Benthic Habitat Analyses Using Micro-bathymetry Data and Subsea Photogrammetry

A Case Study of Benthic Megafauna Community at Karasik Seamount (Arctic Ocean)
Visited during *RV Polarstern* expedition PS 101

by
Amin Mardani-Nejad

A thesis submitted to HafenCity Univerität Hamburg
in partial fulfillment of the requirements for the degree of
Master of Science
Geomatics (Hydrography)

HCU-examinier: Prof. Dr. Karl-Peter Traub
AWI-examinier: Dr. Boris Dorschel

April 2018
Hamburg, Germany

HCU | HafenCity Universität Hamburg
AWI ALFRED-WEGENER-INSTITUT HELMHOLTZ-ZENTRUM FÜR POLAR- UND MEERESFORSCHUNG
HELMHOLTZ GEMEINSCHAFT

Declaration (§20(4) ASPO 2012)

I declare that this Master Thesis – in the case of group work the respective marked parts of the work – has been completed by myself without external help and only the cited sources and references were used.

Literally cited or quotes from different text or other sources are marked.

Hamburg, April 17th, 2018

(Amin Mardani-Nejad)

Acknowledgments

First and foremost, I would like to thank my lord almighty for giving me the strength, knowledge, ability and opportunity to undertake this research study and to persevere and complete it satisfactorily. Without his blessings, this achievement would not have been possible.

I would like to express the deepest appreciation to my supervisors, Dr. *Boris Dorschel* and Prof. Dr. *Karl-Peter Traub*, for their time and support of this thesis. Without their passionate participation, the validation survey could not have been successfully conducted.

A very special Thank you goes out to my supervisor and colleagues at *Alfred-Wegener Institute* for polar and marine research who provided me the fundamental research material and condition, especially Dr. *Boris Dorschel* for all the trust and patronage and support and *Simon Dreutter* for all the helps and aids in many ways and providing me the opportunities of participating in research and training cruises *PS-105* during my studies. Thanks *Boris* and *Simon*, I learnt a lot from both of you.

I thank "Helmholtz Graduate School for polar and marine research", Polmar scientists, trainers and crew on *RV Polarstern* cruise PS-105 and for a great time and a unique experience hands on echosounder and sub-bottom profiler, namely *Dr. Gerhard Kuhn, Dr. Frank Niessen.*

I owe my sincere gratitude to many people for help of various kinds in this thesis, with a special mention to *Dr. Autun Purser* from AWI biosciences division and *Dr. Ralf Krocker* from operations and research platform and *Prof. Dr.-Ing. Hans Werner Schenke*, AWI Bathymetry group, and the PANGAEA team in general a few to mention *Dr. Patricia Slabon*, *Dr. Jan Erik Arndt* and *Dr. Stefanie Schumacher*. Thanks for excellent hospitality it was fantastic to have the opportunity to work majority of my research in your wonderful facilities.

I would like to offer special thanks to *Dr. Rainer Sieger* who, although no longer with us, continues to inspire by his example.

I would also like to thank the experts who were involved in backstage, Thanks to *Dr. Mahdi Hasanlou* from University of Tehran for a helpful discussion regards Image processing and photogrammetry, and *Leila Vashagh* (for practical feature classification discussion).

Furthermore, I am very grateful for the help of *Ruhullah Hosseinie*, my fellow grad student at HafenCity University. With Mr. *Hosseinie* we build up a team to put together the idea of the feature detection logic within point cloud, in order to detect and count trees in forest and further we adapt the method for sponge detection in totally different environment. Thank you *Ruhullah,* it is always great to work with you.

I must express my very profound gratitude to *Dr. Patricia Slabon*, *Jean-Guy Nistad* and *Meri Hietbrink* for assisting me with proofreading.

My acknowledgement would be incomplete without thanking the biggest source of my strength, my family. The blessings of my beloved parents *Behi* and *Eli* and the love and care of my siblings *Mojdeh, Ali, Olduz* and *Aigin* for providing me through moral and emotional support in my life

with unfailing support and continuous encouragement throughout my years of study and through the process of researching and writing this thesis. This accomplishment would not have been possible without them. I cordially thank all of you for your understanding, prayers, and helping me in any possible way.

It would be inappropriate if I omit to mention my dear *Jayron;* thanks for Manual drawing of sponges in ArcGIS. I hope I could give it back to you in your prospective study.

At the end I should mention that the data used for this thesis was collected throughout dives during the *RV Polarstern* cruise PS101, Grant No. AWI_PS101_01, which was a contribution to the FRAM project.

Abstract

The very first map of the Arctic Ocean basin with a few lead line sounding changed the supposal of large continental land beneath of the ice. More resolution added over the decades, reveals the detail of the Arctic seafloor structure of seamounts and ridges below the frozen sea. Numerous methods of bathymetry and mapping were applied as the technology developed over the years for different purposes. While the airborne and satellite-based altimetry and gravimetry data provides a large-scale estimation of the seafloor topography by hundreds of meters resolution, the shipborne and submarine sonars focuses on certain features and areas with higher resolution. During the last century the knowledge of the Arctic seabed geomorphology increased dramatically by the development of acoustic technology combined with altimetry and gravimetry while the habitat characteristic of the polar region still contains lots of mysteries.

The new developments of underwater survey vehicles are bringing new clarity and perspective from the deep sea to the questioners. The sub-meter resolution data of the seabed could be employed for very high-resolution micro topography as well as habitat mapping and feature detection.

The Alfred Wegner Institute for Polar and Marine Research (AWI) developed the Ocean Floor Observation and Bathymetry System (OFOBS) for deep sea research, mostly in polar region. The tailored deep tow system of the AWI is equipped with optical and acoustic sensors in addition to underwater positioning systems. The OFOBS, first deployed during the PS101 expedition, provides a novel dataset of megafauna's habitats at the Karasik seamount.

This thesis is implementing geospatial data mining and knowledge discovery for feature detection by means of habitat mapping in the study area with a focus on the central mount of Karasik seamount where an imperial assemblage of the Geodia sponges are dominating the seafloor.

The main datasets for this study are based on the optical sensor of the OFOBS, including video and still images collected during the dives, while the feature detection within the sonar dataset is in the second place.

During this work study, the development of the OFOBS is also considered in order to improve the capability of the dataset for further expeditions.

Contents

List of Abbreviations

ABS	**A**coustic **B**ackscattering **S**trength
OBIA	**O**bject **B**ased **I**mage **A**nalysis
OBPA	**O**bject **B**ased **P**oint cloud **A**nalysis
ADCP	**A**coustic **D**oppler **C**urrent **P**rofiler
ARAIM	**A**dvanced **R**eceiver **A**utonomous **I**ntegrity **M**onitoring (
AUV	**A**utonomous **U**nderwater **V**ehicle
CEP	**C**amera **E**xposure **P**osition
DEM	**D**igital **E**levation **M**odel
DSM	**D**igital **S**urface **M**odel
DTM	**D**igital **T**errain **M**odel
FH	**F**light **H**eight
FOV	**F**ield **O**f **V**iew
FRAM	**F**rontiers of **A**rctic **M**arine **M**onitoring
GEBCO	**G**eneral **B**athymetric **C**hart of the **O**ceans
GLONASS	**GLO**bal **NA**vigation **S**atellite **S**ystem
GNSS	**G**lobal **N**avigation **S**atellite **S**ystem
GPS	**G**lobal **P**ositioning **S**ystem
GSD	**G**round **S**ampling **D**istance
HS DS3	**H**ydro**S**weep **D**eep **S**ea 3
HS/PS	**H**ydro-**S**weep / **P**ara-**S**ound
IBC	**I**nternational **B**athymetric **C**hart
IBCAO	**I**nternational **B**athymetric **C**hart of the **A**rctic **O**cean
IHO	**I**nternational **H**ydrographic **O**rganization
IMU	**I**nertial **M**easurement **U**nit
ISPRS	**I**nternational **S**ociety for **P**hotogrammetry and **R**emote **S**ensing
MAR	**M**inimum-**A**rea-**R**ectangle
MPES	**M**ulti**p**hase **E**cho**s**ounder
OFOS	**O**cean **F**loor **O**bservation **S**ystem
OFOBS	**O**cean **F**loor **O**bservation and **B**athymetry **S**ystem
PANGAEA	**P**ublishing **N**etwork for **G**eoscientific and **E**nvironmental **D**ata
PPC	**P**er-**P**oint **C**olors
PPN	**P**er-**P**oint **N**ormal
ROV	**R**emotely **O**perated **V**ehicle
SATNAV	**SAT**ellite **NAV**igation
SBAS	**S**atellite **B**ased **A**ugmentation **S**ystems
SLAM	**S**imultaneous **L**ocalization **A**nd **M**apping
SSS-HF	**S**ide **S**can **S**onar **H**igh **F**requency
SSS-LF	**S**ide **S**can **S**onar **L**ow **F**requency
TPU	**T**otal **P**ropagated **U**ncertainty
UAV	**U**nmanned **A**erial **V**ehicle
USBL	**U**ltra-**S**hort **B**ase**L**ine
UTC	**U**niversal **T**ime **C**oordinated

List of Figures

List of Tables

1 Introduction

Roughly seventy percent of our planet is covered with water bodies, including thousands of lakes, seas and five oceans. The International Hydrographic Organization (IHO) recognized the Arctic Ocean as the smallest interconnected ocean which covers less than three percent of the Earth's surface.

Unfortunately, only a small fraction of the worlds' ocean floors have been surveyed with multibeam echo sounders to date. The biggest portion of the existing bathymetry data is derived from satellite altimetry and gravimetric, as it utilized in the General Bathymetric Chart of the Oceans (GEBCO) and International Bathymetric Chart of the Arctic Ocean (IBCAO).

The first featureless single basin map of the Arctic Ocean was a big step forward which changed the knowledge held by humans about the earth. It becomes more interesting when one knows this giant step brought to light by a few charted depths on the first map of the Arctic Ocean was around a hundred and twenty years ago. Fridtjof Nansen and his team revealed that there is no land-mass under the Arctic Ice by the charting the single deep basin of the Arctic Ocean abyssal plain. The concept of the single-basin Arctic Ocean survived for about sixty years until the discovery of the *Lomonosov Ridge which* divided the basin into two separate basins (Weber, 1983). Now there have been several ridges and seamounts added over the years of research to the seafloor by the development of technology but still there are lots of question left unanswered.

Therefore one of the objectives of the PS101 expedition was to collect multibeam bathymetry data of RV Polarstern in order to contribute to the existing ocean datasets (Boetius & Purser, 2017). Part of this data is employed in this thesis for mapping purposes of the Study area chapter.

However, the main intention of the expedition was to study the megabenthos on the Karasik seamount and its outskirts. By the means of analyzing the distribution, diversity and production of faunal along depth gradients from seamount base to peak. (Boetius & Purser, 2017)

In order to study this phenomenon the recently developed deep tow system, by The Alfred Wegner Institute, was employed for data acquisition. The Ocean Floor Observation and Bathymetry System (OFOBS) for deep sea research has a variety of optical and bathymetry sensors along with underwater navigation system in connection with vessel navigation sensor.

The mission of this thesis is focused on the dataset of OFOBS in the following order:

The structure of the OFOBS and its components and all relevant sensors from sky down to the ocean floor will be explained in chapter three. And the operation and data acquisition of the OFOBS will be explained in chapter four, while chapter five will explore the history of the study area with some explanation about environmental and geographic setting of the Langseth Ridge

and Karasik seamount with the intention to explain the geomorphology and habitat characteristics of the area. The sixth chapter will excavate into the provided material from shipborne bathymetry and OFOBS optical and sonar data: partly for mapping the study area and partly for feature detection. The seventh chapter is focused on the several methods of data mining in point cloud and Raster of orthophoto mosaic and side scan sonar. Later the results of the examined methods will present in the eight chapter, relatively in the same order as the methods. The nine chapters try to explain the outcomes and will start with a discussion about uncertainty of the material and results and will provide some recommendations in order to improve the overall system for further expeditions. Finally this work ends by a brief conclusion which is the summary of what has been planned and what was achieved.

This chapter is presenting the introduction of the thesis, with the intention to provide an overall view of the upcoming chapters and the structure of the work. The first chapter following the introduction is presenting the basic principles and logic behind this structure and will provide a general picture of the different components of the interdisciplinary work.

The intention of this work is to develop a spatial data mining workflow in regard to habitat mapping which was tailored for OFOBS datasets and similar underwater systems. The thesis attempts to find the answer for the following questions:

- ***What are the capabilities of the OFOBS datasets for habitat mapping?***
- ***What are the capabilities of the OFOBS datasets for feature detection?***
- ***Which parameters are affecting the quality of the datasets and how?***
- ***What are the challenges in the OFOBS dataset?***

In order to investigate the mentioned questions, the Geodia sponge was chosen as the target of feature detection. The other habitat members such as star fish and shrimp are not targeted in this study. However, it is easier to detect them as they can easily be detected by their colors which are not applicable for Geodia sponges in the sample area.

It is also necessary to mention that in some part of this study the sample area is divided to smaller sections as mater of the hardware/ software capability and limitation.

2 Basic principles

This chapter provides the basic and theoretical information required to better understand the study topic. The initial sub-chapter gives a general overview of habitat mapping and the role of the sponges in the benthic community, with the subsequent two sub-chapters dealing with the interdisciplinary fields of photogrammetry and computer vision. The forth sub-chapter illustrates the pattern recognition, a sub-area of the computer vision, and knowledge discovery. This chapter ends by a brief explanation about Structure from Motion (SfM) technic.

2.1 Habitat Mapping

The term '*benthic community*' refers to those marine organisms which live at the ocean floor interface, within the bottom few feet of the seafloor, and directly on or within the marine sediments, this community is also known as the benthos. Many fauna species within the benthos can be categorized into one of two distinct groups: the deposit feeders and filter feeders. Filter feeders filter their food by siphoning or catching particles out of the water whereas deposit feeders sift through the sediment and consume organic matter within it. Less numerically significant benthos community members include the predators and scavengers, though they will be discussed within the context of this thesis. The main groups within the benthos are shrimps, clams, lobsters, crabs, sponges and worms, though these may significantly change with each region. Sponges are active filter feeders, sessile and of importance to other fauna as their form provides structurally complex habitats for other benthos, fish and invertebrates to utilize and enhance local biodiversity (Keegan et al., 1977).

Benthic habitat studies based on geospatial information are required to provide a premier understanding of the distribution and extent of diverse marine ecology. As a multidisciplinary term, benthic habitat mapping covers a wide territory of mapping fields including the geological mapping of the seafloor with data acquired by bathymetric systems, morphological classification of regions via Benthic Terrain Modeler or even mapping of distinctive biological assemblages into biotopes. Benthic habitat maps are essential components of any successful management plans designed for the planning of the sustainable use of the marine environment, and for the protection of fragile underwater ecology biomes.

The benthos fauna and flora in shallow waters, estuaries and nearshore areas are the most frequently studied and mapped, because the seabed in shallow areas is more accessible than the deep ocean-floors beyond the continental shelf edge, and also because human activities and impacts are more common in these regions, thus these areas are commonly foci of effects

to monitor, preserve and manage the seafloor (Ecological Society of America, 1931; NOAA, 2017).

The recently developed technology of sonars and deep-sea systems are progressively revealing the connections between benthic habitats and the seabed structure, and how these may be affected by geomorphology as well as sedimentology. Seabed mapping and observations published to date shows that specific geomorphic settings like seamounts and submarine canyons are associated with specific benthic communities (Harris & Baker, 2011).

In addition to geomorphology and depth zone classification, there are many datasets which have the potential to be considered for benthic habitat mapping, such as images and videos collected from the seafloor, side scan sonar(SSS) and backscattered data surveys (Harris & Baker, 2011).

The study of the benthos in deep ocean is more challenging than the benthos of shallow areas, as the limited availability of the suitable technology needed for exploration of such environments, especially where the operations need to be done in ice covered, deep regions, such as those found within the harsh environment of the central Arctic Ocean.

The Karasik seamount is one of the habitat zones where an extensive region of seafloor was heavily populated with an assemblage of sponges, discovered during PS101 expedition in 2016(Boetius & Purser, 2017). This thesis attempts to analyze the distribution and characteristics of the sponges collected by the deep-tow system(Purser et al., 2018) within the sample area.

2.2 Photogrammetry

Photogrammetry is a measurement method using remote sensing and deals with the recording and evaluation of images. The basic concept of photogrammetry and its methods are to remotely determine from a number of distinct images taken of a particular area or object from different angles, analyzing the shape, size and position of the imaged objects in space within these images allowing them to be mapped into a three-dimensional space relevant to each other. As a result, a three-dimensional reconstruction of the imaged object field based on two-dimensional source images is possible. The derivation of the geometric quantities in space is subject to the central projective image and requires a reconstruction of the radiation bundles in three-dimensional space using the known internal and external orientation of the camera.

If the parameters of the inner and outer orientation are known, the three-dimensional model determines an object point from the intersection of at least two corresponding spatially different image rays. The measurement of the object does not take place directly, but indirectly on the reconstruction of the object (Luhmann et al., 2013).

- **Bundle block adjustment**

The bundle block adjustment is a method of image orientation and point determination in which any numbers of images arranged in space are computationally oriented simultaneously in a higher-level coordinate system.

It is considered as the most powerful and accurate method for image orientation and object point determination in photogrammetry.

The collinearity equation represents the mathematical model of the bundle block adjustment. First, the image coordinates of homologous points are used as observations. These are the pixels whose rays, starting from the respective projection centers, intersect at one point on the terrain surface. The basis for this is that each measured pixel corresponds to a spatial direction measurement from the projection center to the object point. These directional measurements are also referred to as image rays. If two image rays of homologous points intersect, the object point can be determined in absolute space, knowing the elements of the inner and outer orientation.

Each image beam of a digital image, together with the projection center, forms a spatial beam of light. The bundles of rays of any number of images are simultaneously computationally oriented using the bundle triangulation method, and the object points in space are determined by the intersection of the corresponding image rays. For a large number of images, the combination of the beams and their intersection of the homologous points lead to a high geometric stability of the spatial beams and an optimal determination of the object points (Luhmann et al., 2007).

If the image coordinates of the homologous points in the observation are included, the following unknown parameters can be determined as a function of the observation, iteratively, for each image and each camera:

-Object coordinates	➢ 3 unknowns for each point
-External orientation	➢ 6 unknowns for each picture
-Inner orientation	➢ 0 to 3 unknowns for each camera

Figure 2-1: Camera positions (519 video frames) and central rays of bundle block adjustment in the spherical shooting scenario, experiment of Reconstructed 3D Model, consist of 519 image extracted from 1:45 min video captured by Smartphone (Nexus 5), frame resolution HD (1080x1920),built in *Agisoft PhotoScan* (Own representation, Photographer: S. Dreutter)

Accordingly, the object coordinates in the space, the elements of the outer and inner orientation and other model parameters are calculated by adjustments in an overdetermined system of equations. In the same step, statistical information about the accuracy and reliability of the adjustment can be output. The adjustment requires a linear relationship between the unknown and the expected value. Since the collinearity equations are not linear, Taylor's linearization is performed using approximate values of the unknowns. In a simultaneous calculation process, all observations and all unknown parameters of an image association are integrated and iteratively improved until the intersection of the image rays at the object point is optimal (Luhmann et al., 2007).

2.3 Computer Vision

An important associated discipline of photogrammetry is computer vision, also called machine vision or image understanding. Computer Vision is essentially concerned with image and object recognition and attempts by different methods to reproduce the ability to interpret hu-

man vision. Figure 2-2 illustrates the interplay between the computer science disciplines of visual computing.

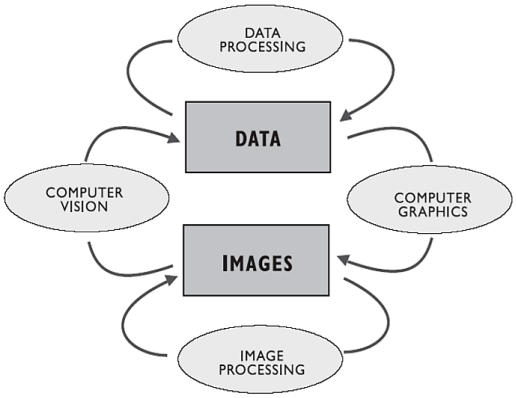

Figure 2-2: Computer vision scope with regards to data and image processing (Sablatnig, 2009).

In principle, different methods for capturing, processing, analyzing and interpreting images play important roles in gathering data on regions of interest, and these have overlaps with photogrammetry in the area of automatic image analysis. The detection and description of objects in pictures is the essential basic target within the field of computer vision. Properties of objects and their classification for derived products, such as the selection and measurement of features in object space, can be derived (Sebe, 2005).

Applied mathematics and information processing lay the foundations in the field of computer vision, as this is mainly about the design and application of large computational methods.

Furthermore, photogrammetric measurement methods due to the above-mentioned overlap in the recording and evaluation of digital images are an important facet of computer vision. Again, photogrammetry benefits from the results of Computer Vision (Heipke, 2003).

Computer Vision is, apart from computer graphics and image processing, a significant part of Visual Computing, combining all disciplines of computer science dealing with image information and the modeling of 3D objects. While computer graphics are used to generate images from numerical data and process them via image processing, Computer Vision is concerned with extracting image information for generating models or reproducing the real, three-dimensional world using two-dimensional images (Sebe, 2005).

2.4 Pattern Recognition

The aim of pattern recognition is to develop mathematically and technically feasible methods which are modeled on human abilities such as vision or hearing (Sebe, 2005). The focus is on

the classification of objects based on defined characteristics such as size, circumference, color, distances, etc. Pattern recognition is used in areas such as speech, object and text recognition.

Pattern recognition is already at play in many areas of everyday life. Examples include the digital language assistants, such as Amazon Echo, Google Assistant or Apple's voice assistant Siri. In addition, today almost all mobile devices with touch-sensitive screens offer the facility for handwriting recognition. Furthermore, there are more and more applications for face recognition and the identification of objects.

In a time of enormous amounts of data availability (big data), automatic pattern recognition is becoming more and more commonplace, for example in medicine (evaluation of x-rays), industry (quality control), biology (analysis of microorganisms), robotics (autonomous driving), and satellite and flight image analysis (remote sensing and photogrammetry) and progressively more important (Ripley, 2007).

Using pattern recognition and image processing, information from recordings can be extracted and classified. The pattern recognition takes place in two phases: The work phase which is the main process and the learning phase (training algorithms).

Since there are several methods of pattern recognition, Figure 2-3 is illustrating the procedure in a general view. It can be seen from the scheme that the pattern recognition starts with the object recording by means of a sensor e.g. a camera and the associated signal processing begins. This leads to the pre-processing stage, which serves to enhance the quality of the recording.

This is followed by the extraction of the features by searching for target features. The characteristics are assigned according to classification rules and the different classes.

The classification characteristics are determined by sampling the feature extraction and the result are separated into clusters (Duda et al., 2001; Ana Fred, 2016).

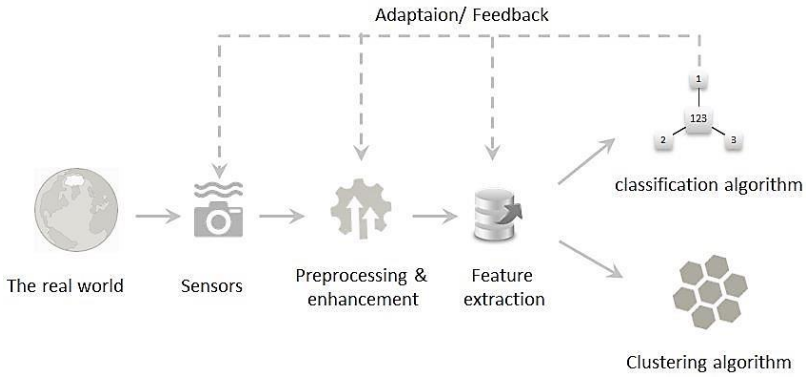

Figure 2-3: Schematic workflow for pattern recognition and classification, own representation adapted from (R.O. Duda, 2001)

Pattern recognition is also the main part of the Knowledge Discovery in Databases (KDD) particularly in image processing and Geospatial datamining which is partly implemented in this

thesis for hybrid cluster analysis (Sassi, 2012). The following graph is describing the logic of the KDD.

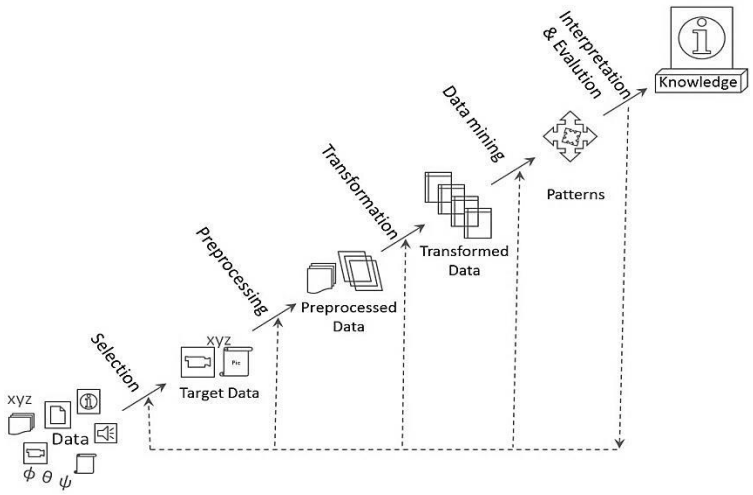

Figure 2-4: Steps of KDD, own representation adapted from (Fayyad, Piatetsky-Shapiro, & Smyth, 1996)

The following graph illustrates the knowledge discovery in geospatial datasets within the multidisciplinary study of this thesis, where the overlap of disciplines is employed as individual steps on specific concepts and where the discovered knowledge is determined.

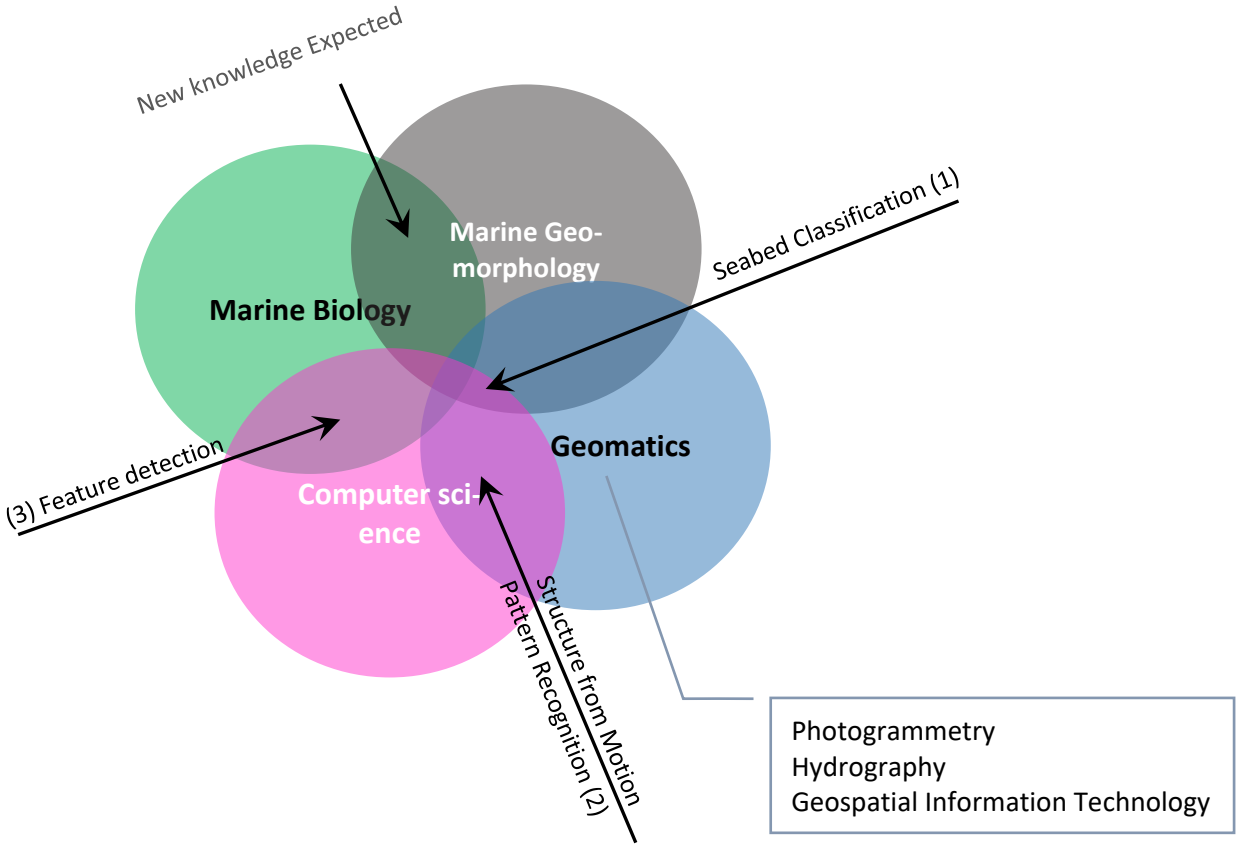

Figure 2-5: Multidisciplinary study overlaps and expected new knowledge

2.5 Structure from Motion

Structure from Motion (SfM) is a method for detecting corresponding features in images and restoring spatial object structures. In principle, it is equivalent to the process of multi-image photogrammetry.

The SfM method is based on spatial vision. The reconstruction of the 3D objects is done using matches in images called features of corresponding points. The reconstruction of the position and form of objects from photographic images deals with perspective vision based on the model of the pinhole camera, which is closest to natural vision. The majority of the creature visual perception system is based on the SfM phenomenon, where 3D structures are recovered from a sequence of 2D motions. This projection is achievable if one can find the correspondence between the image features such as corners or similar patterns and break lines in multiple direction (Kale et al., 2010).

One of the most conventional algorithms which implements the SfM method in computer vision is SIFT, standing for “Scale Invariant Feature Transform”. The SIFT algorithm forms the basis for the detection of features, it allows for the unraveling of invariant features in terms of rotation, translation, scaling, changes in lighting conditions, and partial affine distortion in images. The reliable identification of objects in 3D space can be done on the basis of the invariant characteristics.

For the detection of robust features, the maximum difference between two adjacent maps of the Gaussian pyramids (Difference of Gaussians, DOG for short) is determined. Gaussian pyramids represent sequences of the same image with continuous smoothing and scaling (down sampling). The extracted features are smoothed for contrast and edges and then localized. In a further step, the main orientation of the glazed and localized feature points is determined with the surrounding image gradients. The final step of the SIFT algorithm is to generate the feature vectors based on the feature region defined by the main orientation. The feature vector contains information about the environment of the main orientation. Then the robust features of an object can be extracted using the SIFT method in a rotated, shifted, scaled, partially affine distorted, and different illuminated image (Lowe, 2004).

3 Platforms and Instruments

During the PS101 expedition several deep-sea systems were operated from the Icebreaker RV Polarstern, while the hull mounted bathymetry systems were in 24-hour operation mode sounding the seabed and profiling the sub-seafloor. These platforms were dispatched from time to time in a series of missions in order to observe and collect detailed information about the seabed and sea-ice.

The ROV BEAST, from AWI and the NUI hybrid robot from the Woods Hole Oceanographic Institution (WHOI, USA) are the other deep-sea systems which were use during PS101 along with the "Ocean Floor Observation and Bathymetry System (OFOBS)" from the AWI (Boetius & Purser, 2017). In this chapter the characteristic of the two platforms are described, RV Polarstern as the mothership and OFOBS as deep-tow system, since this thesis benefits from the data collected by these two platforms.

3.1 RV Polarstern

RV Polarstern, a German-icebreaker, is operated by the Alfred-Wegener-Institute, Helmholtz Centre for Polar and Marine Research (AWI, 2017). The icebreaker has served as a research and supply vessel for about 36 years in the Polar Regions, commissioned in 1982. She has an overall length of 117.91 m, and a maximum draft of 11.21 m. The minimum operational temperature for the vessel is -50°C. Polarstern is armed with four powerful engines and double-walled steel hull, allowing her to break through 1.5-metre-thick ice at a speed of 5 knots, while thicker ice can be overcome by ramming (El Naggar, 2006). The characteristic of the vessel is listed in the table3-1.

RV Polarstern characteristic	
Port of registry	Bremerhaven
Length	117.91 meters
Width	25 meters
Max. draught	11.20 meters
Max. displacement	17,277 tons
Empty weight	12,012 tons
Commissioning AWI	1982
Engine	4 x KHD RBV 8M540
Engine power	19,198 PS (four engines)
Range	19,000 nautical miles / 80 days
Max. speed	16 knots
Operation area	Everywhere including pack ice zone
Days on sea per year	Ca. 310
Max Scientists long = 53	**Crew = 44**

Table 3-1: RV Polarstern caracterestic (El Naggar, 2006).

RV Polarstern can be considered as a massive measuring instrument which persistently collects multipurpose oceanographic and meteorological data aboard; meanwhile some systems are running 24 hours during the cruise while others are only available upon request. Part of the collected data is sent steadily to different databases. The official supporting webpage of the AWI categorizes scientific devices onboard RV Polarstern into 9 different group (Table3-2) (AWI et al., 2018).

Category of Scientific devices onboard	
Biology Devices	2 type
Echo Sounders	9 devises
Marine Geophysics	3 devises
Meteorology	10 devises
Ocean Floor Observation and Sampling	12 devises
Oceanography	8 devises
Satellite Data Processing Systems	1 system
Ship Navigation	10 system
Underwater Positioning Systems	2 system

Table 3-2: Scientific devices onboard RV Polarstern in categories

Data management
Local storage on computers (raw data)
DShip - system
Mass data storage and archiving
Transfer data on land
Uploading data to Pangaea database (including meta data)

Table 3-3: Data management system of RV Polarstern

Among all the instruments and devices onboard *Polarstern*, there are some of them which have been involved directly or indirectly for the acquisition of data that this thesis benefits from and will be introduction here.

In order to establish the relation between the various sensors and their alignments, the offsets of all the fixed sensors on the ship's hull are measured (Appendix A). The "Vessel Survey" must be updated whenever a change or new installation happens regarding measurement sensors. The last entire Vessel Survey for *RV Polarstern* was accomplished on 2010, and the third version of updates had been done before the PS-101 expedition on May 2016 (Overath&Sand-Surveyors, 2016).

The following picture is illustrating the relevant sensors involved for data acquisition; including shipborne bathymetry, OFOBS based micro bathymetry and optical sensors.

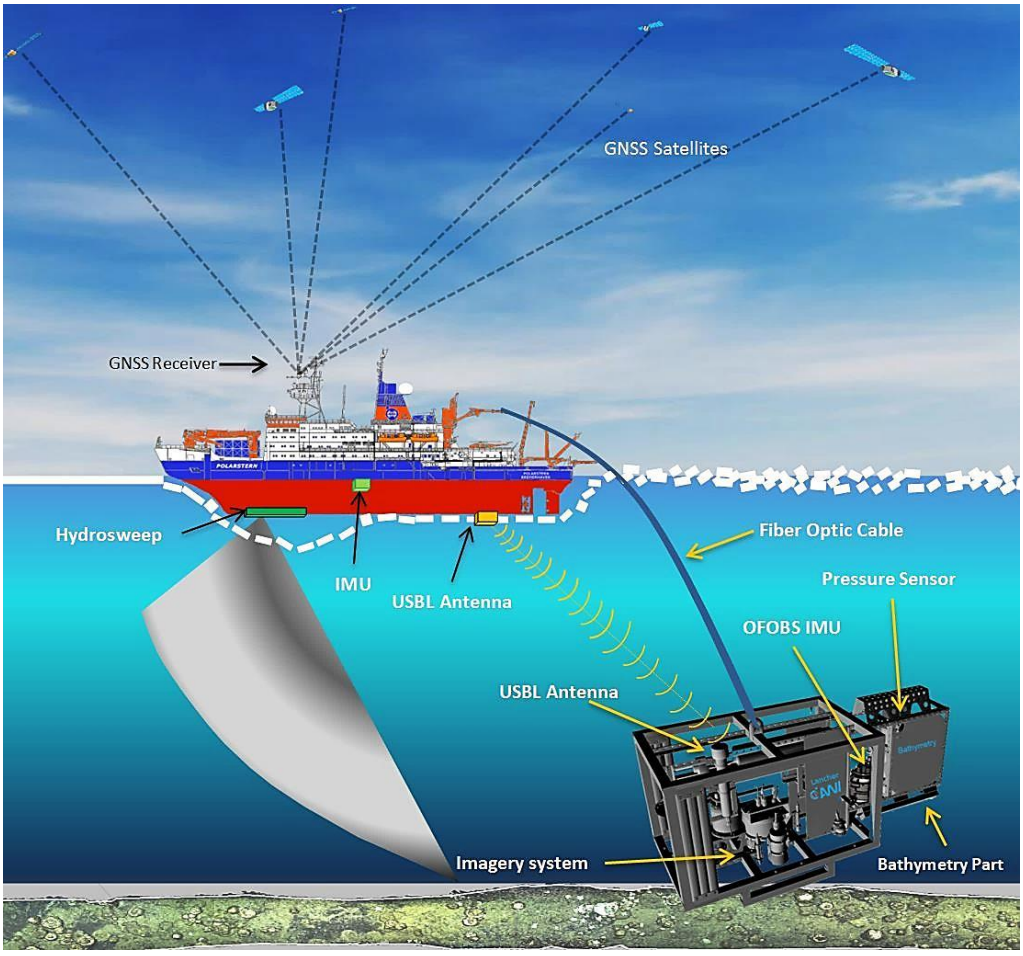

Figure 3-1: Schematic illustration of sensors and relation of the sensor involved for data acquisition in the sample area. While RV Polarstern was breaking the sea-ice, the vessel hull mounted multibeam was sounding the surface of the seamount, and the OFOBS was recording the habitat evidence by video and photo cameras, and the sonar extension was collecting high resolution micro-bathymetry data.

3.1.1 HydroSweep DS III

The HydroSweep DS is a wide-angle, fan-shaped deep water multibeam echosounder, that has been operating since 1989 on *Polarstern*, with the latest upgrade happening in the autumn of 2010. The HydroSweep DS III is the third generation of the high resolution multibeam Echo-sounder of its type and is suited for bathymetric bottom detection and seabed mapping from 10 m up to 11,000 m, covering full ocean depth based on a sonar frequency from 13.6 to 16.6 KHz, changing with defined depth sequences. (Slabon, 2014; AWI et al., 2018).

The HydroSweep DS III uses adaptive bottom tracking windows in order to identify sonar targets in the water column (TeledyneRESON, 2010). The HS DS III is a permanent installation on the hull of RV Polarstern and equipped to stand the polar circumstances with an ice protection layer on the transducers. The HydroSweep system consist of 3 major components; hull mounted transducers arrays (located in a box keel), top side controller hardware (located in room E525A) and operation software (E550 room and Bridge) (AWI et al., 2018).

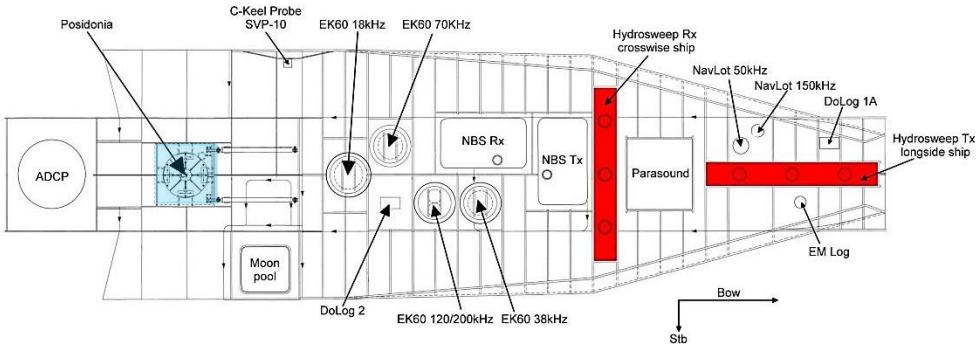

Figure 3-2: Position of the HydroSweep DS III transducer array (Tx) and receiver array (Rx) in related to the other sensors in Polarstern box Keel (AWI et al., 2018).

In order to compensate the possible gaps due to surveying at higher ship speeds, the HydroSweep applies a 2x multi-ping, meaning two swaths are transmitted simultaneously per ping slightly tilted along track. The aperture angle of the full swath amounts to 140° x 2° and the footprints can be arranged for “equal-angle” as well as “equal-distant” pattern mode. The manufacturer claims that with each measurement, 320 hard beam depth values are directly determined which could be interpolated up to 960 additional sounding soft beams via software calculations (TeledyneRESON, 2010). While the AWI instrument portal and an unpublished internal paper gives slightly different numbers of 313 hard beams and 920 soft beams (Slabon, 2014; AWI et al., 2018).

Multibeam calibration is performed after ship yard time in the case of transducer element(s) replacement. The annual calibration is performed at a well-known profile in the Atlantic Ocean nearby Ampere Seamount (ca. 700 km westerly of Gibraltar), where Polarstern is passing this profile on its way from Bremerhaven to Cape Town (El Naggar, 2006; Slabon, 2011).

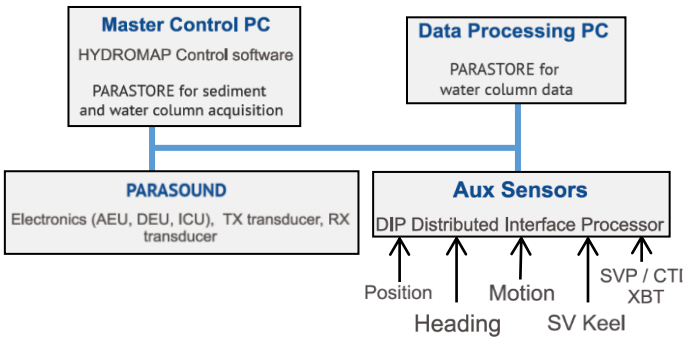

Figure 3-3: Typical HydroSweep System Configuration (TeledyneRESON, 2010).

In order to calculate the pings positions, the three auxiliary information are implemented via a Distributer Interface Processor unit (DIP); the navigation data (Position and Heading) from the GNSS sensors, Attitude information from Inertial Measurement Unit (IMU) sensors and Sound Velocity data provided by SV sensor on keel as well as the manual probe of SVP (Lurton, 2002). Atlas Hydromap Control is the controlling software of Hydrosweep DS3. For data acquisition the HYPACK® SURVEY(HYPACK (Ed.), 2016) software was employed. Atlas Parastore software used for visualizes, process and data conversion. The recorded data was stored in 30 min blocks and Post processing of the bathymetry data was conducted partly on board during expedition and partly done after the cruise in the CARIS HIPS and SIPS software.

3.1.2 Navigational Systems

In order to calculate the correct position of the acquired multibeam data, three more data types are needed from the relevant sensors; 1) appropriate navigational system for vessel position, 2) Attitude sensor for vessel movement around three coordinate axes, 3) Sound Velocity Profiler for measuring the speed of sound in the water column.

On board RV Polarstern, it consists of the GNSS and the Marine Inertial Navigational System, both together providing an absolute positioning accuracy of about 15 m, which also provides the vessel positioning data for Posidonia USBL in order to track the OFOBS during the dives (Slabon, 2011; AWI et al., 2018).

GNSS receivers

To achieve acceptable position of the vessel, it is necessary to use an appropriate positioning system. The Global Navigation Satellite System (GNSS) is the standard generic term for satellite navigation systems (satnav) which provide autonomous geo-spatial positioning with global coverage. GNSS integrity can be achieved via Satellite Based Augmentation Systems (SBAS) as well as Advanced Receiver Autonomous Integrity Monitoring (ARAIM) (Reid, 2015).

During the last two decades the accuracy, redundancy and availability of the GNSS have been increased regarding the technology and regulation improvements, since the Selective Availability of the US Global Positioning System (GPS) was discontinued (Clinton, 2000) and alternative systems from other nations (e.g. GLONASS) came to operation. Therefore the navigation possibilities have increased and consequently, the positioning of the multibeam targets at the seafloor have increased as well as under water positioning (C.J. de Jong, 2010).

At least two GNSS receiver sets are operating on RV Polarstern. A Leica MX400 GPS set for vessel navigation purposes and a Trimble SPS855 set with two receiver antennas are installed for scientific use. The device is a combined radio and all GNSS constellations (e.g. GPS, GLONASS, and Galileo), providing position data for a large number of scientific devices on the vessel. Most sensors do not directly receive positions from GNSS sensors but from Inertial Navigation System HYDRINS. There are two independent systems installed called Trimble 1 and Trimble 2. Both consist of an antenna Zephyr Model 2 Rugged and were installed on the antenna deck above the bridge (port side and starboard). The two receivers are installed in the scientific panel on the bridge. Trimble 1 is sending NMEA0183 telegrams to motion sensor

HYDRINS 1 and DShip. Trimble 2 is sending telegrams to motion sensor HYDRINS 2 and DShip (AWI et al., 2018).

The Device manufacturer claims sub-centimeter accuracy in Real-Time Kinematic (RTK) mode and less than 5 m 3DRMS with SBAS positioning, while the RTK and SBAS solutions are depending on reference stations. Since the land station signals could not reach the vessel in the open ocean the RTK modes are useless, and SBAS covers only distinct areas on the northern hemisphere and is not covering the high latitudes in the Arctic Ocean by the time of PS101, therefore the uncorrected standalone GPS accuracy is approximated about 10 to 15 m (C.J. de Jong, 2010).

HYDRINS

The ship's motion influences the position of the transducer and Posidonia antenna and subsequently the survey data, which can be corrected appropriately. In order to neutralize the vessel roll, pitch and heading, on the pings position, two units of the high-performance inertial navigation system (INS) are installed close to the pivot point of RV Polarstern (AWI et al., 2018). The newly installed HYDRINS are optimized for hydrographic surveying using multibeam echosounders. HYDRINS are comprised of a single compact unit manufactured by iXBlue and delivers highly accurate real-time heading and attitude information as well as position and speed to other systems and displays. It can receive data from other sensors to improve its accuracy. HYDRINS contain a navigation algorithm based on a very advanced Kalman filter. This structure enables HYDRINS to be connected to the GNSS or to work in a pure inertial mode (iXBlue-SAS, 2016).

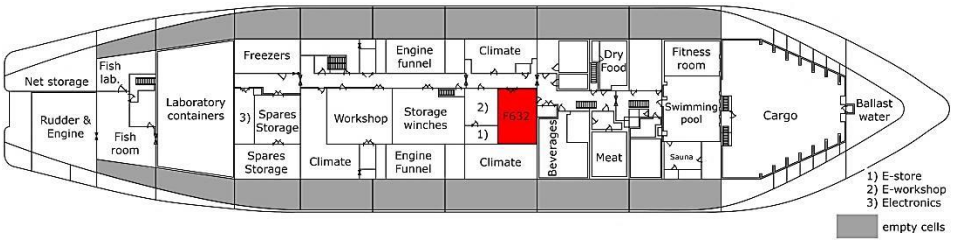

Figure 3-4: Schematic drawing of the location HYDRINS Motion sensor on Polarstern deck F (AWI)

The sensor provides motion and position data for a large number of scientific instruments on board Polarstern. The system is receiving position data from the Trimble GNSS unit and is delivering positions centered to HYDRINS 1. Several output interfaces are defined to deliver different formatted data strings with different frequency to users. The main device is a three component laser accelerometer (AWI et al., 2018).

Figure 3-5: Installation of the HYDRINS-1 and 2 in the Gravity Room of RV Polarstern (AWI)

It is installed in the Gravity Meter room of the vessel. For backup there is a second system installed. Downstream equipment of HYDRINS 1 and HYDRINS 2 are meant to select one of both HYDRINS to be active as one and to deliver data to customers. Additionally the converter boxes are installed to split outgoing data streams and to convert them into several formats requested by customers.

Time synchronizing is received from responsible Trimble GPS receiver (HYDRINS 1 is receiving data from Trimble 1, HYDRINS 2 from Trimble 2). Geographical ship position is received from responsible Trimble GPS receiver (HYDRINS 1 is receiving data from Trimble 1, HYDRINS 2 from Trimble 2). Positions provided by HYDRINS 1 and HYDRINS 2 are both centered to HYDRINS 1 (AWI et al., 2018).

GNSS	No aiding
Position (Latitude and Longitude) accuracy	
2 to 3 times better than aiding sensor	3m after 2min (CEP50) 20m after 5 min (CEP50) 0.6 NM/h (CEP50)
Speed (North and East) accuracy	
0.1 knot (RMS)	0,6 knot (RMS)
Heading accuracy	
0.01° seclat (RMS) 0.2 mrad (RMS) 0.6 arc min seclat (RMS)	0.05° seclat (RMS) 1 mrad (RMS) 3 arc min seclat (RMS)
Attitude (Roll and Pitch or Vertical Reference) accuracy	
0.01° (2RMS) 0.2 mrad (2RMS) 0.6 arc min (2RMS)	0.01° (RMS) 0.2 mrad (RMS) 0.6 arc min (RMS)

Table 3-4: HYDRINS outputs with/without GNSS aid (iXBlue-SAS, 2016).

Posidonia USBL system

Posidonia II is an ultra-short baseline (USBL) acoustic positioning system for high-accuracy and ultra–long range tracking of subsea vehicles. On board Polarstern there are three different antennas available, which can be used alternatively but not at the same time. A Flush antenna is permanently mounted in the ships keel at about 11m depth (Figure 3-2). The antenna is protected by a window, which can be opened during operation (Figure 3-6) (AWI et al., 2018).

The second antenna, named deployable antenna, is lowered through the moon pool. Lastly the third antenna from Thomson Marconi is fixed mounted to a device carrier for moon pool. The control and operation of the system is performed via web-Interface.

There is different version of Oceano transponders available for the Posidonia system on board the vessel. The maximum reachable depth is 6000m with accuracy of 0.2% of the slant distance. The online data stream of Posidonia is broadcasted via a network and the time synchronizing for the USBL-Box is provided by the Trimble GNSS receiver. In addition, the geographical position and orientation of the vessel are provided by MRU iXBlue HYDRINS via DShip system (El Naggar, 2006; AWI et al., 2018).

Figure 3-6: Antenna of Posidonia (AWI)

3.2 Ocean Floor Observation and Bathymetry System

Deep-tow observation vehicles are ocean floor survey systems designed to operate in deep-sea environments, supplied with imagery systems and can also be outfitted with sonars. These systems are submerged and towed behind a vessel or submarine at low speeds at the end of a cable measuring several thousand meters in length.

Figure 3-7: The new OFOBS - PS101 deployment in icy condition (Photo: S. Dreutter, AWI)

The first version of “Ocean Floor Observation System” (OFOS) is a deep-towed underwater imagery system, property of Alfred Wegener Institute, designed and built by Helmholtz program ROBEX. The OFOS is used for a vast variety of purposes, from bathyal organism observation to topographic/geological survey of hydrothermal activities within polar region. The main OFOS is armed with two sets of imagery systems, a high-resolution photo-camera in waterproof housing at the center of vehicle with an adjacent high-definition video-camera with a 5° tilt, in order to provide the best footage coverage together. Both of the cameras are mounted

to a steel frame on the vehicle, escorted with two strobe lights, and three laser pointers at a distance of 50 cm from each other meant for dimension estimation of the seafloor structures and features. Moreover, four LED lights, supporting the lighting system and a USBL positioning system makes it possible to track the location of the OFOS during deployments. The configuration of the OFOS and the sonar extension is illustrated in Appendix B (Purser et al., 2018).

A while before PS101, the OFOS was upgraded with a tailored bathymetry extension, including the interferometric side scan Bathymetry Sonar of *EdgeTech* and a forward-looking sonar system of the BlueView.

The new improved OFOS system with Sonar extension mentioned in the Cruise report as OFOS-Sonar but later in the technical published paper the system is mentioned as OFOBS which stand for “Ocean Floor Observation and Bathymetry System”(Purser et al., 2018).

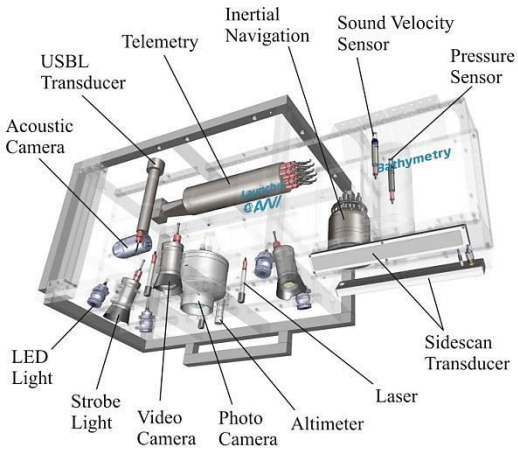

Figure 3-8: Schematic illustration of OFOBS components and instruments (Purser et al., 2018).

The reason why the deep-sea research group at the AWI intended to equip the OFOBS with the sonar extension was to expand the survey range of the vehicle in order to augment the seafloors pictorial data with sidelong swathes of habitat data provided by the side scan sonar (Boetius & Purser, 2017).

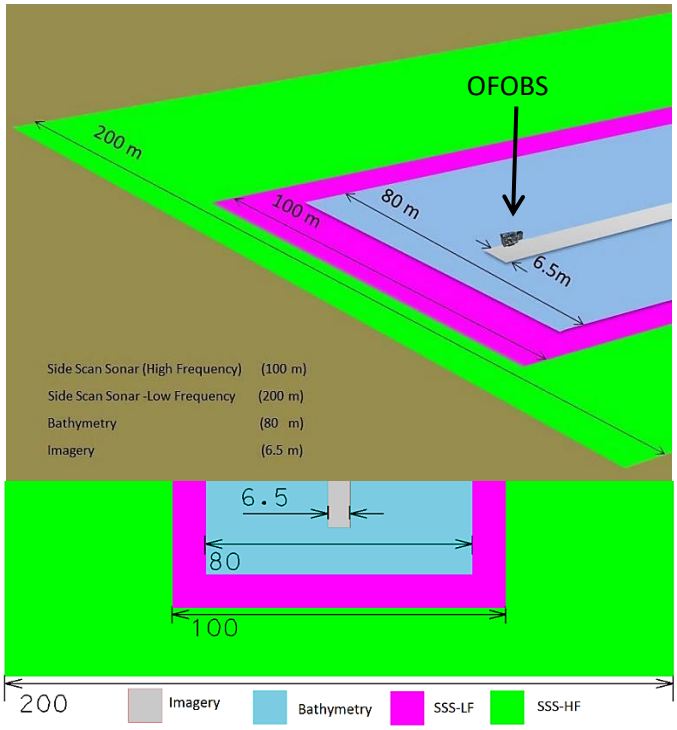

Figure 3-9: Schematic compression of the OFOBS subsea unit imagery and sonar coverage of swath widths from a flight height of 4.5 m

The forward looking sonar was aiding for the real-time avoidance of approaching obstacles, specifically in the steep terrain and sudden cliffs as well as bigger rock formations (Purser et al., 2018).

The OFOBS consists of two main components: the topside unit installed on the support vessel, and the subsea unit. The topside unit is a ship-mounted rack unit, which supplies power and connectivity via a combined fiber optic cable with maximum range of 6000-m depth.

OFOBS and installed devices on subsea unit		
Dimensions	Length	235 cm
	Breadth	92 cm
	Height	105 cm
	Weight (in air)	1000 kg
Operation	Maximum towing depth	6000 m
	Towing speed	Less than 1 knot
	Towing altitude	Imagery 1.5–5 m above the seabed Sonar 5–10 m above the seabed
Imagery system downward looking camera systems	High-resolution photo-camera	CANON EOS 5D Mark III + 24 mm fixed lens
	High-definition video-camera	Sony FCB-H11
	Strobe lights	iSiTEC UW-Blitz 250, TTL driven
	Four LED lights	iSiTEC
	Triple red laser points positioned 50 cm apart from each other in triangle form	*OKTOPUS*
Acoustic systems	Side scan bathymetry sonar	EdgeTech 2205 AUV/ROV MPES (Multi-Phase Echosounder) with two side scan frequencies (230 kHz & 540 kHz) for different range and resolution achievements
	Bathymetry bathymetric 2.5D data in the range of the 540 kHz	
	Forward looking acoustic camera	BlueView M900-130
	Sound Velocity Probe	*AML Micro-X 6000 SV-Xchange*
Navigation and motion sensors	Pressure sensor	*Integrated in AML Micro-X 6000 P-Xchange* 0.05% FS and a precision of 0.03% FS, up to 6000 dbar
	Ultra-short baseline (USBL) transponder	iXBlue Posidonia II
	Inertial navigation system (INS)	iXBlue PHINS 6000 INS

Table 3-5: OFOBS subsea unit Components and characteristics

The full OFOBS system components is described in the published paper of the AWI deep-tow system group also mentioned as AWI- Launcher in full detailed (Purser et al., 2018). In order to avoid duplicating the information of the system the rest is provided in chapter 4.2 within OFOBS operation.

4 Data acquisition

On the noon of the 9th September 2016 the expedition PS101 started from Tromsø port towards the Gakkel Ridge with the aim of investigating the "KARASIK" seamount and hydrothermal vents of the Gakkel Ridge. The layout of the research program was to investigate the morphology, geophysics, biogeochemistry, petrology, microbiology and the faunal composition of both seamount and hydrothermal vents. The forty two days expedition ended on the 23th of October in Bremerhaven (Boetius & Purser, 2017). The Figure 4-1 is presenting the main study area and RV Polarstern track line during PS101.

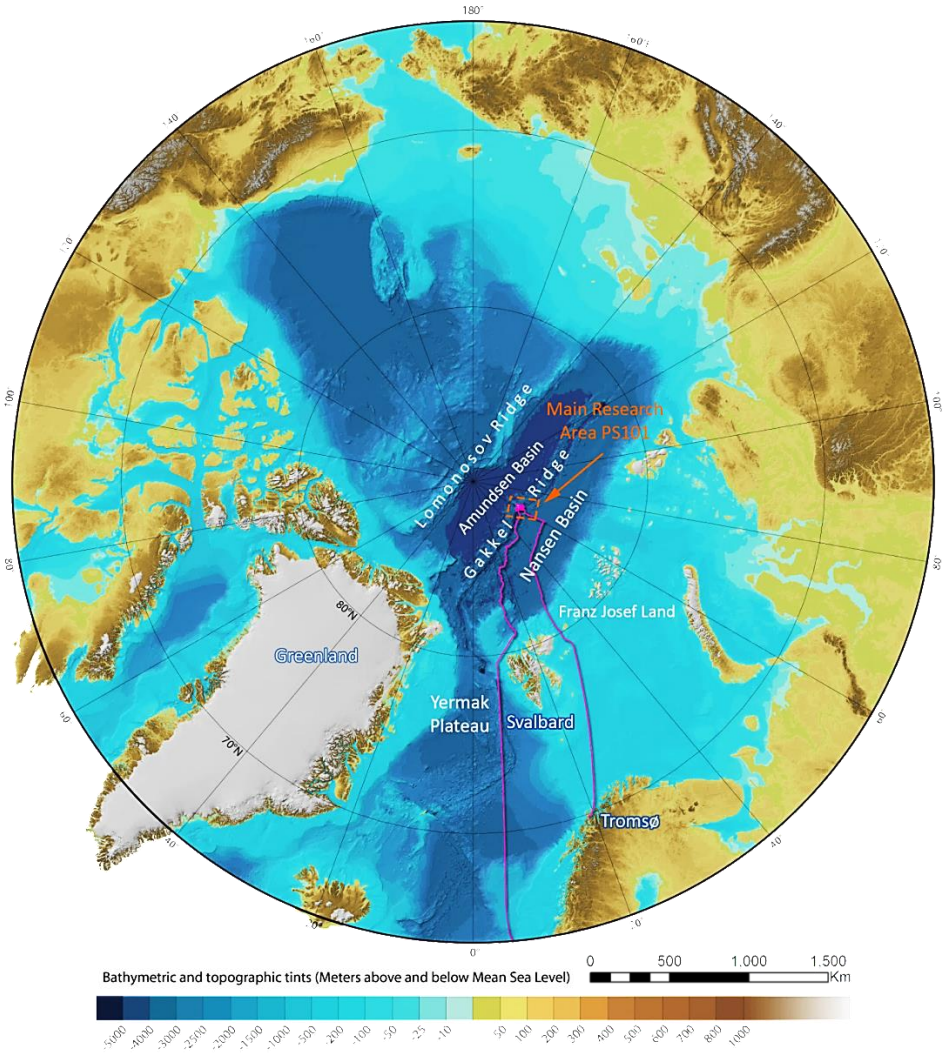

Figure 4-1: The Main Research area (orange box) of PS101 at the Central Arctic Ocean and RV Polarstern track line (Purple) started from Tromsø in 9th Sep and moored at the Bremerhaven 23th Oct 2016. The background map is version 3.0 of IBCAO 30 arc second bathymetric grid (Jakobsson et al., 2012).

The Ocean Floor Observation and Bathymetry System (OFOBS) was one of the main scientific survey instruments used during the research cruise PS101 which contributed to the aim of the FRAM infrastructure program by applying innovative technologies for monitoring Arctic change, especially in the Eurasian Basin. (Boetius & Purser, 2017).

4.1 Vessel based Data acquisition

The vessel-based data was recorded 24 hours per day in 2 working shifts, with the *Hydrosweep* DS III System; *Hypack 2015* was employed for visualizing the beam profile and backscatter data. Water column data was not recorded since there were no relevant water column features visible. The sound velocity probe was not collected individually by the bathymetry group since the oceanographer's group cast and provided the vertical sound velocity profiles from the CTD or XCTD casts and applied to the software (Boetius & Purser, 2017).

4.2 OFOBS operation and Data acquisition

The main intention of deploying OFOBS to the height of several meters above the seafloor was to visually investigate the seafloor to determine the geological, sedimentological and biological community structures across the surveyed area. The benthic community structure on top of the Karasik Seamount was in high intention and well known prior to the PS101 expedition. (Boetius & Purser, 2017).

As it was mentioned in the sub-chapter (3.2) the OFOBS has two main parts: a top side monitoring and controlling unit and a subsea unit, which is the multi-sensor platform. These two units are connected to each other via an umbilical cable for both side communications, in addition to the ship's power supply. The fiber optic cable is connected to the ship's network for data flow and distribution over the network enabling the technicians and scientists to set up their computers to connect to the subsea unit's sensors during the dives while monitoring the seafloor via the online video and forward looking acoustic camera.

Prior to the first dive the top unit of OFOBS needed to be set up within the ship's infrastructure in order to connect to the subsea units. All the settings for controlling and monitoring are located in the winch room of Deck D, where the OFOBS team can communicate with the winch operator in the same work stations (Dreutter, 2017).

As long as there are network connections and relevant controlling software for each sensor, any computer could carry out the operation of the relevant sensor, thus the operation could be deferred from time to time, but the principals are the same. The following description is a tailored setting for PS101 described by the OFOBS team that participated on the same cruise.

During the OFOBS dives about seven PCs with multiple displays were connected to the subsea unit and the controlling and monitoring sensors dataflow. In general, for a 12-hr OFOBS dive a

team of four is optimal, excluding the winch driver. The Figure 4-2 and Table 4-1 provide the requirements of the OFOBS team for 12-hr operation and the overall PCs tasks (Purser et al., 2018).

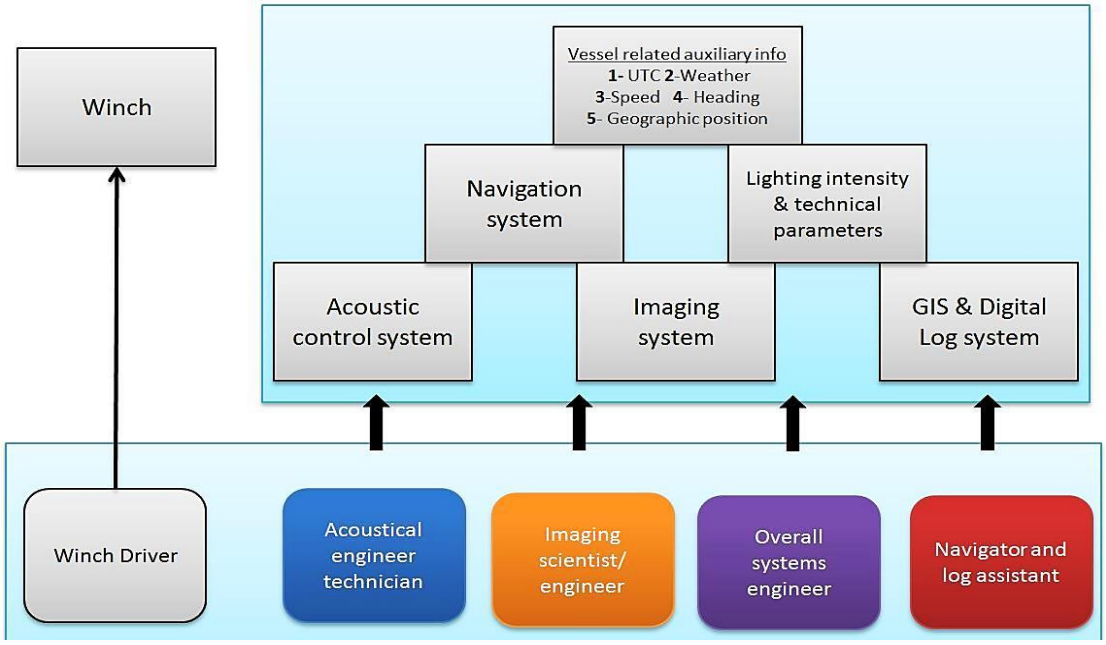

Figure 4-2: OFOBS top unit setting PCs and Operations for 12-hr deployments.

Operational Team of OFOBS for 12-hr deployments	1-Overall systems engineer	A dedicated systems engineer is required to ensure the full suite of OFOBS subsea systems and sensors are operating and communicating with the topside unit correctly.
	2-Acoustical engineer	An engineer or appropriate technician is required to operate the acoustical systems correctly. Acoustic interpretation is essential within unknown regions exploration could be challenging
	3-Imaging scientist/engineer	This member is supervising the imaging data collected by the subsea unit is controlling all video data and timed image data to assure data are collected and recorded properly and looking for appropriate flight height. This member is continuous communication with the winch operator, advising on height corrections required to maximize the usefulness of collected data and to aid in hazard avoidance.
	4-Navigator and log assistant	This member monitors and records the position of the subsea unit within a geographic information system (GIS) framework in real time, while communicate with the bridge for request modifications to the course headings or changing research requirements. Also keep the log of the dives updates
	5-Winch operator	The winch operator usually from the vessel crew is required to raise and lower the OFOBS subsea unit through the water. Ideally the winch driver should be able to see the live video and image stream from the subsea unit and the operational crew should be able to communicate directly with the winch operator to ensure a suitable flight height is maintained

Table 4-1: Operational Team of OFOBS tasks and capabilities

After controlling the sensors from the subunit connection and on the top workspace PCs, the OFOBS subunit should be prepared for launching with a winch and descent to the seafloor. During PS101 the OFOBS was deployed from either the side winch or the A-frame of the vessel. The power supply should switch on after launching the OFOBS to the water and once again all the instruments are checked, and parameters are adjusted. The first sensor needed to be considered is the positioning sensors, including the top side USBL and done side transponder alignment via the acoustic pulse exchange where the Transponder on the OFOBS sends a pulse and the Posidonia USBL of the vessel receive it and sends the calculated position back to the OFOBS INS system via the fiber optical cable. The first data circulation could take up to about 5 minutes until the INS triggers the self-calibration and alignment. The alignment gets better when the OFOBS INS goes from coarse alignment to fine alignment, which could take up to about 30 minutes (IXSEA (Ed.), 2010).

In the range of about 100 m the first seafloor contact is appears in the SSS data and in the distance of the 40 meter the bathymetry data emerge. The first seafloor image is seen in the 10 to 15 meter range above the sea-floor in the video camera streams (Figure 5-10). When the OFOBS reaches the proper flight height then the towing should starts communicating with the bridge and the flight height of the subunit is kept at the proper distance (1.5 -2.5 m) via communication with the winch operator (Dreutter, 2017). The tow speed of PS101 was 0.5 to 1 knot depending on the drift speed of the ice and the flight height varied from 1.2 to 8.7 m above the seafloor in the sample area of dive PS101-169-1.

5 Study Area

The following chapter provides the outline of the characteristics of the Nansen basin in the Central Arctic as the study area and summarizes the research that has been done in the region, mainly on the Gakkel Ridge and Karasik seamount. There are also dedicated sub-chapters describing the environment and habitat property of the survey area where acoustic and camera systems of OFOBS recorded, for the first time, remarkable micro-bathymetry sonar and imagery footage of the habitat on the Karasik seamount, which is the main dataset of this thesis.

5.1 Environment Characteristics

The main expedition territory was in the region of 86°40'N and higher and 60° E. At the Langseth Ridge seamounts included the large Karasik Seamount as well as the adjacent hydrothermal mount on the Gakkel Ridge rift valley. The study area is located in the mid-Arctic Ocean, where the ocean is covered with year-round sea ice. The thickness and coverage of sea-ice changes by the seasons with September being the month when the Arctic sea ice area reaches its minimum (Seaice.Universität.Bremen, 2017), but it is still a challenging environment for deep-sea research.

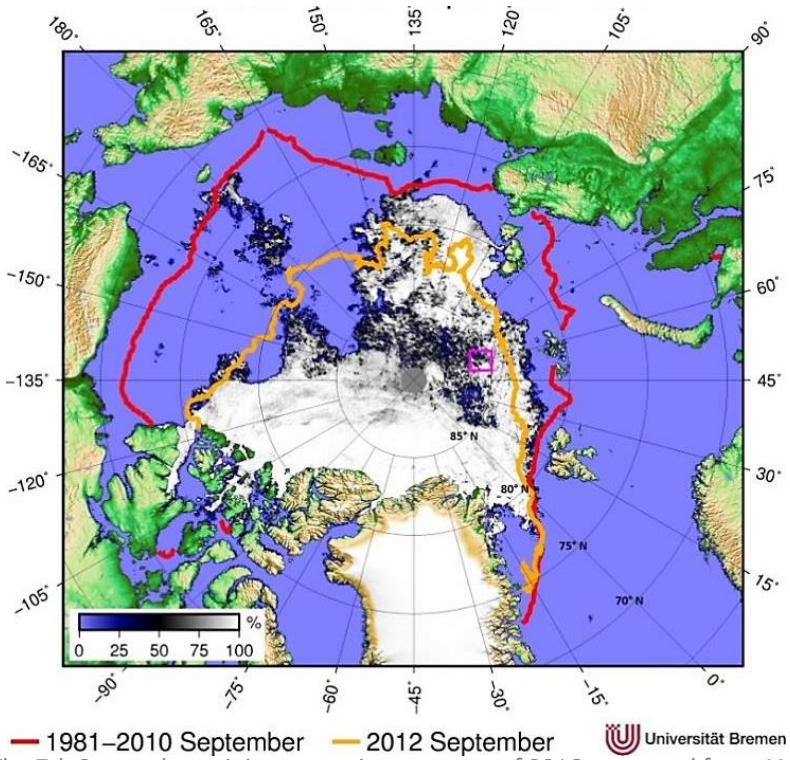

Figure 5-1: The 7th September minimum sea-ice coverage of 2016 measured from AMSR2 compared to historic summer ice extents: the 30 years (1981-2010) September mean(Red) and the lowest minimum in 2012(Orange) (Seaice.Universität.Bremen, 2017). The PS101 study area is highlighted in the purple.

Figure 5-2; RS Polarstern at 6th of the October 2016, close to the northern slope of the Langseth Ridge at 9:31 AM, A short window of good weather followed by extremely difficult ice conditions and poor visibility. (Courtesy of Simon Dreutter / AWI)

Operation of deep-tow systems is highly limited by mean of steering and navigation in sea ice condition and requires a certain level of concern. In the case of the operation of the flank crane, the side forces of the ice to the vessel hull might cut the cable and connections of the system or even loose of vehicle. Therefore, OFOBS mostly was towed from the stern side of the Icebreaker over the A-frame during PS101 dive operations, where the propellers wash keeps ice floes away from the cable, nevertheless there is still a high risk of scissoring by thick ice floes when the vessel suddenly stops during icebreaking. That makes the sea ice characteristics a preliminary factor for OFOBS dive planning as well as ice-drift speed and direction (Dreutter, 2017).

5.2 History and Background

The very early bathymetry data for the Arctic Ocean basin was acquired during the first Fram expedition in 1893–1896. Fridtjof Nansen and his team changed the speculation of large continental land-masses beneath the Ice. The compiled chart depicted by a few lead line sounding, shows a featureless single deep basin beneath the sea ice of the Arctic ocean. The portrait of a single deep basin in the Arctic Ocean abyssal plain consisted for about sixty years after the Fram drifted across the polar sea (Weber, 1983).

Even the 1941 airborne expedition to the Pole by Soviets neither proved nor disproved the one-basin concept till 1948 by the discovery of *Lomonosov Ridge* which was an outset for the first modern map that shows the Arctic Ocean divided into two basins in 1954 (Weber, 1983).

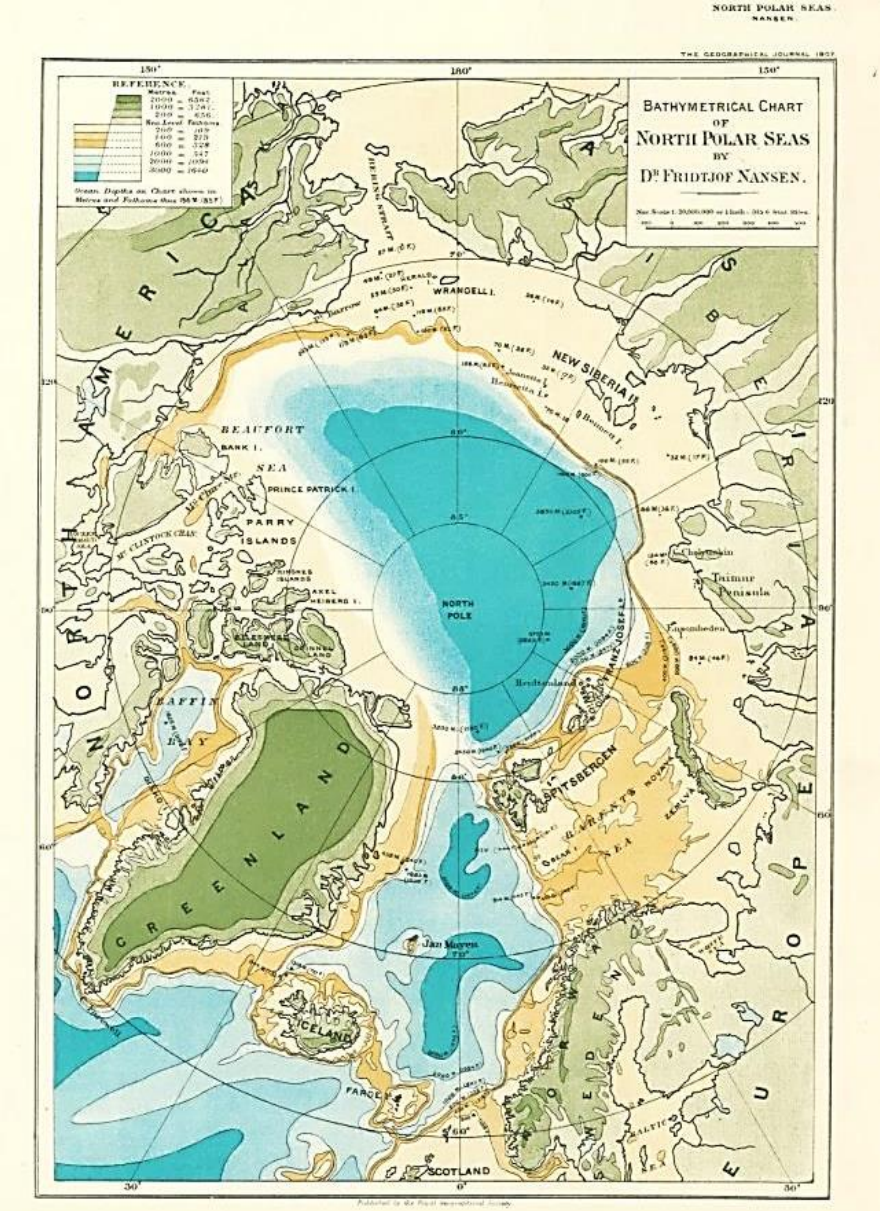

Figure 5-3: Bathymetrical Chart of Northern Polar Seas (by Dr. Fridtjof Nansen) denotes Arctic Ocean with a single basin. Throughout the Fram expedition, Nansen kept the crew busy carrying out scientific measurements, including ocean depth soundings. This bathymetrical map of the Arctic Ocean was one of many scientific results published after their return (Fridtjof Nansen Institute, 1999).

More detail and features brought to the charts came from expeditions happening between the 1950s until the 1970s collected by U.S submarines and airborne, along with the Canadian Polar Continental Shelf Project (PCSP) which was Long-range planning for systematic bathymetric and gravity mapping (Weber, 1983).

More complex bathymetric landscapes have formed from the tectonic evolution of the Arctic Basin, ocean currents and glacial history and have been subsequently collected in numerous

surveys for a variety of maps and projects by several nation involved ad interested in the research, military and commerce expansion (Jakobsson et al., 2012).

In 1967 the Canadian Hydrographic Service put all the major physiological features that had been discovered on the first official chart in preparation for the first General Bathymetric Chart of the Oceans (GEBCO) which was compiled and published a year later (Weber, 1983).

Almost one century after the Fram Expedition, in 1997, one of the International Bathymetric Chart (IBC) Mapping Projects, sub-project of GEBCO, aimed to develop a digital database for the Arctic region, named IBCAO, in order to contain all available bathymetric data north of 64° North, for users whose work requires a detailed and accurate knowledge of the depth and the shape of the Arctic seabed. (Jakobsson et al., 2012)

The third version of the International Bathymetric Chart of the Arctic Ocean (IBCAO) grid and chart was published by the June of 2012, which this thesis is also benefiting from along with data acquired during the PS101 cruise.

Germany was involved in the Arctic research at the end of the 1860s by Carl Christian Koldewey who led two expeditions to the east coast of Greenland and *Sabine Island*. The first expedition did not lead to much new scientific knowledge and explored only a few unknown coastal areas in northeast Spitsbergen. The second expedition with two schooners vessel had several achievements. The convoy ship (*Hansa*) sank in the third month of the expedition, but the main ship (*Germania*) managed to carry on and conduct a series of valuable observations and measurement. The Second Expedition resulted in several geographical and cartographic surveys of northeast Greenland, and also geological, glaciological, glacial geomorphological, zoological, botanical and archaeological studies were conducted during the 435-day voyage. In addition, extensive astronomical, geophysical, and geomagnetic measurements were carried out which later played an important role in the development of Alfred Wegener's theory of continental drift (Venzke, 1990).

The new race of the Deutschland polar expedition started around 1980s by the “Alfred Wegener Institute, Helmholtz Centre for Polar and Marine Research” (AWI) with the three major divisions being the Geoscientific Department, Climate System Department and Biosciences Department along with several special groups. AWI has a close cooperation with numerous national and international partners in order to decipher the complicated processes in the "system of earth". This topic research is a cooperation of AWI bathymetry group and Bioscience department and the data collected during the PS101 cruise of AWI icebreaker RV Polarstern.

5.3 Geographic Setting of the Investigation Area

The Karasik seamount is situated on the Langseth Ridge and was the main target of the research area for the PS101 cruise, along with the vent mount in the Gakkel Ridge Rift Valley. Both of these under water features are located in the central Arctic Ocean.

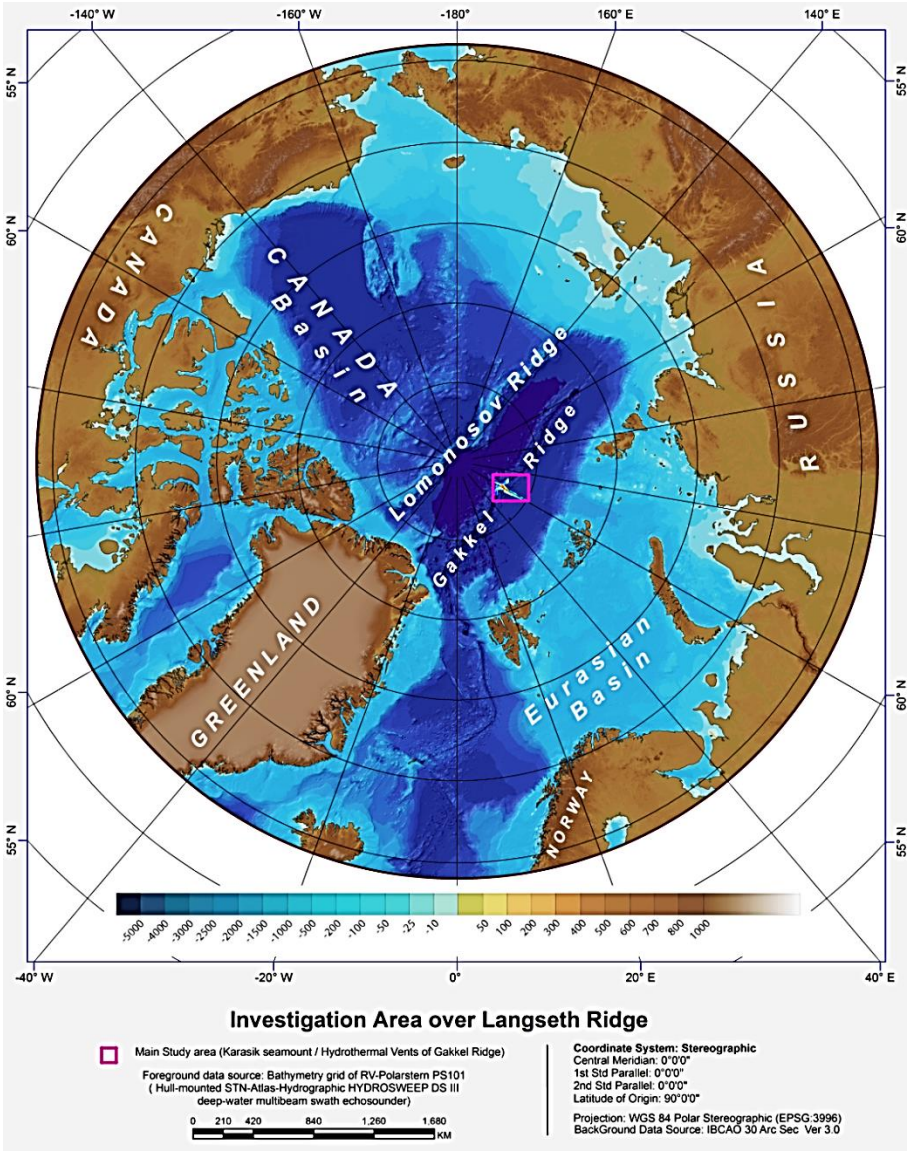

Figure 5-4: Overview of the Lomonosov Ridge and Gakkel Ridge as a complex Arctic Mid-Ocean between the North American and Eurasian tectonic plate. The main research area of PS101 cruise (purple box)

The main area investigated is in the region of 87° N and 60° E. Both structures were discovered during the Arctic Mid-Ocean Ridge Expedition (AMORE) during the 2001 expedition, a joint cruise with two icebreakers, the Polarstern and the Healy (Boetius & Purser, 2017). The preceding oceanographic observations by the submarine in 1999 indicated reginal volcanism and hydrothermal activities along large axis-perpendicular of the Gakkel Ridge.(Thiede, 2002),(Sohn et al., 2008).

The Gakkel Ridge (position 83°30'N - 6°00'W to 81°00'N - 123°00'E) formerly recognized as “Nansen Cordillera” or "Arctic Mid-Ocean Ridge" is the slowest spreading portion of the global mid-ocean ridge system. Total spreading rates range from 12.7 mm/yr. near Greenland to 6.0 mm/yr. where the ridge disappears beneath the Laptev Shelf (Cochran et al., 2003). The ultraslow divergent boundary is an 1,800 kilometers mid-oceanic Ridge of the Eurasian and the

North American Plate which touches the end of the Mid-Atlantic Ridge at northeast of Greenland.

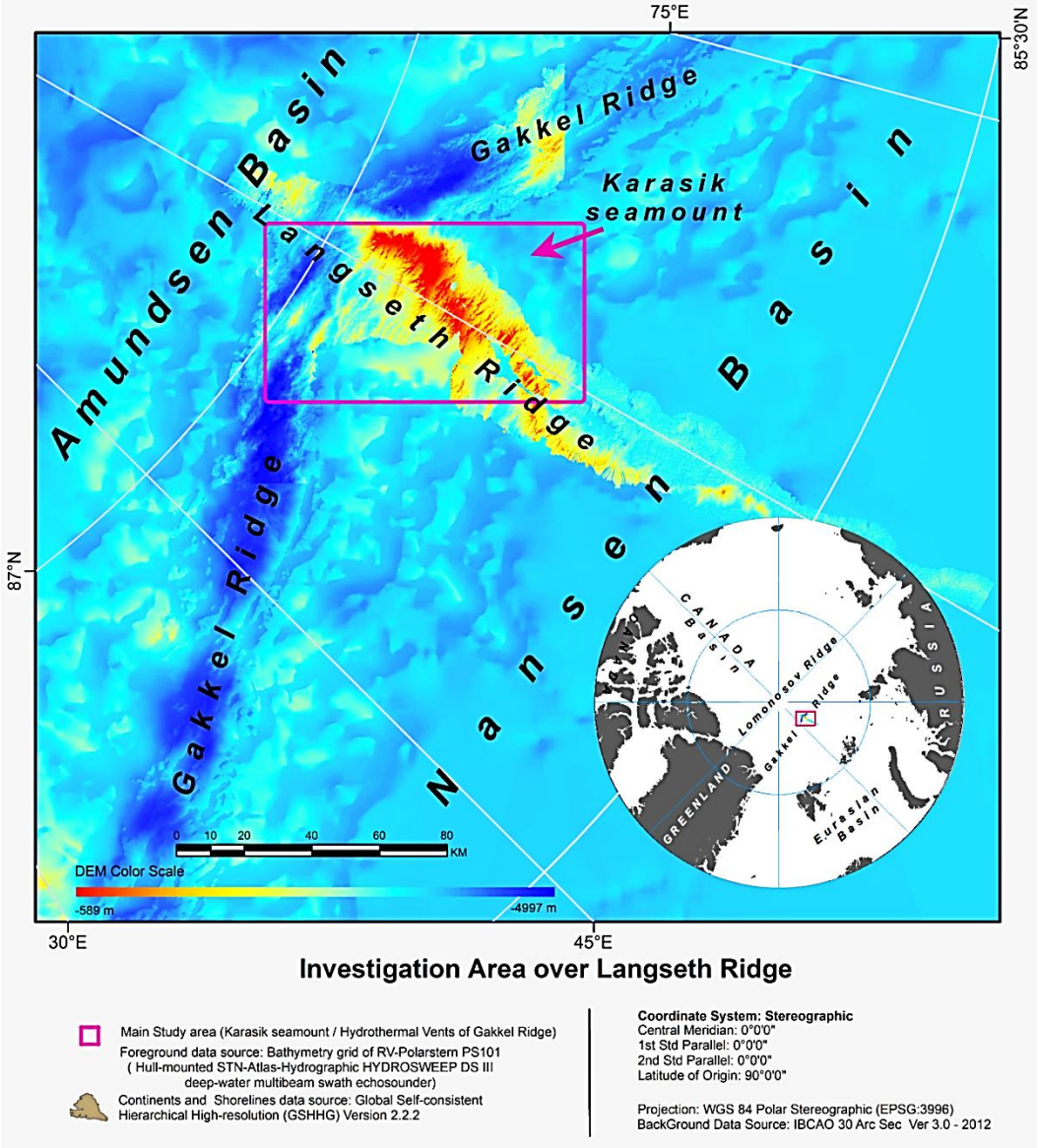

Figure 5-5: The Langseth Ridge intersected with the Gakkel Ridge perpendicularly. The purple box representing the main investigation area of PS101 research cruise. Data sources are (IBCAO) Ver. 3.0(Jakobsson et al., 2012), (GSHHG) Version 2.2.2, High resolution multibeam bathymetry of RV-Polarstern during PS101 (Dorschel & Jensen, 2017)

The transarctic Ridge was discovered during Soviet high-latitude Arctic expeditions (1948-1953) and mapped in 1954. The ocean floor feature is named after a reputed Russian Arctic explorer and oceanographer *Dr. Yakov Yakovlevich Gakkel* who predicted the existence of the Ridge in 1948 and six years later collected bathymetric, hydrological and benthic data and made the first contour of the Ridge on the chart (Sohn et al., 2008),(IOC-IHO GEBCO SCUFN-XV/3, 2002).

Along 1,800 km length of Gakkel Ridge, there are several intersecting axes crossing from one side of the Gakkel Ridge to the other side.

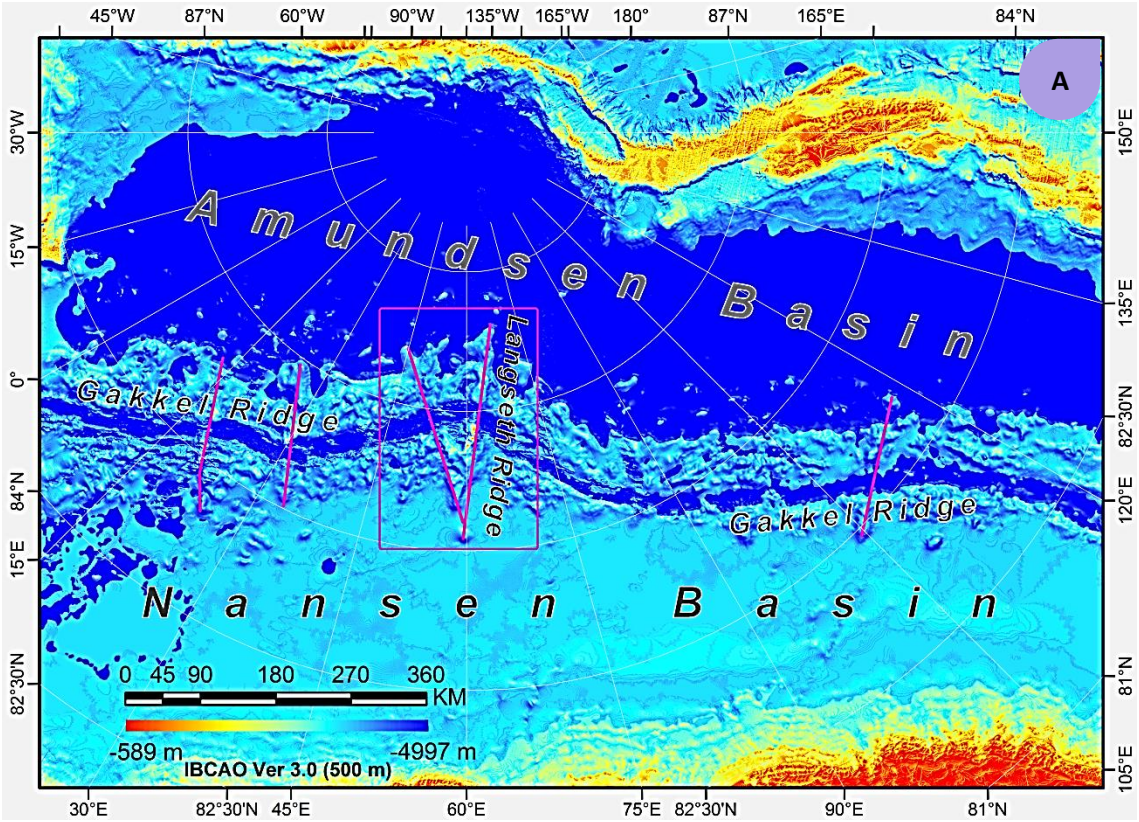

Figure 5-6 (A, B): The Hypothetical "V Shaped" extent of Langseth Ridge (Purple Box) is perpendicularly crossing the Gakkel Ridge relatively in the mid-arctic ocean is one of the several axes bisect the Gakkel Ridge.

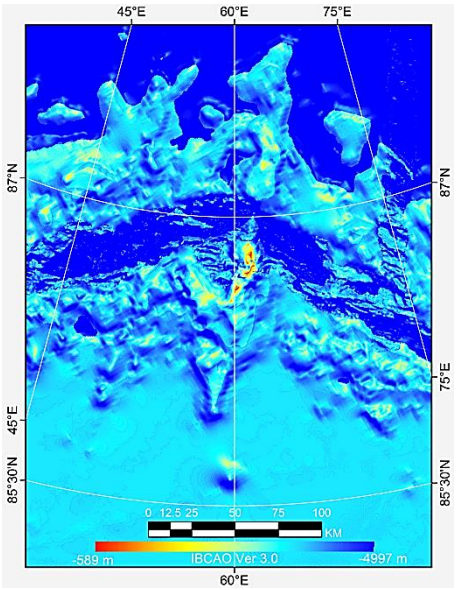

The Hypothetical "V Shaped" extent of Langseth Ridge is perpendicularly crossing the Gakkel Ridge and extended from both side while the major elevated part of the Langseth Ridge is located in southern side (Boetius & Purser, 2017).

The Ocean Relief Feature stretches from 87°N 62°' E to 85°55'N 57.45'E, it has been defined as an undersea mountain structure during the sixteenth meeting of the GEBCO Sub-Committee for Undersea Feature Names (SCUFN). The Langseth Ridge is named after the American geophysicist Dr. Marcus Gerhardt Langseth who designed the Arctic Basin submarine scientific research program in the 1990s, however, the elevated feature was discovered by Soviet scientists in 1965 and appears

on a geological map and nautical chart from the soviet union in the same year (IOC-IHO GEBCO SCUFN-XV/3, 2002) (IOC-IHO GEBCO SCUFN-XV1/3, 2003).

According to the provided coordinates and information in the fifteenth and sixteenth SCUFN meeting reports the Langseth Ridge is described as a “Relief: 2000 m; least depth: 566m” (IOC-IHO GEBCO SCUFN-XV1/3, 2003) located on the Nansen Basin side of the Gakkel Ridge , 124,4 kilometer long, while the latest Multibeam hydroacoustic bathymetry of PS101 expedition raised a hypotheses of a “greater Ridge system” in a “V Shape” which could indicate that the Langseth Ridge extends on both sides of Gakkel Ridge and also is prolonged to the south but needs further geological analysis (Boetius & Purser, 2017). (Figure 5-3)

Along the Langseth Ridge several Peaks were discovered by Soviet scientists in 1965, and later proofed by USS Hawkbill data in 1997-1998. Some of them are officially named and some are still under the appellation. The sixteenth meeting of the GEBCO Sub-Committee for Undersea Feature Names (SCUFN) officially accepted one of these summits as the Karasik Seamount, named after Arkady Moiseyevich Karasik (1930-1987), a Russian geophysicist who led aeromagnetic studies and expeditions in the Arctic. The Karasik Summit is defined as the shallowest feature in the northern part of the Langseth Ridge. The official description on SCUFN describes Karasik seamount as a 2000m Relief with the lease depth of 556m, located at 86°43.0'N 61°17.6’E (IOC-IHO GEBCO SCUFN-XV1/3, 2003) while the PS101 survey measured 584.8 meters below sea level for maximum elevation of the area with about 1.5 km south west of the accepted summit location(IOC-IHO GEBCO SCUFN-XV1/3, 2003; Boetius & Purser, 2017).

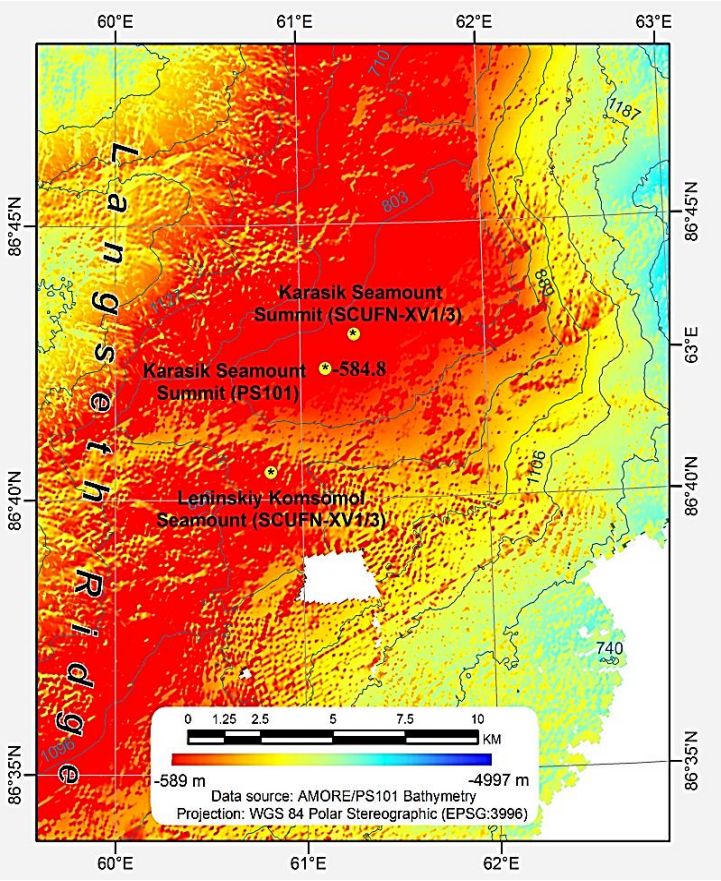

Figure 5-7 : Comparison of the position and lease depth of the Karasik seamount measured during PS101 expedition with official property of the two accepted feature by SCUFN-XV1/3

The first swath bathymetry of the Karasik seamount was during the AMORE cruise which added more detail to the initial survey. The previous bathymetry data represented the Karasik as one individual seamount while the recent PS101 swath bathymetry reveals two new individual

peaks and saddle in addition to the Karasik Summit. Figure 5-8 demonstrates the location and the unofficial names for these new features which could be identified on the higher mountain range of the Langseth Ridge.

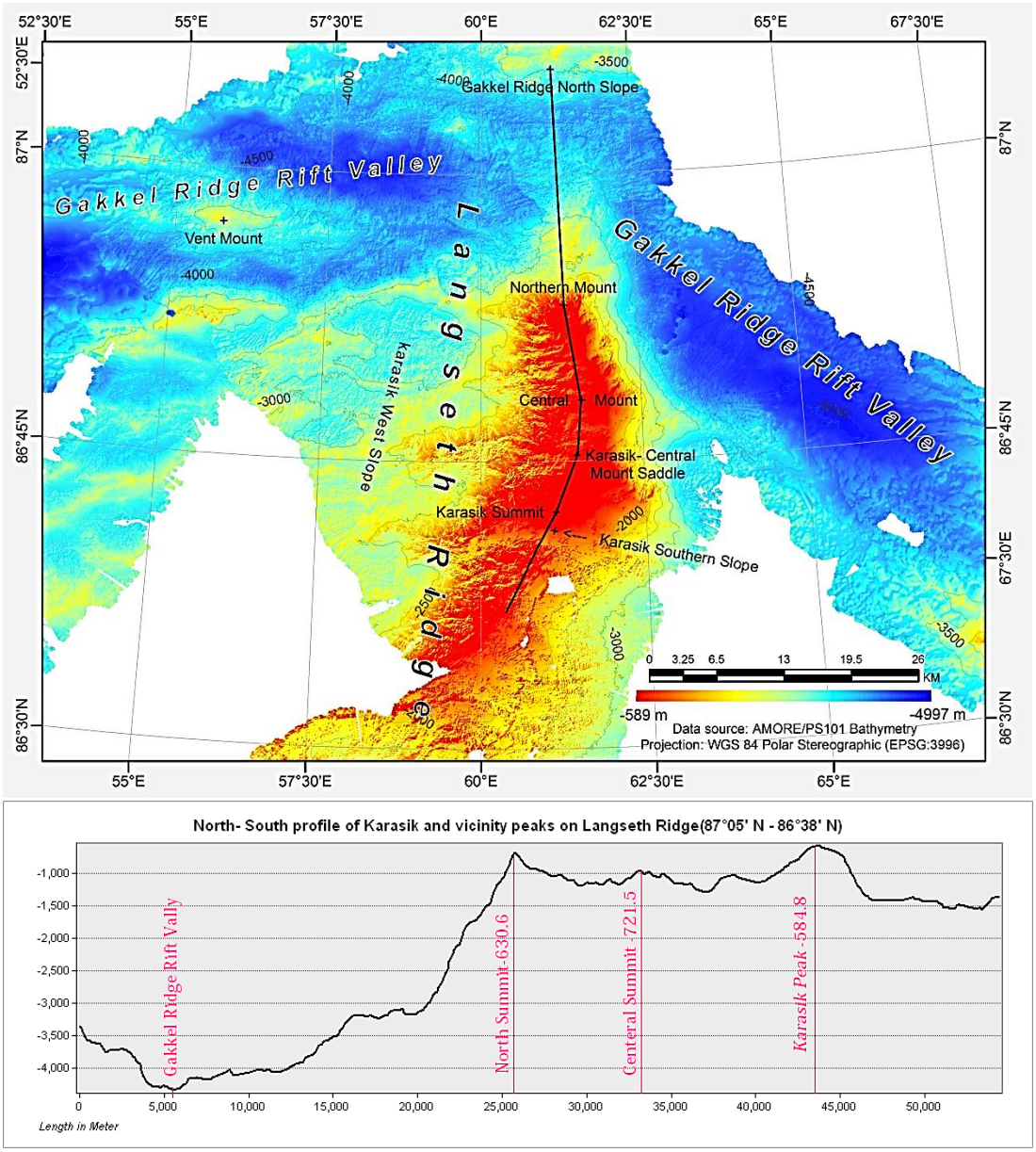

Figure 5-8 : Seamounts of Langseth Ridge and adjacent Vent Mount peak on Gakkel Ridge Rift Valley over AMORE and PS101 SHIP bathymetry (Top). North-South profile of Karasik and vicinity peaks and saddle from 87°05' N to 86°38' N (Bottom)

As the bathymetry profiles indicates, the Karasik seamount remains the highest peak on the Langseth Ridge while the existence and position of the Leninskiy Komsomol Seamount at the given position of SCUFN-XV1/3 is not confirmable with the hydroacoustic survey from the PS101. The nearest possible feature of the missing seamount is 14 kilometers southwest of

the Karasik Seamount at the location of 86°36.0'N 60°8.39'E and climbs 1,015 meters above the surrounding seafloor, which is 3,200 meters deep (Boetius & Purser, 2017).

5.4 OFOBS Dives Stations and Sample Area

A big portion of the PS101 expedition was dedicated to visually determining the geological, sedimentological and biological community structures across the surveyed area. The OFOBS was one of the instruments used along with TV Multicore and ROV on board the RV Polarstern. The OFOBS was deployed as imaging systems for recording the video and still images from several meters above the seafloor while the Sonar extension was sounding the several meter beneath the system (Boetius & Purser, 2017). The current sub-chapter is describing the OFOBS dives in the study area.

During PS101 expedition fifteen OFOBS dives were successfully carried out. Most of the dives were around the unofficially named Vent Mount of Gakkel Ridge Rift Valley (eight dives) and Karasik Seamount and toward the North Mount (four dives). Brief information and locations of the OFOBS dives is given in table 5-1. The dataset used for this thesis is from the north part of the PS101/169-1 dive which is located in the Central Mount along Langseth Ridge, north said of Karasik Seamount.

Station name	*Region*	*Duration*	*Planimetric Length*
PS101/010-1	(Test Site)	1:07	1222 m
PS101/068-1	(Test Site)	2:32	2052 m
PS101/089-1	Karasik Seamount	5:23	6109 m
PS101/100-1	Central Mount	2:54	5254 m
PS101/120-1	Northern Mount	5:11	7308 m
PS101/134-1	Vent Mount	1:11	3476 m
PS101/135-1	Vent Mount	4:08	6998 m
PS101/158-1	Vent Mount	5:20	8763 m
PS101/169-1	**Central Mount**	**4:16**	**5370 m**
PS101/179-1	Vent Mount	2:07	3226 m
PS101/185-1	Vent Mount	1:27	3091 m
PS101/225-1	Vent Mount	5:39	3719 m
PS101/229-1	Vent Mount	2:00	4069 m
PS101/232-1	Vent Mount	2:08	2831 m
PS101/241-1	Yermak Plateau	1:23	3139 m

Table 5-1: List of the OFOBS Dive of PS101 expedition. The Dataset of this thesis is North side of the PS101/169-1 OFOBS dive (Highlighted)

The OFOBS dive of Central Mount named as PS101/169-1 started on the 30th of September at 20:26" Coordinated Universal Time (UTC) and at the depth of -878 meter below mean sea level (86° 45.67' N ,061° 51.86' E). The total duration of the dive was four hours and sixteen minutes

and the length of the dive was 5,370 meter (Boetius & Purser, 2017). The dataset used for this specific study was the last 500 meter of the dive where the OFOBS towed from Karasik-central Mount Saddle toward the Central Mount summit.

The following map is representing a general overview of the four OFOBS dives at the Karasik seamount and the specific dive number PS101-169-1. The white box is highlighting the dataset used for sponge detection in this paper.

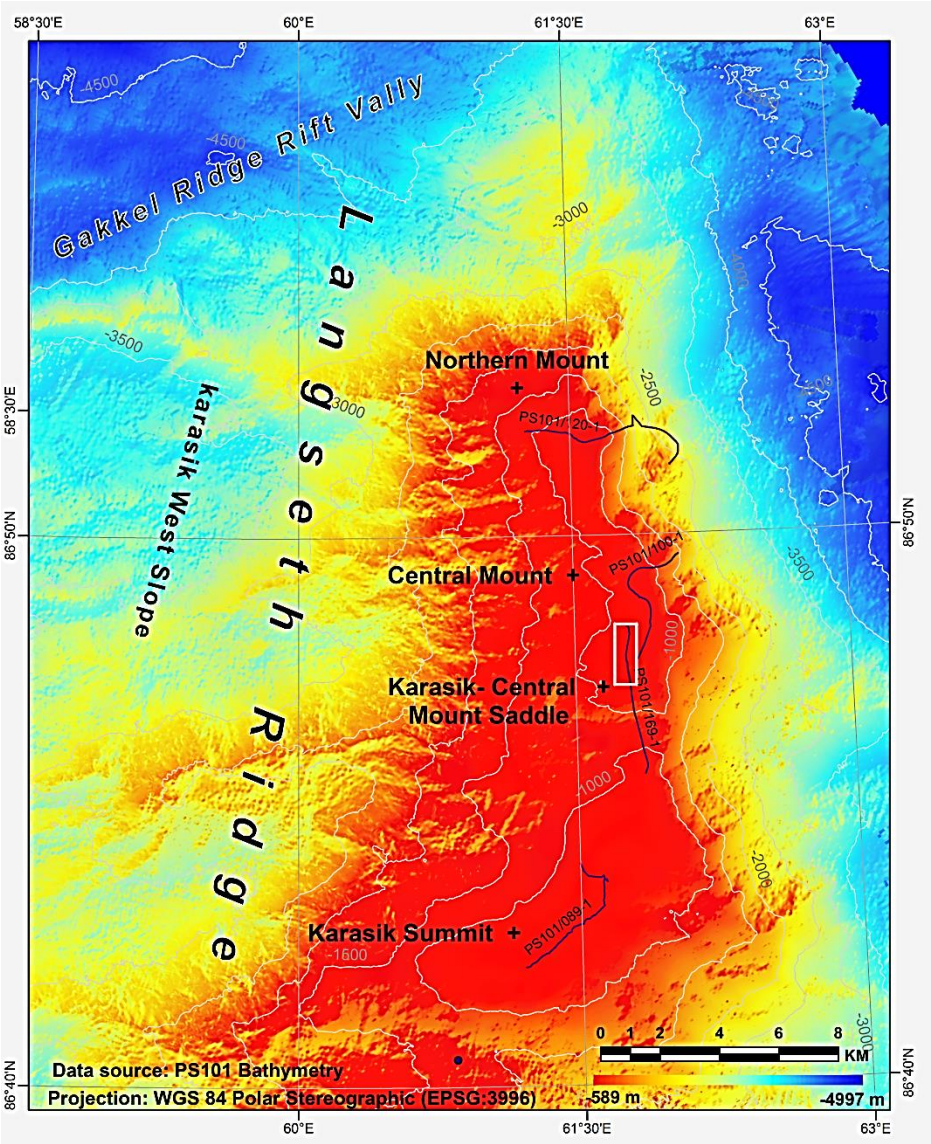

Figure 5-9: Overview of all the four OFOBS dives at Karasik Seamount and the boundary of the thesis dataset (White Box)

5.5 Habitat Characteristics

The OFOBS dives PS101/089-01 surveyed Karasik Seamount, the imagery system showing a dense forest of sponges and sponge spines at the summit. There were several breaks in the sponge cover toward the northern section of the mount summit, where a thick layer of dead tube worm tubes was intermixed with dead mussel, clam and gastropod shells, as well as small pebbles and sand. Also, two individual dives of PS101/100-1 (Central Mount) and PS101/169-1 (Karasik-Central Saddle) on the Langseth Ridge showing similar sponge communities on both dives compared to the Karasik summit but the accumulation and sponge cover on the central mount is lower in general, and the abundance of sponge spines between sponges was less.

More detailed visual interpretation of the OFOBS footages is given in the PS101 expedition report, generally indicating a multifarious distribution of the sponges over the Langseth Ridge seamounts.

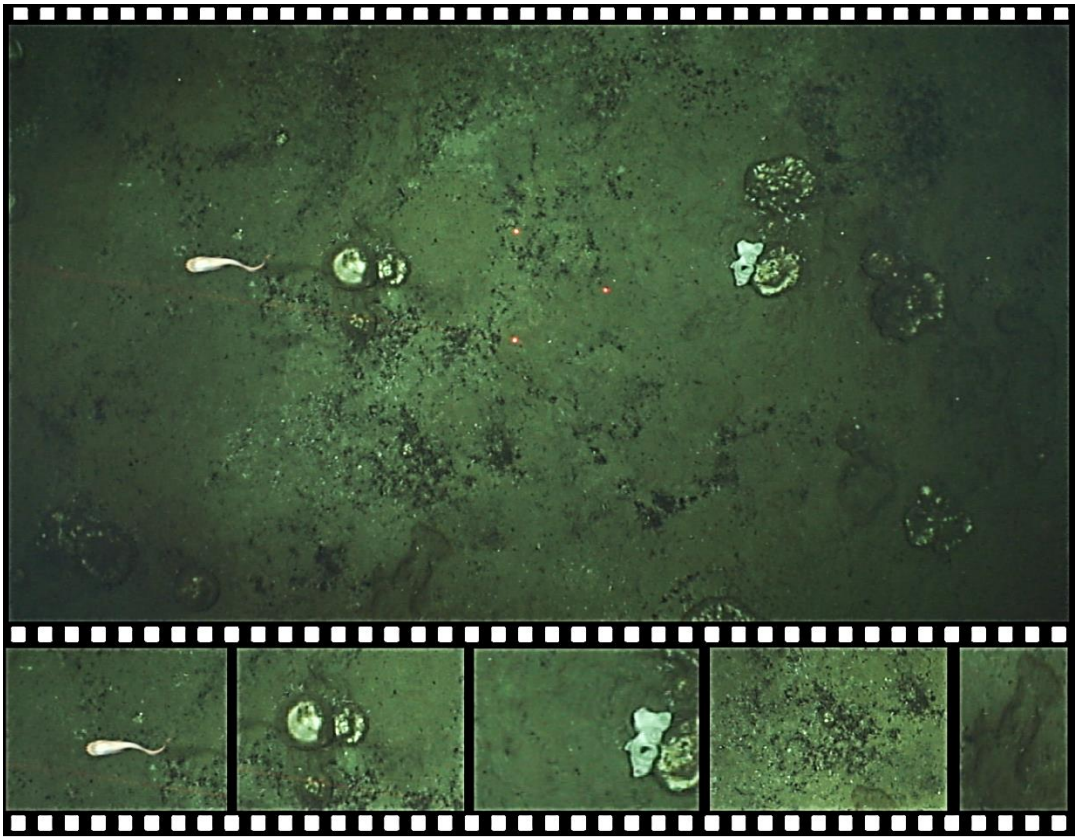

Figure 5-10: While the OFOBS is descending to the central mount surface, the very first video footage fading in a distinct biodiversity of the central seamount at the depth of ~800 meter. From right to left there are unofficially named: Arctic pink snail fish, twine Geodia sponges, Glass sponges, dead tube worm tubes, sponge spicules mats (OFOBS dive PS101-169 September 30th, 2016).

The saddle flanks were both populated by tubeworms however on plateaus the astrophoroida sponges and are colonies. The saddle is mainly covered with a thick layer of Geodia sponges'

spp., with infilling mix of dead Polychaeta and needles were replaced by a lower density of sponges and mixture of sponge spicules and sand, infrequent small stones and rocky outcrops.

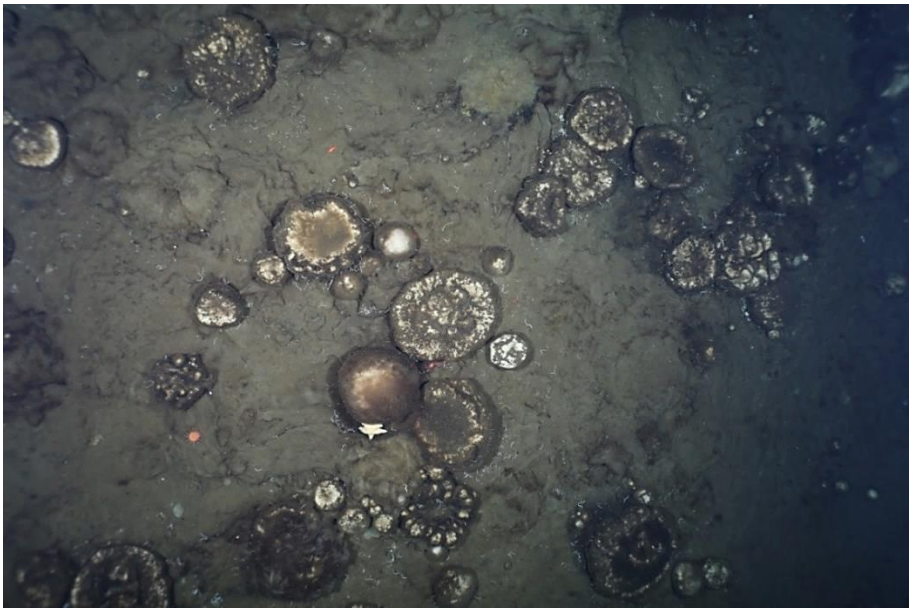

Figure 5-11: Still image collected on OFOBS dive PS101-169 indicates biodiversity at Karasik seamount at the depth of 500 to 1500 meters, the Geodia sponges setting at the seafloor surrounded by infilling material of sponge spines.

At the utmost of the central peak the majority of the seafloor is covered with the dead Polychaeta worm casts, a strata of several centimeters thickness covering below and top of the sponges. The thickness of the black areas is denser in some regions with regards to the worm casts accumulation.

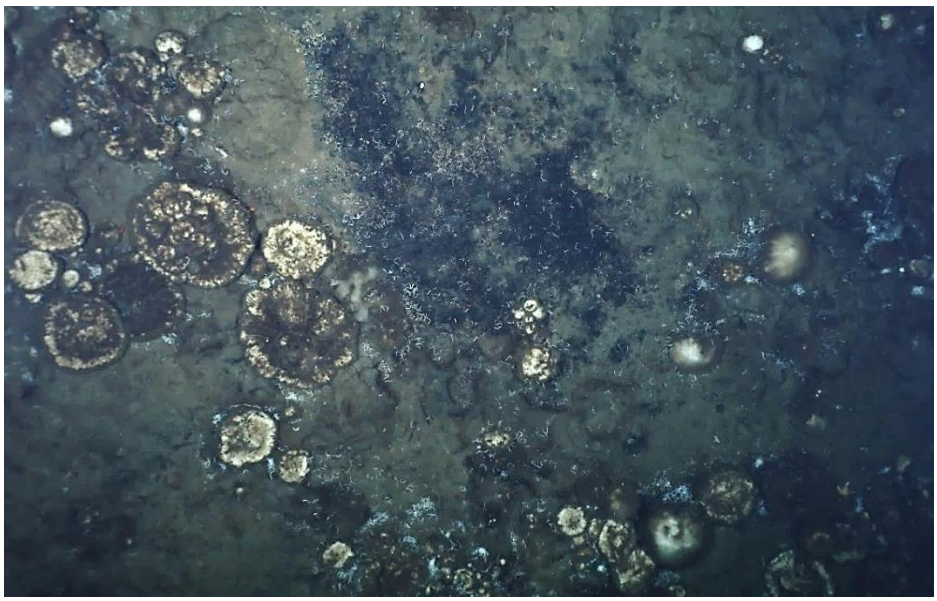

Figure 5-12: Still image collected on OFOBS dive PS101-169. The black area in the middle of image is the accumulation of Polychaeta worm and their casts.

In addition to that, there are white-spotted sponges in the scene, and white-yellowish microbial mat growing on decaying dead/dying sponges, spicules of sponges as well as sponge tracks on the seabed. (Boetius & Purser, 2017)

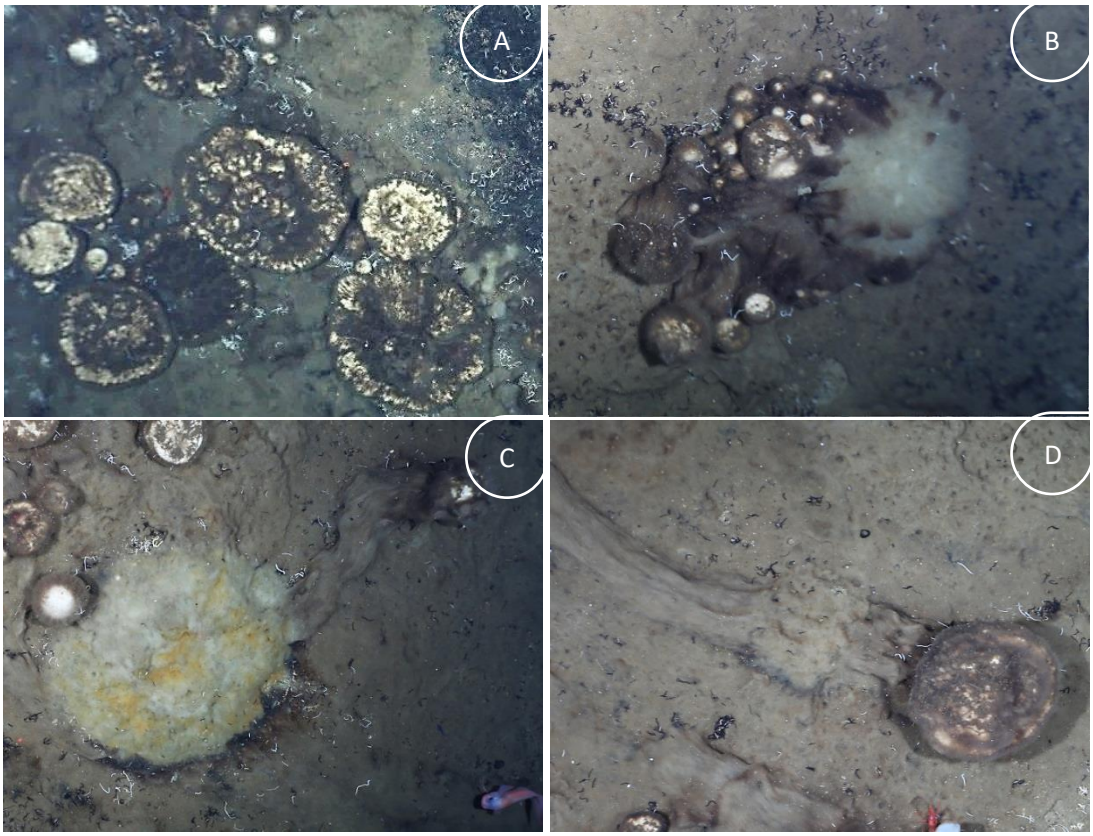

Figure 5-13:Diversity life stage of Geodia spp. is captured in OFOBS footage, (A)group of white-spotted sponges, (B) layer of bacteria mat and sponges spicules matte covered a group of sponges, (C) white-yellowish decaying giant sponge, (D)A Geodia spp. sponges and its track

Footage of the saddle revealed that the seafloor is dominated by Geodia spp. and Stelletta spp. sponges but scarcely there are glass sponges of several distinct species beside them.

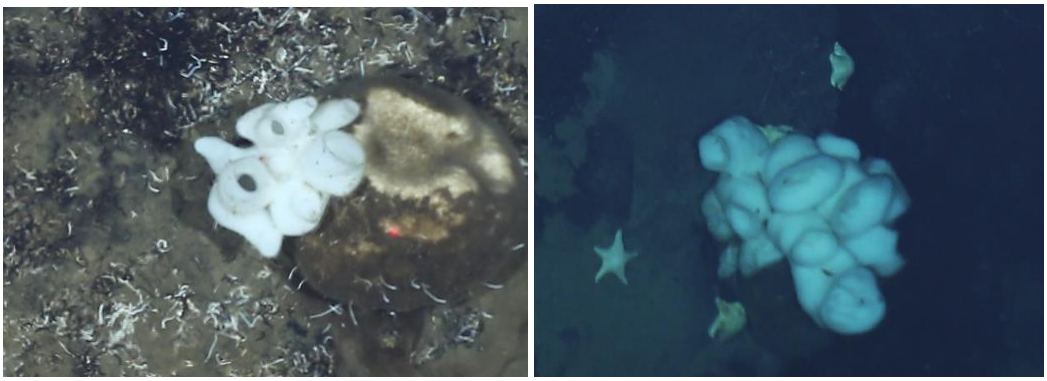

Figure 5-14: (Left) a vase-shaped Glass sponges in the saddle area beside a Geodia sponge spp. (Right) a giant glass sponge spp. In the slope of the central mount as they could be found in the Northern mount.

In the surveyed area of the saddle and central mount, many other distinct fauna categories were also present in the cameras footage. The most common view are " Crustacean gathered around or beneath of the sponges" or " group of the Starfish crawling ups the sponges and seemingly are feeding upon them where the sponges are usually covered by a white bacterial mat". (Boetius & Purser, 2017)

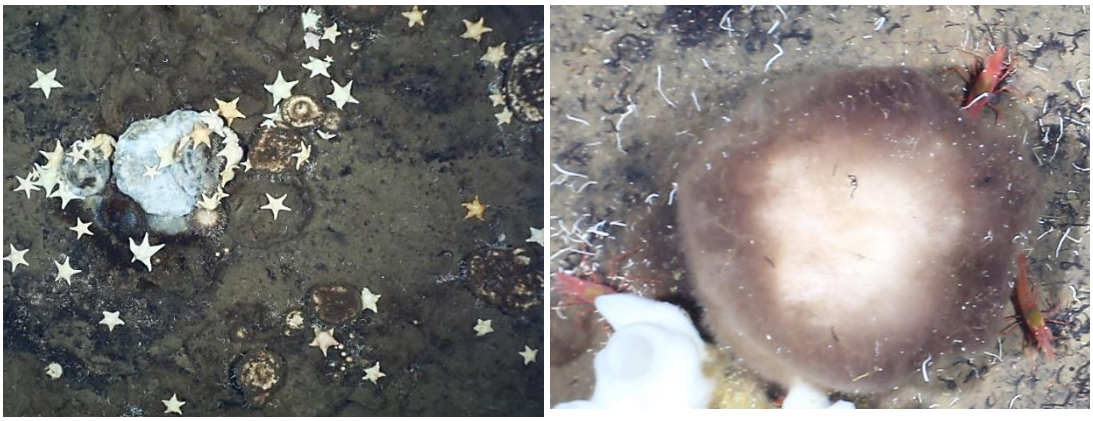

Figure 5-15: The starfishes, shrimps are appearing around either on a sponge or the bacterial matt. (Left) "Cushion star" starfish were commonly observed feeding on the dead remains or bacterial growth upon the dying/dead sponges (Right) while the shrimps are mostly shelter under the steady sponges

Irregularly there were snail pink fish and gray/purple fish encountered during the dive at Karasik peak.

Figure 5-16: Two distinct species of the fishes dominantly appearing in the cameras footages during the OFOBS dive PS101-169 in the saddle and said flanks

In some sponge colonies there are also anemones sitting on sponge tops or suspended in the water column. The Ophiuroids mostly appearing where the tubeworm debris or spicule mats are prevailing.

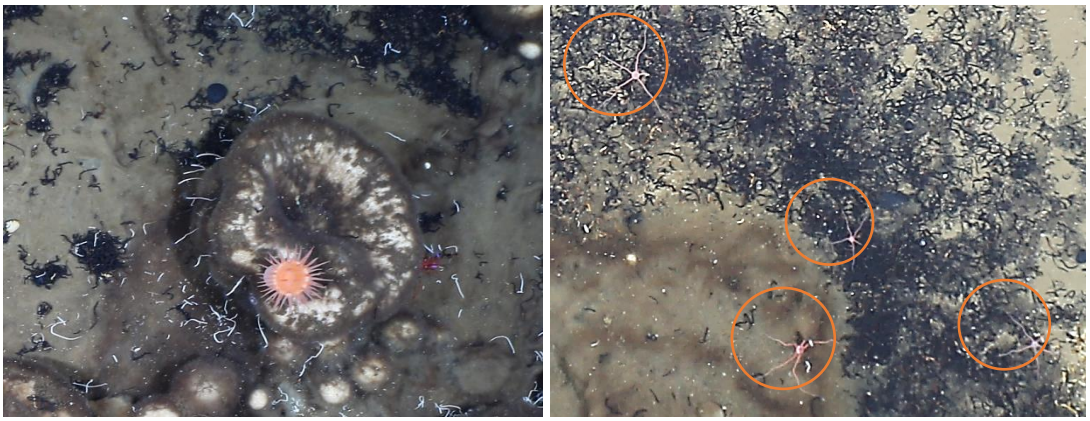

Figure 5-17: (Left) Usual picture of anemones setting on the Geodia sponges ssp. (Right) Four individual Ophiuroids setting at the mixture of tubeworm debris and spicules mats (Red Circles).

Sponge spicules mats area surrounds almost all the sponges' colonies with different thickness, also in some areas sponges are sinking in the accumulation of the Spicules mates.

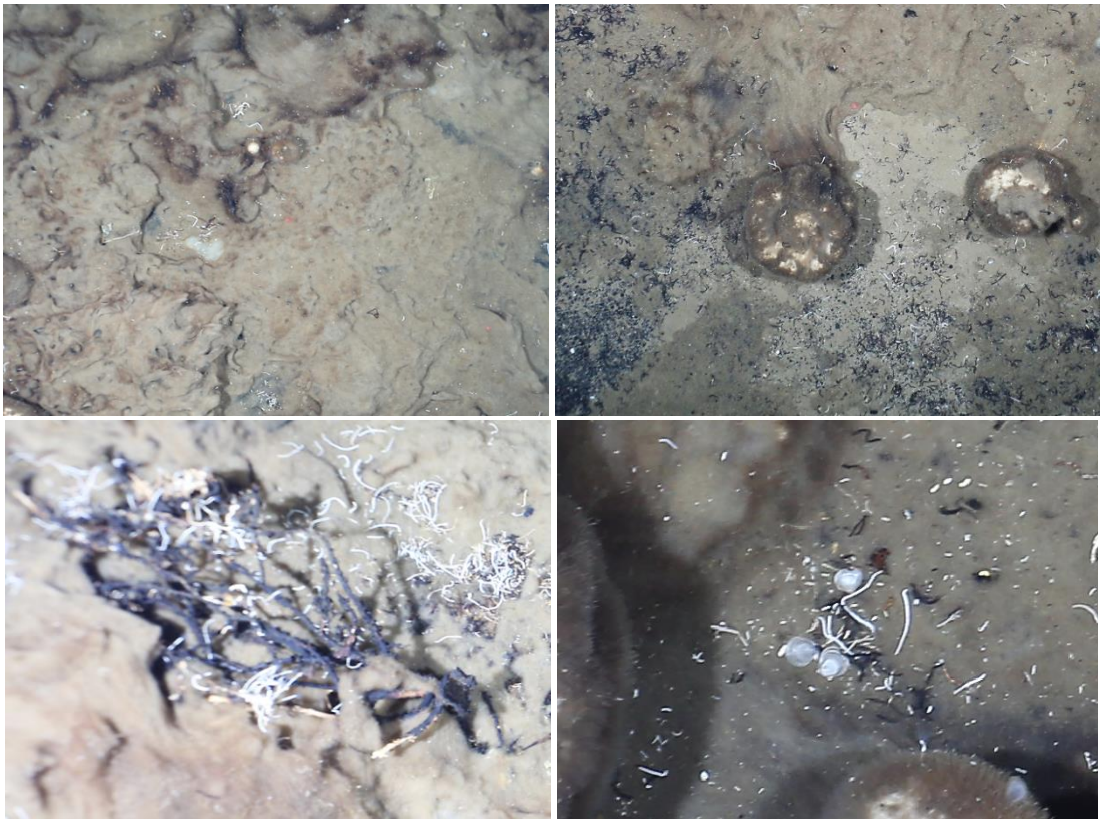

Figure 5-18: Sponges spicules mats with the different thickness.

6 Materials

The materials used in this study come from three different sources; 1) the publicly-available datasets 2) the vessel-based datasets 3) the OFOBS-based datasets.

The vessel-based and the publicly-available datasets are the secondary data sources for this study, they were used for overall mapping of the study area on chapter 5, while the OFOBS data sets (imagery and acoustic) were employed for feature detection of the habitat mapping, on chapter 6 to 10. In this sub-section the characteristics of the materials are described, and the methodology is delineated in the data processing chapter. The imagery data set of the OFOBS is the main data set which is described in sub-chapter 6.3.1 and 6.3.2.

6.1 Publicly-Available Datasets

IBCAO:

The International Bathymetric Chart of the Arctic Ocean (IBCAO) is an international project associated with 24 institutions in 10 countries (up to 2017), in order to develop a modern data base for the Arctic north of 64° North, which provides the latest available bathymetric data for those who requires accurate and detailed knowledge of the depth and the shape of the Arctic seabed features for their projects and researches.

This thesis benefits from the latest updates of maps and grids realized in mid-2012. The version 3.0 takes advantage of the new data sets. About 11% of bathymetry data is covered by multibeam surveys, mostly from research vessels and Navy submarines, collected by the circum-Arctic nations. The new dataset is on a 500 meter spacing enhanced by an advanced gridding algorithm (Jakobsson et al., 2012).

GSHHG:

Global Self-consistent, Hierarchical, High-resolution Geography Database are amalgamated vector files, from three public domain data bases which all together provide spatial data for the shorelines and water bodies (from ocean to lakes and rivers), Antarctic Ice-front or Grounding line as well as political borders. The data sets are available in 2 formats, Esri shapefiles and native binary files. The geography data files are available in five resolutions, Shorelines are furthermore organized into 6 hierarchical levels, while rivers come in 10 classification level and borders are provided in 3 levels. The maps in chapter 5 are the latest released version 2.3.7 in June of 2017 (GSHHG, 2017).

6.2 Vessel Bathymetry Dataset

The acquired data of the multibeam echosounder (MBES) was initially processed on board using *Caris HIPS and SIPS* (Caris (Ed.), 2016). The post processing data took place at the AWI Geophysics / Bathymetry department (Bremerhaven) after the expedition by manual editing, and matrix-based median filtering. The final cleaned data was exported into xyz soundings and bathymetry grid at 100 m resolution. The overall MBES HS DS3 data recorded during PS101 exceeded 4300 km^2 in the Nansen Basin and Gakkel Ridge, which is available in the scientific data warehouse PANGAEA (PANGAEA-PS101-Datasets, 2016). The bathymetry grid of the Gakkel Ridge and Karasik seamount is used for mapping purposes in chapter 5.

6.3 OFOBS Datasets

During OFOBS dives different sensors were collecting various datasets continuously (video and sonar) or at certain intervals (still images). All unprocessed data is named here as “Raw data” including multi-sensor navigation data and imagery data sets as well as sonar data. The first set of processes is meant to combine “Raw datasets” together, in order to enrich the position accuracy and the overall value of the geospatial and mapping material for the further process. This part of the data processing was carried out during an earlier stage of the project and is explained in detail in Dreutter (2017).

In order to provide a better picture of datasets involved in this study, the main process chain is broken down into several distinct steps, the output of each step is the input for the next one. Therefore, the relevant materials are sorted into individual batches, and in this chapter the properties of each are considered. The following graph represents the respective data of each step.

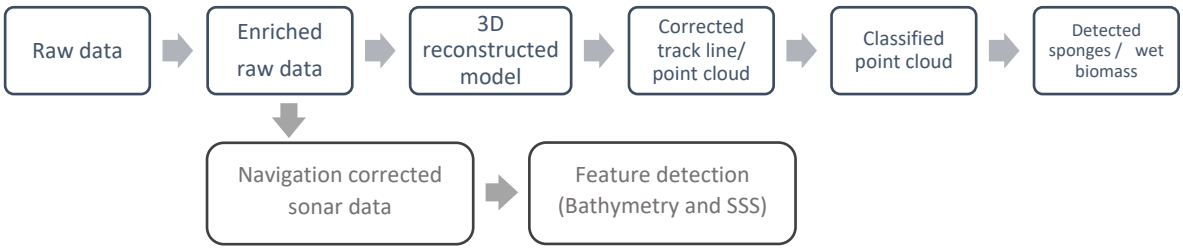

Figure 6-1: Outputs and material of process steps.

6.3.1 Raw Data Structure

The OFOBS datasets could be categorized in three classes: sonar, imagery and Navigation datasets, while some data are merged in the other datasets but also stored individually.

Raw Navigation data

It is worth noting that some of the sensors and relevant datasets have a dependency on the other instrument outputs. Specifically, the position strings of the OFOBS have several affiliations on other instruments such as GPS and vessel IMU passed out to OFOBS where the failure or disconnection of one of the instruments has an influence on the data quality and validation directly or indirectly.

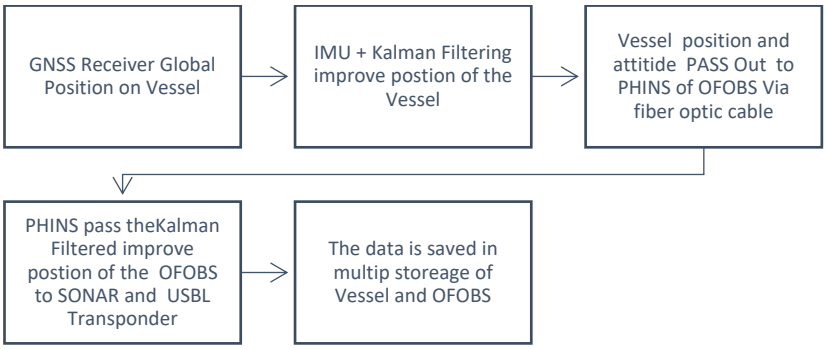

Figure 6-2: Navigation data flow from Vessel to OFOBS and back

The outputs of the navigation sensors vary in formats and logged places. The iXBlue HYDRINS unit on the ship passes the improved Kalman filtered position and attitude of the vessel to the subsea unit of the OFOBS via a fiber cable to the PHINS sensor.

The output of the PHINS is a navigation solution including geographic position, depth, heave as well as attitude and speed. The motion data comes from the internal 3D fiber optic gyroscopes and accelerometers, in addition to the external pressure sensor installed on the OFOBS frame. The embedded Kalman filter of the PHINS processed all the inputs in order to provide real-time positioning for the bathymetric systems which are also stored for post processing and evaluation.

The USBL-Box log stores a raw string of subsea transponder positions with the NMEA standard in ASCII format with a depth-dependent setting of a 5 to 8 second interval. The position provided by PHINS is three times more accurate than the USBL position (iXBlue (Ed.), 2011; iXBlue (Ed.), 2014). In addition for accurate sensor synchronization, the PHINS is time synchronized with the ships GNSS based timeserver and creates an OFOBS internal time and pulse per second signal (Purser et al., 2018).

Raw Imagery Data

During the OFOBS dive two camera sets were in operation, a video camera (*Sony FCB-H11*) and a stills camera (*Canon EOS 5D Mark III* + 24 mm fixed lens). The video camera was streaming and recorded constantly during the whole dive via a *RONIN HD-SDI system*. The video camera is meant for online observations during the dive by the operator and scientists, and the idea of adding the video frames came after the expedition in order to cover the still images gaps within the photogrammetric reconstruction step. The recorded videos are in Full HD resolution (1920 x 1080 pixels) with a rate of 25 fps and the extracted frames are 1-4 fps, depends on the

OFOBS flight height (FH) and speed. It was considered that the extracted frame has at least 60% overlap with each other and the stills images. For the area where the OFOBS FH was less than 3m and the towing speed were more than 0.5 knots the extracted frame was 4 fps while in case of low towing speed with bigger than 3-meter FH the extracted frame rate of 1 fps was sufficient.

The stills camera, which was meant for recording the seafloor, was operated within the iSiTEC OFOBS software package. The camera sensor combined with fixed lens provided a high-quality image of 22.3 megapixels (5760 x 3840 pixels). The controlling system supported two shooting methods; an automatic trigger was adjusted for 20 seconds intervals while manually shooting was possible by the operator.

The distribution of the frames and still images are not balances in the numbers and quality. Just 5 % of the still images among the extracted frames, is decreasing the quality of the point cloud and subsequently the orthophoto mosaic and DEM. This complexity is already have made the outputs data as multi resolution. In addition, the flight height of the OFOBS is changing dramatically from 1.2 meter to bigger that 8 meter, makes the resolution of the relevant data more complex which could be observed in the bathymetry data and 3D Reconstructed Model

In addition, the still images area timestamped by the vessel GNSS timeserver in UTC via Posidonia USBL, and well fitted with the metadata file containing all available camera parameters.

The data provided by the both imagery systems are the main dataset for the 3D Reconstructed Model.

Raw Sonar Data

Among the three-sonar system installed on OFOBS, the forward-looking Sonar (*BlueView M900-130*) was employed as an acoustic camera to assist in avoiding collisions with upcoming rocks, thus the data is not described here however the data has its own capacity and potential. The sound velocity probe (AML Micro-X 6000 SV-Xchange) was measuring the return time of the transmitted pulse in certain intervals during the OFOBS dives, and the result was used for real-time phase correction on the *EdgeTech 2205* multiphase echo-sounder (MPES) (Dreutter, 2017).

The *EdgeTech 2205* MPES has its own JSF file to store all the acquired data. The *EdgeTech Discover Bathymetric* software stores the high frequency (HF) and low frequency (LF) side scan data with attitude and position in the same file in addition to the binned bathymetry solution. The raw data file could be replayed in the post processing step with different parameters for bathymetry equiangular/equidistant, binning and range filtering. The side scan sonar data of PS101 is limited to 100m for LF and 50m for HF.

6.3.2 Enriched Raw Data

As mentioned before there is a large gap between the still images, which have a very good quality, and the metadata in comparison to the video frames which have relatively low quality but flexible coverage in overlap where the user could increase or decrees the amount of the overlap by changing the frame extraction rate. (Figure 6-3)

The process of the 3D reconstruction was carried out in the *Agisoft PhotoScan (*Agisoft (Ed.), 2016*)* (version 1.2). The Software is supports several image formats, but it is not able to import the video files directly, therefore the video frames are extracted in the rate of 1-4 fps. Then with the aid of provided Python scripts, the timestamp of the still images and INS navigation/ attitude data synchronises and are interpolated with respect to the lever arms. At the end the calculated values are assigned to the extracted video frames with a new name. By this sequence of the scripts the raw video frames have been enriched by virtual Interpolated metadata and then the enriched data sets are ready for the 3D reconstruction step. More detail of the preparation process are explained in Dreutter (2017).

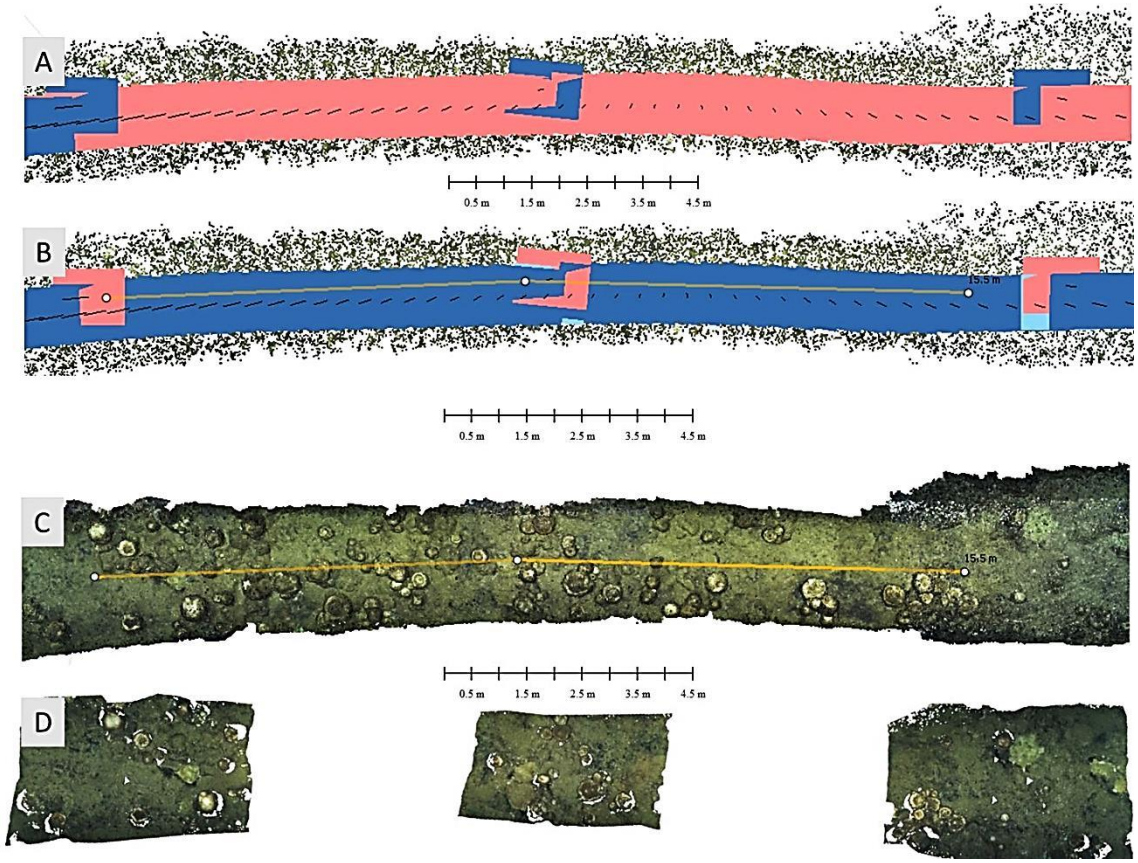

Figure 6-3: The Comparison coverage and gaps of the Still Image and Extracted video frames. (A, B) The image alignment step in *Agisoft PhotoScan*, (A) The Red areas are the extracted video frame and in (B) the three red areas are the Still images. (C) orthophoto mosaic of the same area (D) the individual orthophoto of Still images with corrected coordinated and the relevant gap in-between.

6.3.3 The 3D Reconstructed Model

In the third step the “Enriched raw data” is used to construct a digital georeferenced 3D model. Accordingly, in the immediate stage of the process, the “Constructed 3D Model” using Structure from Motion (SfM) technique is the main material and the basis for “Feature Detection” and secondary outputs and side products.

The main outputs used for this thesis are dense point clouds, orthophoto mosaics and DEMs and camera positions. In the early stage of the project the camera positions was applied to sonar data as a corrected track line of OFOBS in order to adjust the sonar position which normally gets position from USBL but had several disconnections due to technical problems (Dreutter, 2017). However, in this paper the camera positions considered the flight height in order to analysis the quality of point cloud (dense and noise) as well as the DEM and orthophoto mosaic characteristic.

6.3.4 Outputs of the SfM

Several other outputs are based on the reconstructed 3D Model, which inherits the quality of the 3D model. These secondary datasets are listed as follow:

1) Dense cloud, 2) DEM, 3) Mesh, 4) Individual orthophotos, 5) Orthophoto mosaic,

6) Camera positions as a corrected track line of OFOBS, 7) Point cloud

The process and the property of these outputs are described in the relevant chapter.

6.3.5 Classified Point Cloud of SfM

The raw dense cloud is one of the products of SfM and has some embedded noise. The levels of the noise have several dependencies which are described in the process and result chapters. The prepared dense cloud for feature detection is mentioned as point cloud (Figure 7-2 B), and it is categorized in 4 main classes as outputs of the point cloud classification:

1) Detected general noise, 2) Digital Terrain Model (DTM points), 3) Sponges crowns, 4) Ultra-Noisy area

6.3.6 Detected Sponges and Wet Biomass

Detected sponges and wet biomasses are the two products of the point cloud classification, and analysis which could be employed for further processing and geospatial data mining and knowledge discovery. For example, the detected sponges are used for feature analysis of morphotypes recognition and classification.

The wet biomass calculation is also the primary material for total biomass and dry biomass calculation which are not in the scope of this thesis.

6.4 Sponges Morphotypes Diversity in the Study Area

The OFOBS footage shows a variety of shapes of the similar morphotypes with different geometry and also some of the complexity with regards to sponges collision of the same type or other members of habitat community. Therefore, a local catalog is provided from the videos and still images in order to prepare an unofficial catalog of the sponge's geometry-morphotypes in the region, which are the essential key for data interpretation, feature detection and algorithm training. These two catalogs are "sponges regional catalog for geometry-morphotypes" shortened as "geom-morphotypes" illustrated in Appendix F, and some of the "complex situation for sponge detention" represented in Appendix G.

6.5 Navigation Corrected Sonar Data

The corrected camera positions aligned in the first step of the SfM process (Figure 7-2 A), are used as corrected track line of OFOBS. This new track line was applied to the SSS dataset and bathymetry grids then the corrected data used for feature detection. The corrected bathometry employed for Roughness estimation method in sub-chapter 7.2.3 and the classification of the SSS data is described in 7.5.

7 Data Processing

The following chapter describes the implemented methods for the sample area in five sub-chapters. The first sub-chapter introduces the 3D model reconstruction and then it follows a description of point cloud classification. The third sub-chapter focuses on sponge detection with a program called *Spongdia*. The fourth sub-chapter describes the volume calculation for biomass estimation. The fifth sub-chapters provide a brief note about the feature detection on the side scan Sonar by raster classification.

The following graph gives an overview of the processing workflow. The sub-processes highlighted by an orange color box are the main focus of this section and will be explained in detail. However, the sections in the blue box show the fundamental processes section for the main part therefore briefly described.

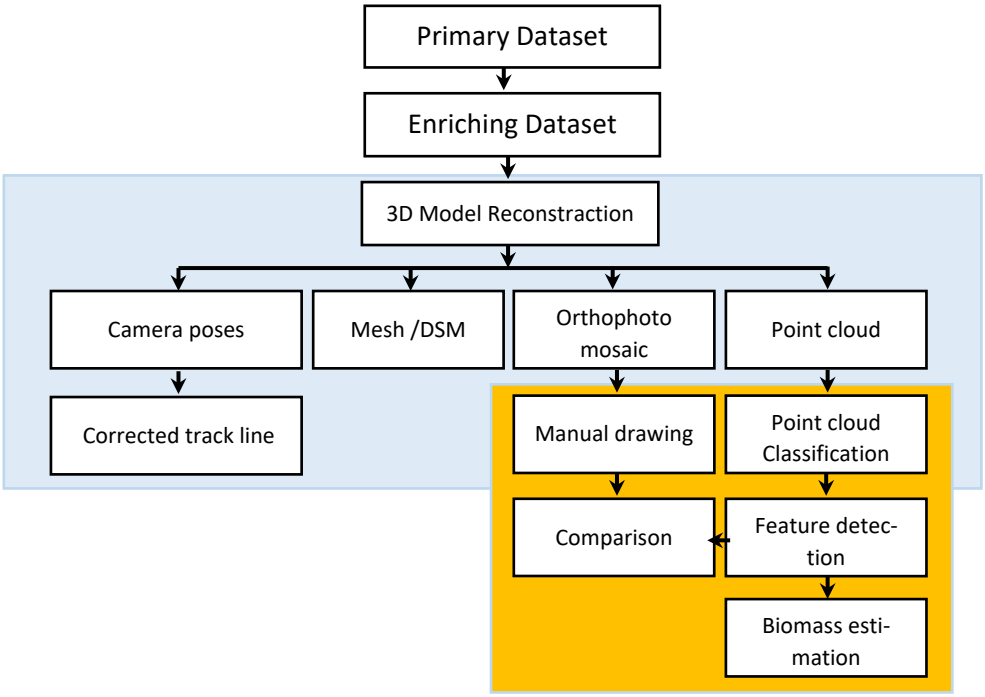

Figure 7-1: Overview of the data processing workflow

Agisoft PhotoScan was utilized to align video frames and still images in order to get a continuous 3D model of partial dive tracks of the OFOBS. The SfM process was used to improve the existing navigation data and to achieve higher accuracy camera poses. Those workflows are part of the process done in this project, however the workflows were developed in an earlier stage of the project and are explained in detail in Dreutter (2017).

7.1 The 3D Model Reconstruction

The output of the enriched data described in 6.3.2 is imported to the *Agisoft*. The work flow of the 3D model reconstruction is based on the *Agisoft* program with some concern about camera positions and orientations. The figure 7-2 represents the workflow and the corresponding outputs and applications.

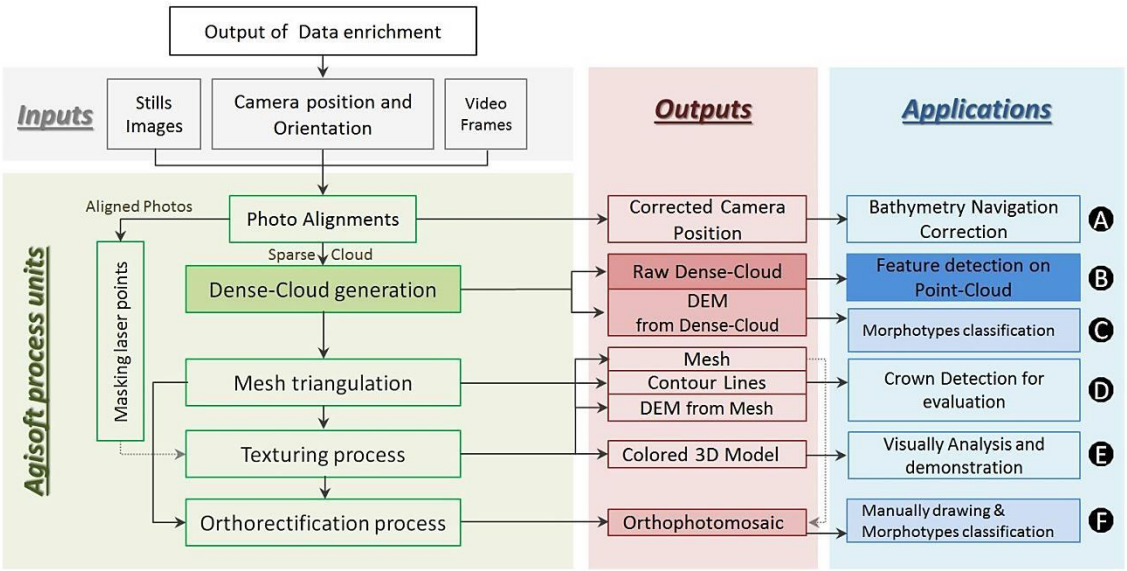

Figure 7-2: The 3D model reconstruction workflow and relevant outputs and applications

The 3D Model reconstruction is the fundamental step for producing the other intermediate material of the feature detection and segmentation such as point cloud, DEM and orthophoto mosaic. The imagery enriched materials along with the camera position and orientation are imported to *Airsoft*. Then the images are aligned with each other by using the SfM method described in Sub-chapter 2.5. The first output of the process is the corrected camera position which is applied for bathymetry navigation correction (Figure 7-2 A). Also, the Sparse-Cloud produced within photo alignments is used for dense cloud generation, which is called a raw dense cloud: the main material for feature detection (Figure 7-2 B). The other product of the dense cloud is DEM that is applied as a raster layer for geom-morphotypes classification (Figure 7-2 C) along with orthophoto mosaic (Figure 7-2 F) explained in sub-chapter 7.6. The mesh is the result of the dense cloud triangulation which is also a substance for contour line interpolation, orthorectification and 3D model generation. The other matter that takes part in the orthorectification process is the delighted texture fused by an ambient occlusion process and cleaned from the triple laser spots by a masking method.

The orthophoto mosaics and the colored 3D models are used for manual digitization and visual analysis (Figure 7-2 F and E). The generated contour lines are used in crown detection for

evaluation purposes (Figure 7-2 D). The characteristics of these outputs are described in sub-chapter 8.2.

7.2 Point Cloud Classification

The objective in using this process unit is to separate any points shaping non-bio material from the points shaping bio material, including sponges and sponge spicules accumulation. These two classes will be used for sponge detection and biomass estimation.

Visual evidence from camera footage shows a complex environment, where it is hard to define specific boundaries between bio and non-bio materials. Within the sample area, the sponges have a very similar color to the background seafloor. This is because the seabed is mostly covered with the sponge spicules mats that partly intermixed with sediments from the seafloor. Thus, it is almost impossible to detect and separate the sponges from the background using the color variable parameter. Therefore, an alternative separator factor should be defined in order to separate sponges from the seabed, though an uncertainty in identification success is to be expected.

Figure 7-3: Stills image of the OFOBS camera, showing the intermixed layer of spicules mats and sediments. At the top of the picture there is a Geodia sponge partly covered by a spicules blanket.

The data used for this part of the process is from the raw dense cloud (Figure 7-2 B) which is a colored point cloud. As the color property is not involved in this process, henceforth it will be mention as point cloud.

There are a few geospatial characteristics which could be defined as the separations rule within the point cloud of the sample area, such as regional slope detected by angle or roughness.

In order to define the reginal angle as the first separator rules, a recently developed method was employed, namely the Cloth Simulation Filter (CSF) algorithm applied for DTM point cloud classification. The algorithm is designed to extract ground points in discrete return LiDAR point clouds, but later developed and implemented for photogrammetry and remote sensing applications as well (Zhang et al., 2016).

The CSF algorithm is applied via *Agisoft* for ground point classification in as the first separation method, except for the ultra-noisy part of the sample area, where the result was not satisfactory and thus the backup method was applied. The Roughness classification algorithm was also applied via *CloudCompare (*GPL-software (Ed.), 2017*)* over the extracted unclassified section.

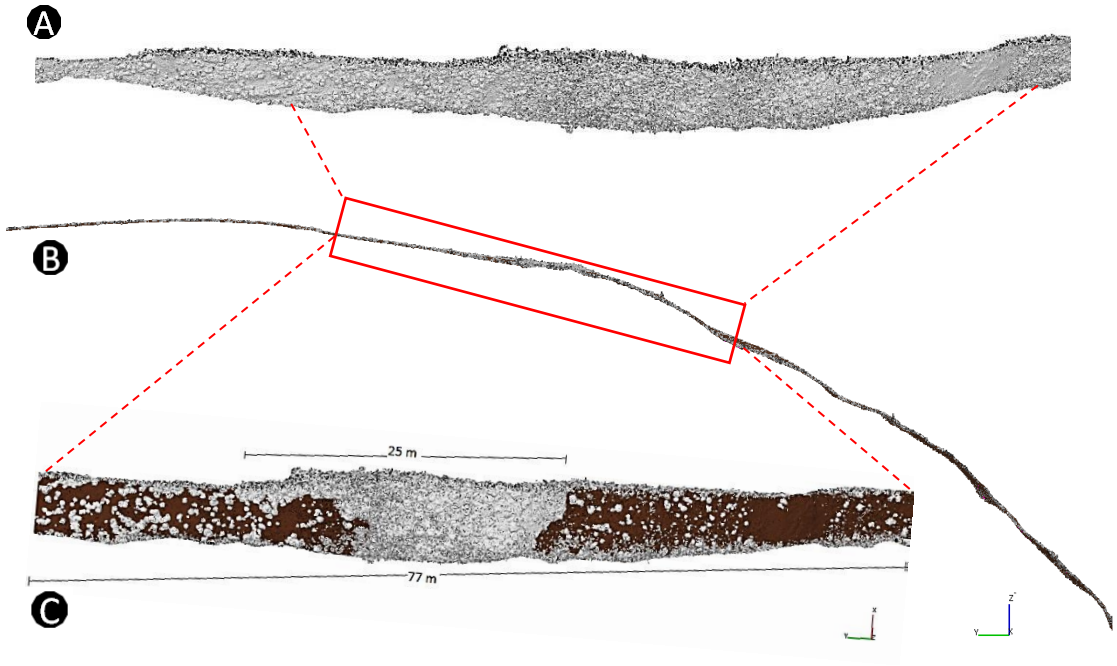

Figure 7-4: (A) top view of the unclassified point cloud (B) The side view of classified point cloud in the slope area (C) The 25 m of the ultra-noisy area after CSF classification. The gray areas are the unclassified points and the brown areas are the Classified DTM points.

7.2.1 Cloth Simulation Filter (CSF) Classification

In order to start the point cloud classification in *Agisoft*, first the whole project should commence with image alignments followed by dense cloud generation, since it is not possible to import the individual point cloud from other sources to the current employed version (*Agisoft PhotoScan Professional, version 1.2.6*). The dedicated *Agisoft* project contains about 2000 pho-

tos of different sources and qualities. The aligned project was too big to handle in one solid session thus the project was divided into three chunks.

Since the aim of this section is to separate non-ground points from ground points, a deeper look into point cloud classification algorithms is worth mentioning.

Agisoft PhotoScan provides two methods of point cloud classification. The first method is the manual selection of points to be placed in a certain class from the standard list known for LIDAR data. There are also some selection tools and filters provided such as "Select points by color and masks", however it does not help greatly with the given sample area dataset, which has a low color contrast, regardless, manual classification is not the intention of this thesis, even though the tools are of considerable use for slight manipulation over outlier noise.

The first and main method is automatic separation of points into ground points and non-ground points. *Agisoft* benefits from the CSF algorithm for automatic classification in two steps. The initial step is dividing the dense cloud into cells of a certain size where within each cell, the lowest point is detected. Triangulation of these points provides the first approximation of the terrain model. Then in the second step, a new point is added to the ground class. This new point has to pass two conditions: it lies within a certain distance from the terrain model and that the angle between the terrain model and the line to connect this new point with a point from a ground class is less than a certain angle. The second step is repeated while there are still points to be checked.

There are three parameters controlling the automatic ground point classification procedure as follows:

1) Max angle (deg):

The angle is one of the conditions to be checked while testing whether a point represents the seafloor. This parameter determines the assumption for the maximum slope of the ground within the scene. It sets a limitation for an angle between terrain model and the line that connects the point in question with a point from the ground class.

2) Max distance (m):

This parameter determines the assumption for the maximum variation of the ground elevation over a given time or distance. It is one of the conditions to be checked while testing a point as a ground point. It sets a limitation on the distance between the point in question and the terrain model.

3) Cell size (m):

The cell size is determined by the size of the cells that the point cloud will be divided into as a preparatory step in the ground point's classification procedure. Cell size should be indicated with respect to the size of the largest area within the scene that does not contain any ground points.

The Agisoft forum also suggested some variables for these parameters for urban, forest and topography landscapes which did not provide a satisfactory result for the given micro-

bathymetry dataset, thus a new set of the parameters was tested on the sample area in order to find out the most suitable variables for the given dataset.

The segmentation of the point clouds is a time consuming process. 19 different variables are applied to determine the best fit parameter sets for the DTM segmentation in the given sample area. The tested variables are listed in (Table: 7-1.)

Parameters of the dense cloud classification			
Parameter sets	Max angle (deg)	Max distance(M)	Cell size (m)
1st	15	0.1	25
2nd	15	0.1	5
3rd	15	0.2	5
4th	25	0.1	5
5th	15	0.1	50
6th	10	0.1	50
7th	5	0.1	50
8th	5	0.1	25
9th	5	0.1	10
10th	7	0.1	10
11th	10	0.07	10
12th	10	0.07	25
13th	5	0.07	10
14th	5	0.06	5
15th	5	0.05	10
16th	5	0.05	5
17th	5	0.05	2
18th	7	0.05	2
19th	7	0.05	1

Table 7-1: Parameter sets tested for dense cloud classification in *Agisoft*. The highlighted row is showing the convenient parameters for the sample area.

7.2.2 Roughness Estimation for Imagery Dataset

In the mid slope of the sample area there is a 25-meter boundary, where the Agisoft CSF algorithm result was not satisfactory, as a matter of the noise and therefore the low quality of the point cloud.

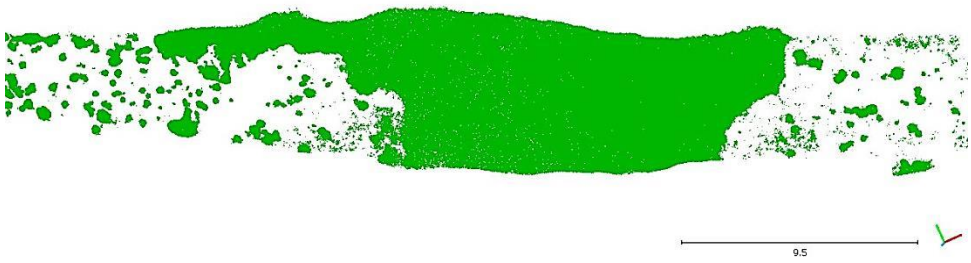

Figure 7-5: Ultra-noisy area in the slope area.

An alternative algorithm for classification is the Roughness estimation. This method was applied to the ultra-noisy area for DTM classification via *CloudCompare tools.*

The surface roughness prediction model is based on a support vector machine and the logic of this method is to computes individual 'roughness' values per point with regard to its neighbor points. For each point, the 'roughness' value is equal to the distance between this point and the best fitting plane computed from its nearest neighbors. In cases where there are not sufficient numbers of neighbors to compute, for example at the edges of the point cloud boundary, the roughness cannot be found. In that situation a Least squares plane (LS plane) with invalid scalar values is used, where the adjacent neighbors are less than three (GPL-software (Ed.), 2017).

The algorithm steps are described as follows: (1) First the tool extracts neighbors around each point inside a sphere (kernel = sphere radius). (2) Then the tool fits a plane to the neighbors. At least 3 neighbors are needed, but more points are recommended. (3) Afterwards, the tool computes the distance between the central point and the LS plane. The 'roughness' is then simply the deviation from the average local surface.

To run the algorithm there is one variable which needs to be defined. *CloudCompare* asks for the 'kernel size' which is the radius of a sphere centered on each point. The software supporting technician describes the right kernel value based only on the size of the features needs to be identified. Thus, for the given data set three different values were applied in order to get the best possible output values by the experiment: The kernel size of 0.029 m, which is the default value of the exported dense cloud, the kernel size of 1 m, which is the approximate size of biggest sponges in the sample area, and the 0.35 m, which are assumed to be the approximate size of the most sponges in the sample area. The result of this comparison is illustrated in the relevant sub-chapter 8.3.2.

7.2.3 Roughness estimation on Bathymetry Grid

The same method of Roughness estimation applies for bathymetry data. First the bathymetry grid, which unfortunately had a navigation problem, was corrected by fixing the camera position (Figure 7-3 A) as it is described in *Dreutter (2017)*. Then the point cloud of the corrected bathymetry grid was exported as the new point cloud and the similar process of Roughness estimation was applied to the data via *CloudCompare tools*. The results are illustrated in subchapter 8.4.

7.3 Sponge Detection by *Spongdia*

"*Spongdia*" is the name of a python based program, which was developed for "Tree-Detection" in forest inventory from point clouds in cooperation with the author by a Geomatics Student of the HafenCity University Hamburg (HCU) (Hosseinie Abrischimie, 2017). During the main program developing phase sponge detection was considered along with Tree-Detection, but later the new version derived from the main script was further adapted for sponge detection, specifically Geodia sponges from any source of point cloud, (including Laser scanner and photogrammetry).

In this sub-chapter, the methods and workflow of the program *Spongdia* are described in detail including point cloud filtering, DTM generation, sponge Crowns segmentation, sponges' peaks detection and sponges' height calculation. These functions are standalone processes by *Spongdia* benefits from python including python packages and libraries.

Spongdia is mainly a filtering and calculation tool equipped with geostatistical algorithms and also some information windows for presenting statistical and minor graphic display (Figure 7-6, E and F). For the point cloud demonstration the program is not providing a graphical environment, but the outputs are platform independent, therefore the results could be shown in any point cloud supporting program.

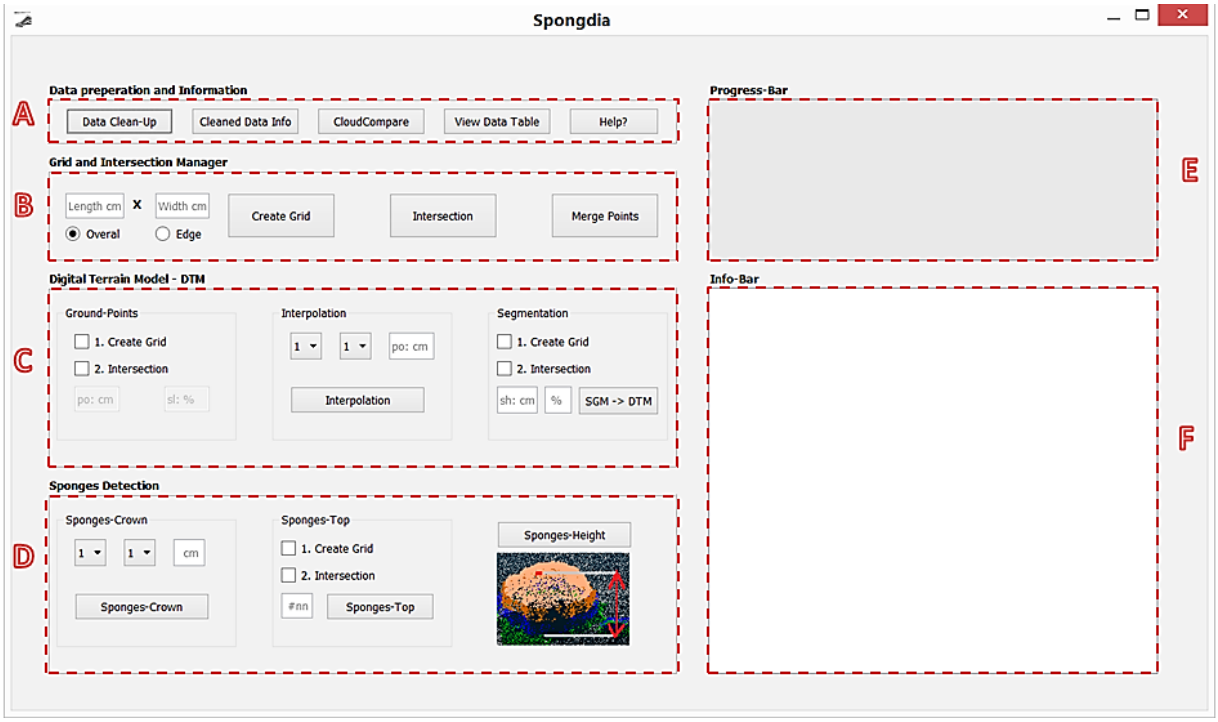

Figure 7-6: Spongdia environment and functions. The Spongdia GUI is designed in six main parts (A-F) as it shown in the picture. (A)Data Preparation and Information, (B) Grid and Intersection Manager, (C) DTM extraction, (D) sponge Detection, (E) Progress-Bar, (F) Info-Bar.

The recommended demonstration environment for results and outputs is "*CloudCompare*" a GNU General Public License Software. The whole output structures are kept simple and follow the well-known standard formats such as "Esri SHP" files and also "xyz" as well as "las" formats which are text files in ASCII format.

Although the program is developed with the open source python platform, it also benefits from other fundamental packages which should mention in regard to copyright law. The following table (Table 7-2) is listing the packages and libraries which *Spongdia* benefits from.

The aim of the software is to detect the sponges in the study area from the point cloud by separating the Crown and calculating the sponges' height.

Python Package and Library	Main functions
NumPy	Scientific computing, N-dimensional array object, Linear algebra, Fourier transform, and random number
Pandas	structures and data analysis
Geopandas	spatial operations on geometric types
Scipy	Python-based ecosystem of open-source software for mathematics, science, and engineering. For "*Spongdia*" the following tools have been used: 1-scipy.spatial : nearest neighbors, distance functions library 2-scipy.interpolate: Interpolation tools
Shapely	A group of libraries for manipulation and analysis of geometric objects in the Cartesian plane. For "*Spongdia*" the "geometry" library is used
Math	It provides access to the mathematical functions defined by the C standard
Matplotlib	Python 2D plotting library in order to produces figures in a variety formats and interactive environments. For "*Spongdia*" the library "matplotlib.pyplot" is employed
time	Time library is providing processing time calculation function
Shapefile	The Python Shapefile Library (pyshp) is a purely python package for reading and writing ESRI Shapefiles
Sklearn.neighbors	Main package for Machine Learning in python by Data mining and Data analysis provides functionality for classification, regression, clustering, unsupervised and supervised neighbors-based learning methods

Table 7-2: List of fundamental packages and libraries that Spongdia benefits from.

7.3.1 *Spongdia* Workflow

There are six main steps in the sponge detection workflow which are shown in the following diagram (Figure 7-7) and each step output could be described as an individual product. More details for each step will be described in the upcoming relevant sub-chapters. During each step of the program, a fuzzy logic approach is attempted.

Figure 7-7: Spongdia workflow

The very first step is to prepare the given point cloud for the main processing steps by reducing the size of the data by deleting the unnecessary information. The next step is deleting major noise in the point cloud and then several classes of point will be assigned to different groups within the points. The first group of points represent the seabed allocated by the Digital Terrain Model (DTM) class. Then the group of points which are shaping the sponges dome, are assigned as the crown class and the peaks within the extracted pieces out of each sponge crown are used for the height calculation of sponges.

The entire process has been applied to the sample area extracted from OFOBS dive PS101/169-1 to the Karasik seamount and the results will be discussed in the relevant chapter. For more detailed demonstration and description of the methodology steps, a sub-section of the sample area was chosen and illustrated in Figure 7-8.

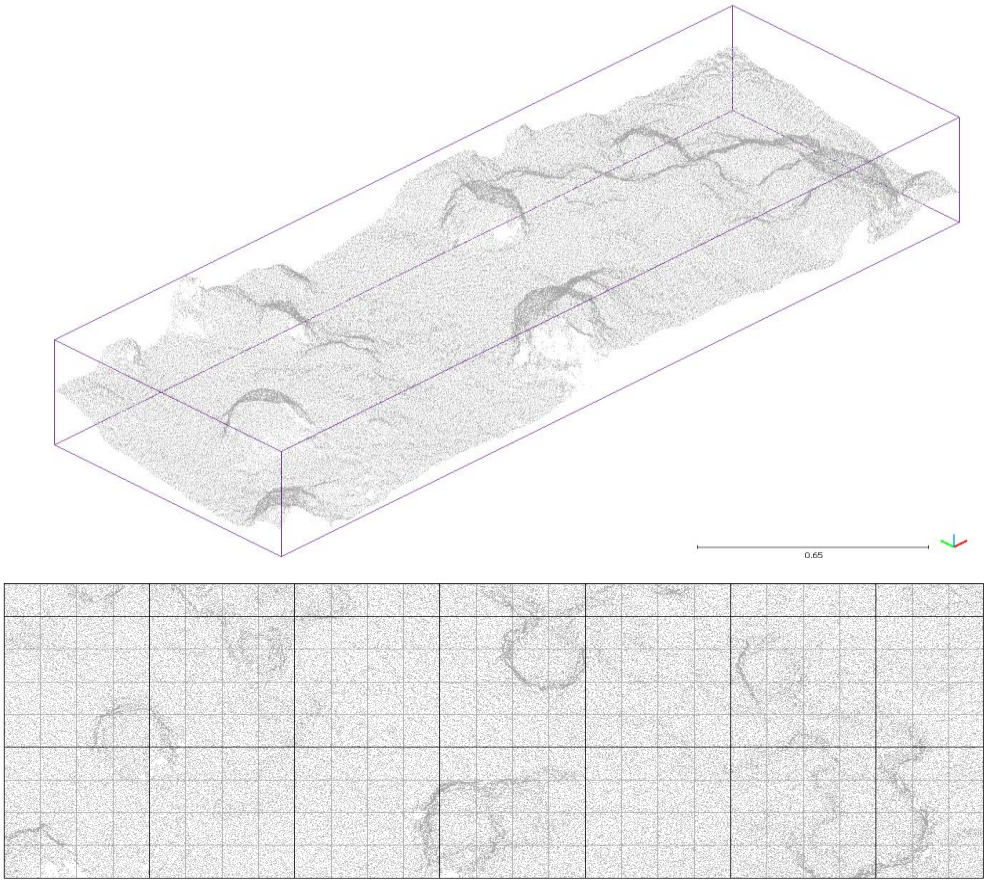

Figure 7-8: Top and Isometric view of the sub-section of the sample area.

7.3.2 Grid Generation

The grids are a necessary aid, as they are applied in several steps such as DTM and crown detection as well as the sponge peaks calculation. The grid generation is based on information about the spatial extent of the area by specifying cell length and width.

To do so, a Minimum-Area-Rectangle (MAR) (Freeman & Shapira, 1975) for given points is calculated to find out the best fit for the known coordinates of the rectangular frame points, and then the following formula (Figure 7-9) is used for grid generation based on the given variables as grid width and length.

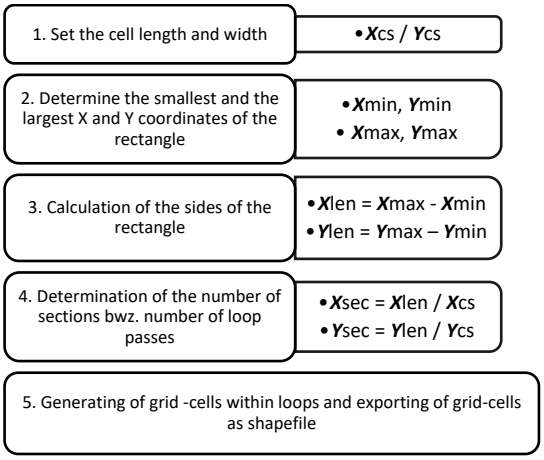

Figure 7-9: Workflow of the grid calculation

The required grid cell size should be considered individually in each step of sponge detection as it varies in dimension for each purpose.

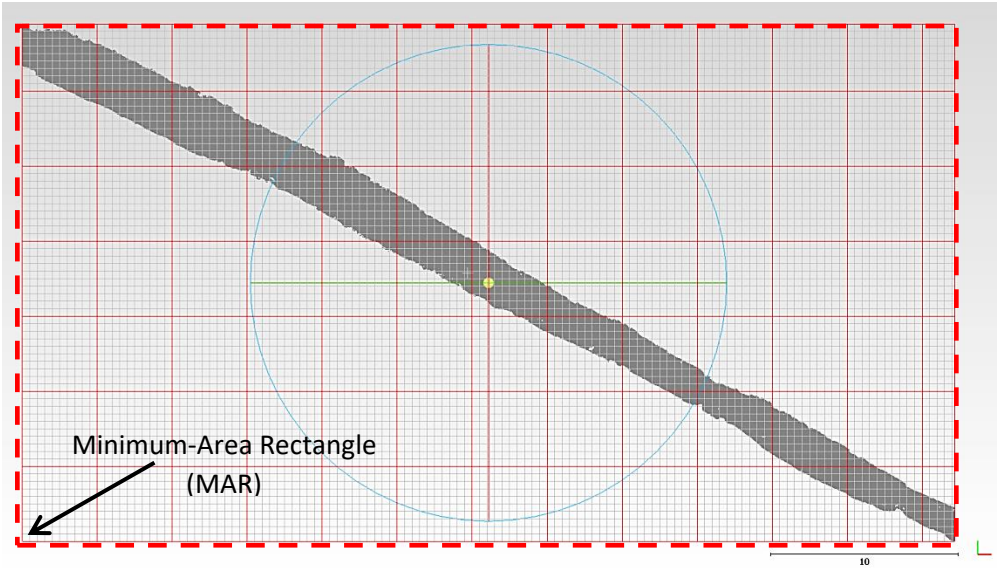

Figure 7-10: Gridding by Minimum-Area Rectangle over Chunk 1 of the sample area.

To generate the DTM, the whole point cloud should overlay with the grid, with respect to the geometry and the size of the features which are needed to be identified. Hence the size of the grid should be chosen so that each cell contains at least one bottom point of the DTM. For Sponge detection in the sample area, it seems that the diameters of the sponges do not exceed 90 cm. Therefore, for DTM detection, the grid size of 1 and 3 meters was applied. While the grid size for peak detection was set as big as 5 to 10 cm for crown detection.

7.3.3 Data Preparation

The very first step in processing the point cloud in *Spongdia* is to define the data format with the data size and processing time. Input and output are then defined, as the script should be able to be read and processed in the common formats of point clouds. For memory allocation, the size of the data must be reduced so that the file contains only substantial information for performing the given tasks without loss of required accuracy.

The following table (Table 7-3) showing the uncleaned data which is a sample dense cloud output of SfM process, exported from *Photo scan Agisoft:*

X	*Y*	*Z*	N_x	N_y	N_z	*R*	*G*	*B*
2313685.54479980	1831673.71720123	-771.18572998	0.246330	-0.129030	0.960558	57	57	57
2313685.53829956	1831673.67549896	-771.18359375	-0.112319	-0.034474	0.993074	55	55	55
2313685.567802430	1831673.695396420	-771.18310547	0.166954	0.062756	0.983965	53	53	53
….								

Table 7-3: Sample area-1 dense cloud information before cleaning.

The exported dense cloud from SfM phase include XYZ coordinates and “per-point normal vectors associated to the vertex” ($N_x/N_y/N_z$) likewise “per-point colors” (RGB) values. It is possible to ignore this data while processing script but this information still makes the processing time longer therefore it is better to back up the main data and delete unnecessary information in a new copy. The following table (Table 7-3) shows the cleaned data which is simple standard xyz coordinate, output of the *Spongdia.*

X	*Y*	*Z*
2313685.5448	1831673.7172	-771.1857
2313685.5383	1831673.6755	-771.1836
2313685.5678	1831673.6954	-771.1832
….		

Table 7-4: Sample area-1 dense cloud after cleaning by *Spongdia*.

Although the original dense cloud and cleaned point cloud contain the same amount of points, they differ considerably in size and data contained. As is shown in the Table 7-5, usually there are three data types available in the raw dense cloud and there are three column data for each of them with different string length.

Data type	Column Per value	Number of Characters for Uncleaned Data	Number of Characters for Cleaned Data
Coordinate (XYZ)	3 column	≥ 47 Character	≥ 38 Character
Per-point color (RGB)	3 column	6 to 12 Character	0
Per-point normal (Nx,Ny,Nz)	3 column	~ 30 Character	0
Over all	9 column	~ 90 Character	~ 40Character
Comparison	_	100%	44%

Table 7-5: Comparisons of the content and character length in the cleaned and uncleaned data tables

The cleaning process has two parts, first deleting unnecessary data columns and second shortening down the digit decimals to the sufficient value by rounding up the value.

In the Sample area-1 the cleaned data file requires 283 MB in order to keep 3D coordinate of about 8 million points, while the uncleaned file is up to twice the size.

The Table 7-6 outlines the information and data size before and after cleaning it up in sample area-1. The XY coordinates are rounded to four decimal places and the Z value is rounded to five decimal places in advance, since accuracy in the range of submillimetre is not required and hundred micrometre resolutions cannot be achieved in our survey anyway.

Sample area-1	Uncleaned dense cloud	Cleaned up dense cloud
File capacity	573,766 KB (100%)	283,448 KB (49.4%)
X,Y precision	8 Digit Decimals each	4 Digit Decimals
Z precision	8 Digit Decimals	5 Digit Decimals
Per-point color	-	-
Per-point normal	6 Digit Decimals each	-

Table 7-6: Comparison of the cleaned and uncleaned data by file capacity and character length

7.3.4 General Noise Detection and Filtering

Image-based point clouds generated by 3D reconstruction techniques are often much noisier than those obtained using active techniques like laser scanning (Wolff et al., 2016). This noise can be exponentially higher for underwater images, where aquatics and suspended material traveling in the water column are captured more frequently in the cameras Field Of View (FOV).

Since this noise poses significant challenge at the feature detection stage, noise should be reduced significantly at the beginning and during the process.

The first step is to detect the noises and improve points in the given data so called “Raw dense cloud “which is the non-segmented point cloud of the SfM stage.

This noise is detected and filtered out in three steps, first by segmenting the Z value point cluster in each grid-cell and then assigning a weight scale to each point. Thus, the points which have a dramatically low weight compared to each scale value will be considered as noise potential.

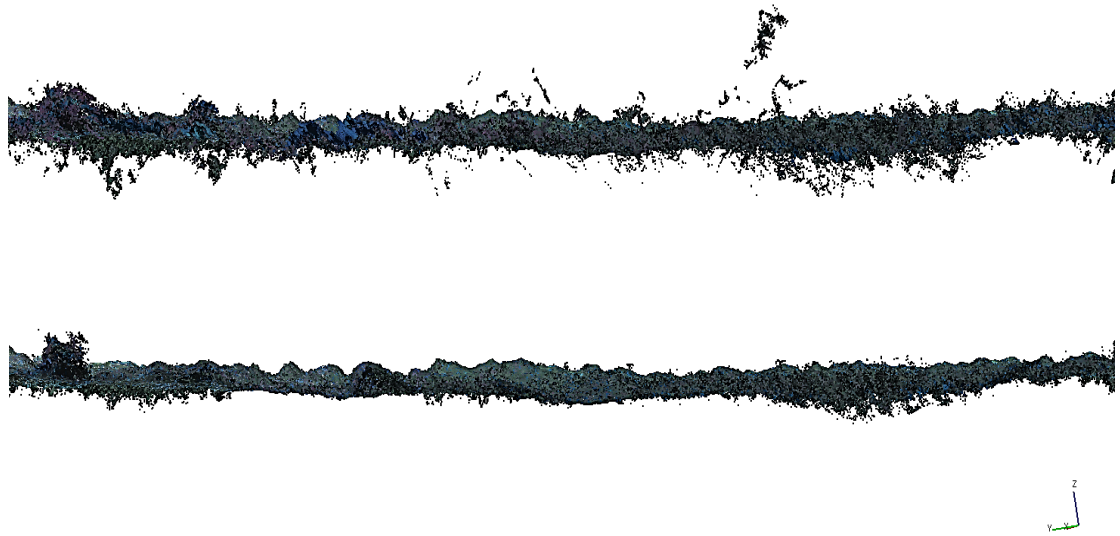

Figure 7-11: Side view of the raw dense cloud with noise in water column (top), and after the noise filtered (bottom).

This procedure will omit most of the noise via consideration of the Gaussian distribution of the Z value in each individual cell of the grid. In the current version of *Spongdia* non-normal distribution filtering is not included, so these kinds of noises cannot be addressed by the current methodology.

A more complete description of noise filtering will be discussed in the DTM generation subsection as the principles of the filtering are similar.

7.3.5 DTM Detection

It is essential to mention that the term Digital Terrain Model (DTM) in micro-bathymetry should be considered slightly differently compare to the shipborne bathymetry.

In usual bathymetry, sub-meter organisms, such as sponges and starfish, settled in or on the seafloor are treated as part of the terrain, thus they are part of the DTM, while in micro-bathymetry these benthic megafaunas should be drawn out from the other points so they can be identified and their densities across an area and in relation to terrain variables are considered alongside scientific questions.

In the next step of the sponge detection workflow, the main goal is to find and filter those points which have the most probability to be potentially useful in generating the seafloor terrain model. Therefore, in this section a fuzzy logic approach is implemented in order to define a class of the points with different credit. Therefore, the DTM detections process has several sub-steps and iteration.

The following picture (Figure 7-12) is representing the steps for DTM detection, by *Spongdia*.

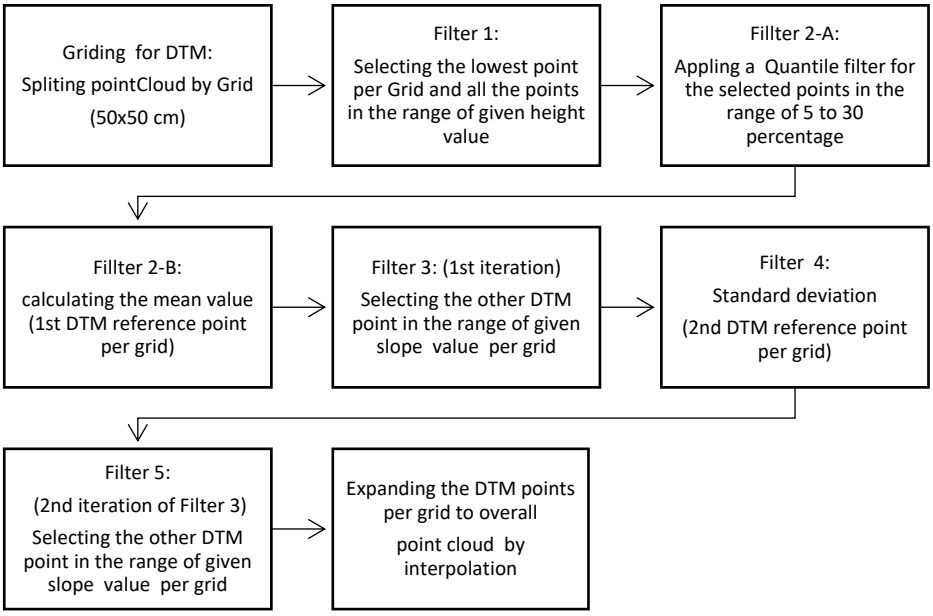

Figure 7-12: DTM detection workflows of the Spongdia.

As mentioned earlier, the point cloud should be free of radical noise. In the first sub-step the point cloud should be split up by the gridding method. There is a gridding tool within *Spongdia* for this purpose (Figure 7-6, B) and the grid cell size should be considered as their cells should be big enough to contain at least one low ground point and small enough to not be affected by the slope of the area.

The second sub-step is to find representative ground points within each grid cell. For this purpose, the algorithm selects the lowest point per Grid and all the points in the range of a given height (Filter 1). Then the mean value of all points in the range of 5% to 30% Quantile from the first filtering will be selected. This mean value is the first reference-point within each grid (Filter2 A and B). Based on the first reference-point all points with a given slope line to this point will be selected per grid (Filter 3).

A second reference-point is the result of standard deviation of these selected points applied (Filter 4). Then the filter 3 will run as the second iteration and grade the resulting points as ground points per grid-cell. In some situations, there are gaps between filtered points from grid-cells of the same neighbourhood.

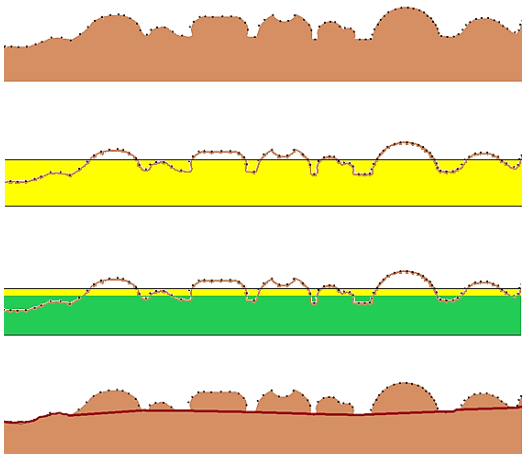

Figure 7-13: Schematic side view of DTM segmentation. The Yellow area is where Filter 2 searches and the Green area is the scope of Filter 3

This mostly occurs when a general inconsistent micro slope appears in the overall area. Regarding the geomorphological aspect, these anomalies are not matter of ground slope but mostly are dead sponge mats laying over the seafloor.

The last sub-step is to expand these filtered per-grid DTM points to overall DTM points, In order to generate seamless DTM points in overall point cloud, which is a matter of 2D interpolation.

This will be achieved when all the ground points determined in each of the grid-cells are interpolated and all points in the range of the given height above the interpolation area are graded as the DTM points for the area. The selected points are exported as a DTM class for non-sponge area. Those areas which are covered by sponges will remain as holes in the DTM point class.

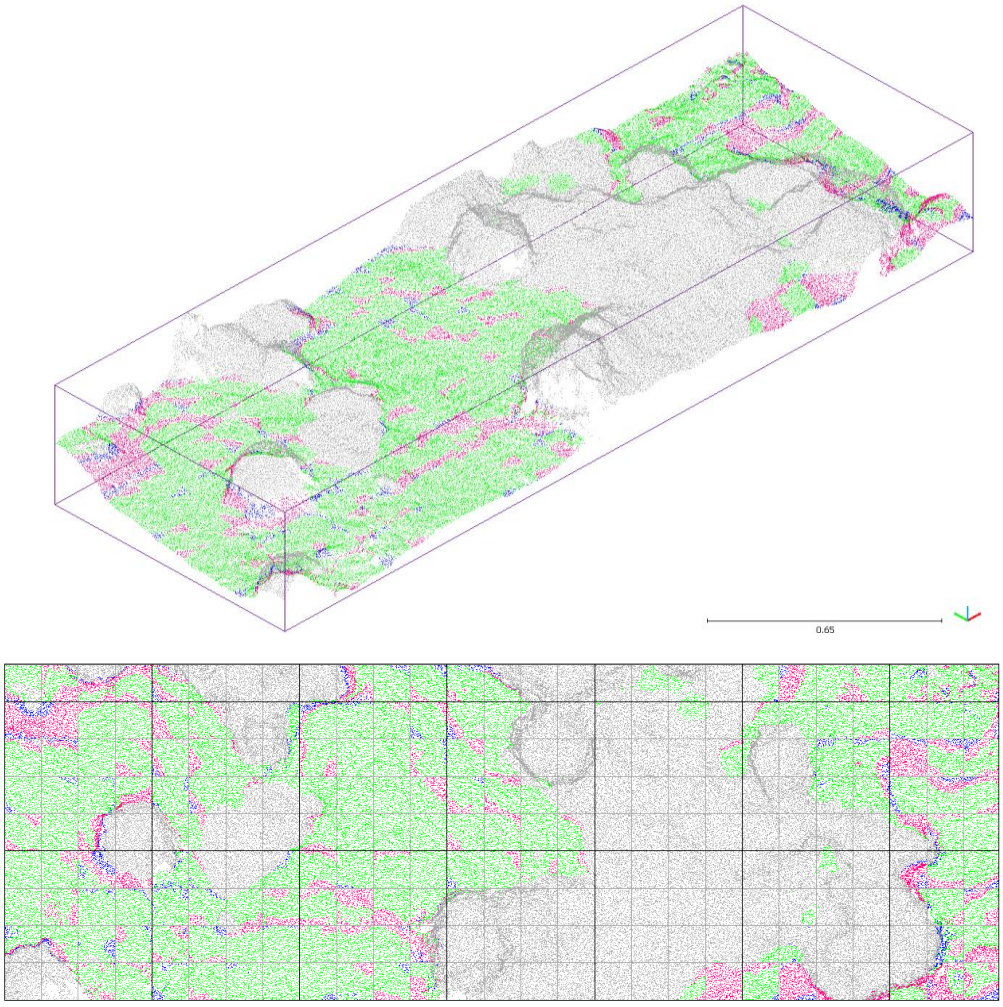

Figure 7-14: Overlay of three layers of the DTM points filtering; The top layer is the output of first iteration of the Filter-3 (Blue points), The middle layer is output of the Filter-5 (Red points) and the bottom layer is the output of the inter grid interpolation

7.3.6 Crown Detection

The most probable points which have the potential of being part of the sponge crown (top regions of sponges) are filtered as the sponge crown class, in five sub-steps.

First, the point which was in the previous processes filtered as DTM point will be enriched by interpolation and evaluate between the gaps of the sponge area.

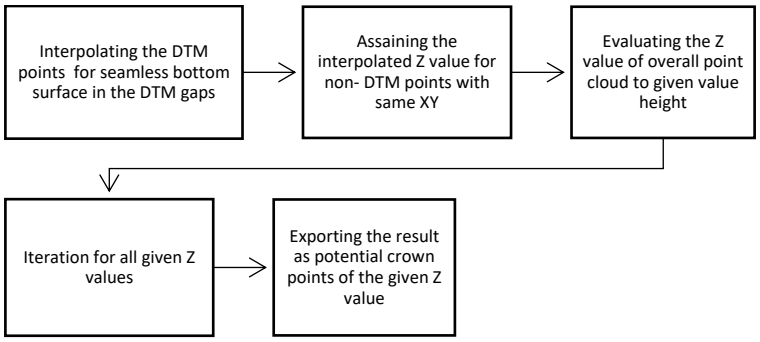

Figure 7-15: The crown detection workflow

This process will provide a virtual DTM point value for the bottom of sponges where there is a gap, in order to get a seamless DTM point cloud. This interpolation will be assigned as interpolated Z value to those points which are not part of the DTM. This interpolation will fill the gap area.

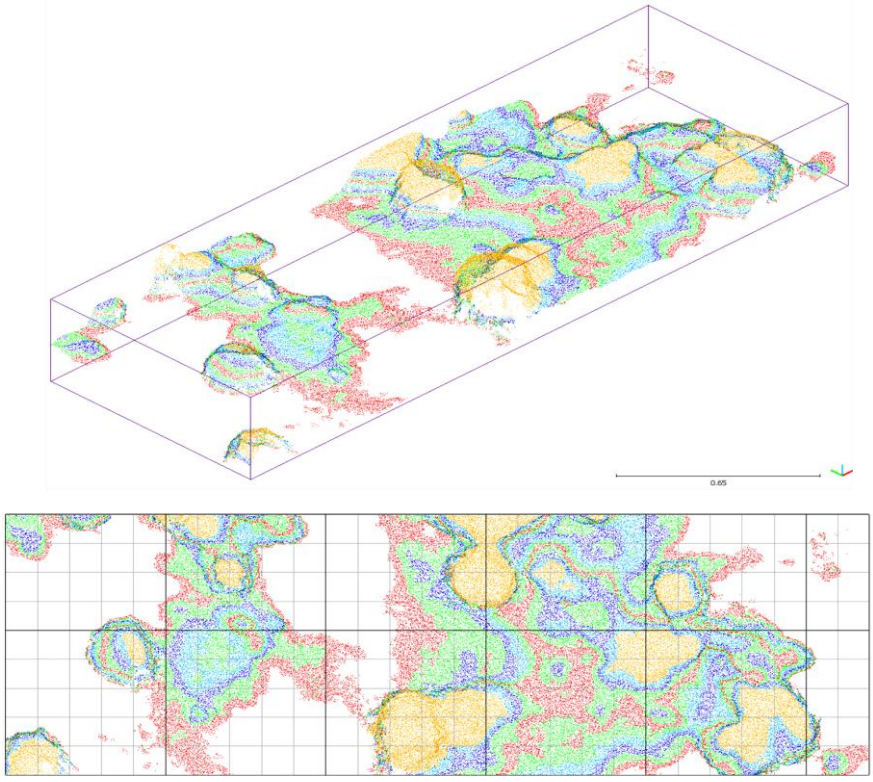

Figure 7-16: Segmentation over sponge's crown on Spongdia.

It is essential to mention that the detected crowns are not only the sponges but also area of sponges' spicules accumulation.

In order to get most probable sponges out of these first detected crowns, the segmentation process is designed in *Spongdia* GUI. The result of the non-segment of the crown is presented in the Figure 7-16 by a different color value; the highest layer is the most probable sponge crowns while the lowest layer is the less probable segment.

7.3.7 Peaks Detection

Like the previous steps there should be a grid network intersected to the relevant point cloud. The analysed point cloud in this sub-step is the crown points, intersecting with a 5x5 cm grid. Then the highest point per grid will filter out crown sparse points, which will provide the highest point within each grid-cell.

Then, regardless of the actual position of each of these sparse points, the height of the point is assigned to the relevant grid centroid. Next, the Nearest Neighbours (NN) algorithm (Altman, 1992) is used to search and compare the height of the assigned centroids in order to find the highest value. The algorithm will iterate until there is no highest centroid in the neighbourhood for each start point within the whole crown point cloud.

The next sub-step is to assign back, the original position (XY) value of the detected top centroid by the original point ID.

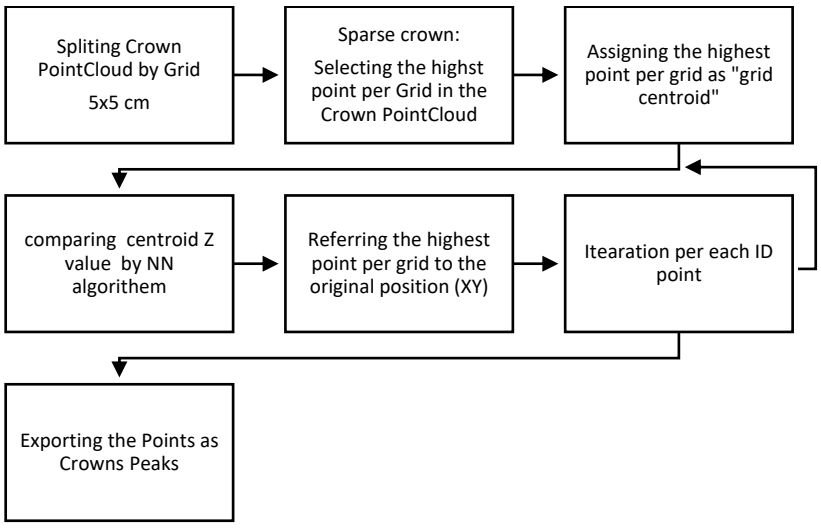

Figure 7-17: workflow of the peak detection in Spongdia.

The Nearest Neighbour algorithm is the searching method in pattern recognition which examines the distances between each point and the nearest point to it and compares the values for an arbitrary sample of points to a "Complete Spatial Randomness" (CSR) pattern (Altman, 1992).

The following schematic picture is illustrating the functionality of the Nearest Neighbour algorithm within 25 NN variables within the given point cloud.

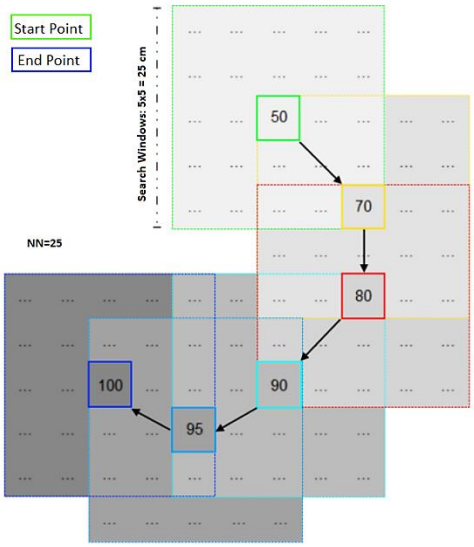

Figure 7-18: Schematic search of Nearest Neighbors algorithm in sponge peak detection for 25 neighborhood and 5 cm grid size (Hosseinie Abrischimie, 2017).

During the peak detection in the sample area the NN algorithm is applied with several variables as 9, 13, 25 and 45. The outputs are illustrated in the sub-chapter (8.4)

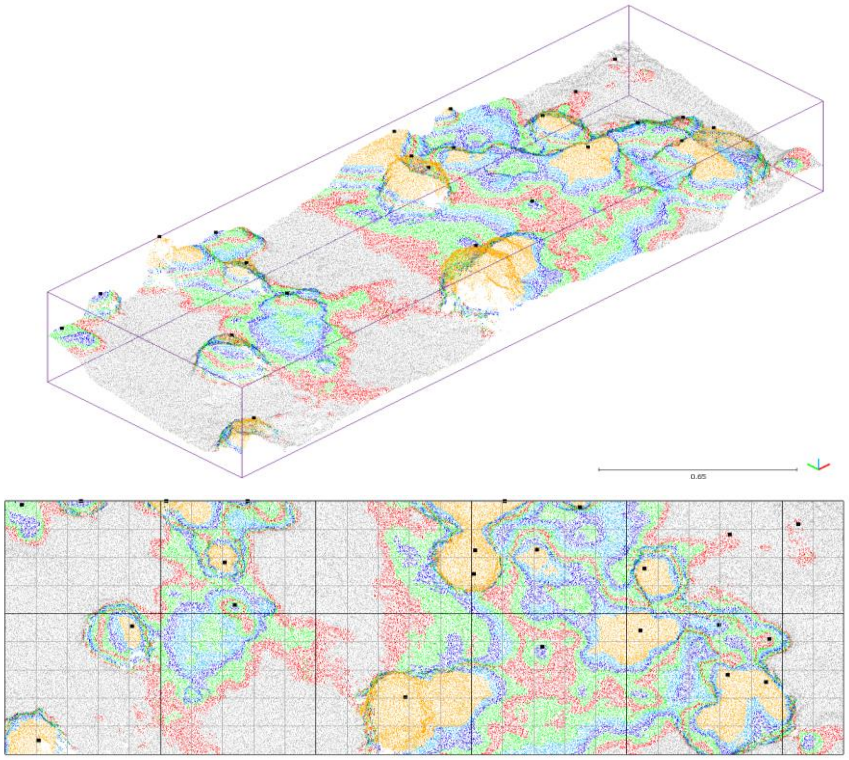

Figure 7-19: Spongdia peak detection for NN 13.

7.3.8 Sponge Height Calculation

In order to calculate the vertical height of each sponge, the two other products of the previous processes are needed: the seamless DTM and the sponges Peak. The calculation of the sponge's height will be derived from individual Z values of each Peak, subtracted from the interpolated Z value of the projected point on the interpolated DTM.

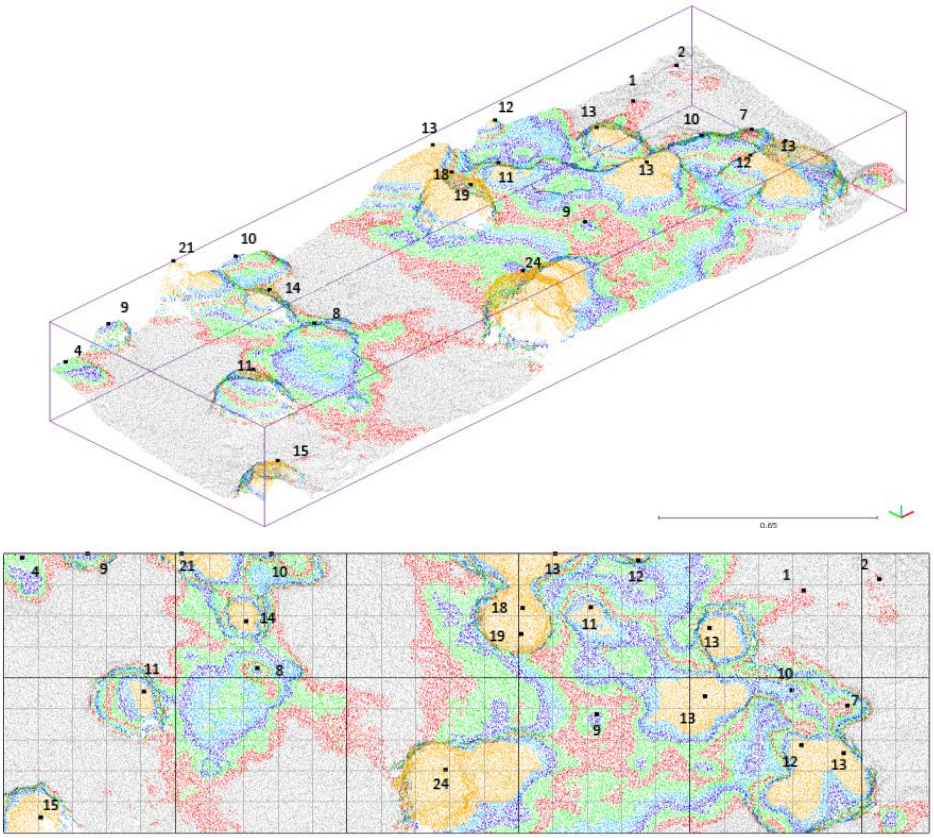

Figure 7-20: Sponges height calculation by Spongdia.

7.4 Volume Estimation of Biomass

Biomass estimation and calculation are subjects of biological and renewable energy, generally described in terms of net loss or net gain for an appointed period.

Biomass is the total mass of living material measured within a specific area. Since all living things contain water, the first concern is the weight of mass including the water called "fresh mass". However, the percentage of water can vary widely from species to species, therefore

biomass is calculated as a dry mass. Dry mass is the mass of biomaterial that is left after all the water is removed. Usually scientists use an oven to remove all the water from the plant or animal material before weighing it to determine its biomass. (Ravindranath & Hall, 1995)

There are several methods for biomass calculation, most of which use volume information as an essential prerequisite within the determining formula (Fang & Wang, 2001).

In this sub-chapter the volume estimation that is provided can be considered as total fresh mass or wet mass, and by providing the result of the weights of the dried sample (per m^3) from the laboratory the total Biomass from the image data can then be determined.

The volume calculation method applied in this thesis is based on earthwork volume calculation methods using two surfaces with the same base and resolution.

The output of the SfM process provides one surface as the Digital Surface Model (DSM).It is a surface which contains both the seabed terrain and the unseparated crown of the sponges. These are the two surface models available after point cloud classification; one is the Digital Terrain Model (DTM) and the other is separated crowns model.

For volume calculation two methods were applied, the first method is based on two individual meshes and the second method is using point cloud. For this procedure *CloudCompare* provides adequate facility which can be used for volume computation. One method is calculating the volume between an arbitrary plane with a constant height and a 2.5D cloud. And the other method calculates the volume between two individual 2.5D clouds.

In order to calculate the sponges' volume by mesh, three steps are needed via *CloudCompare*. Firstly, the two set of the individual surfaces are converted to the closed mesh, one for DSM and the other one for interpolated DTM point cloud. Then the volume of these two closed mesh are calculated with regard to their own base. Since these two mesh have the same source and same base they fit quite well to the same bottom plate. The last step is to subtract the numerical values of the volume of DTM-based Mash from the DSM-based Mesh. The result is the total fresh mass within the surveyed area.

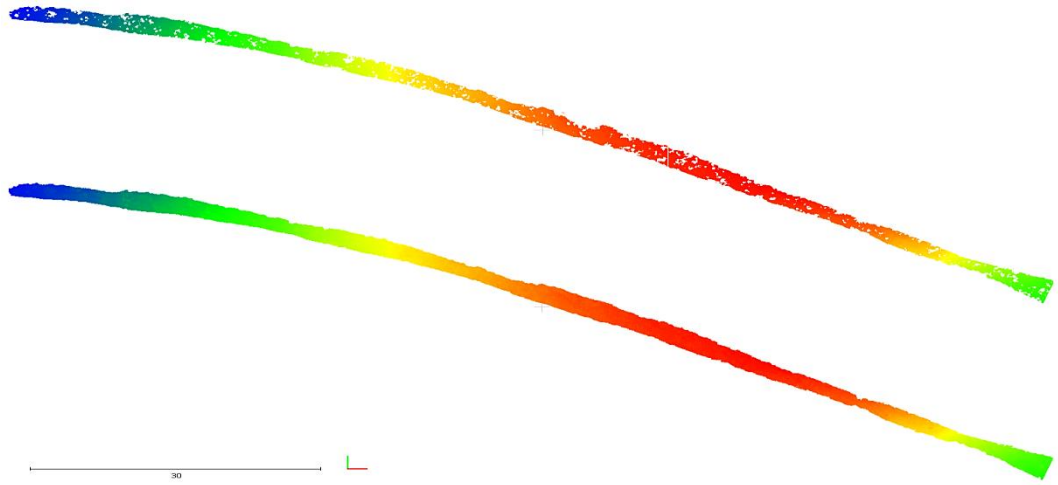

Figure 7-21: Grid calculated for DTM-based Mesh (Top) and DSM-based Mesh (Bottom)

The proper parameters for the volume calculation are applied to both DSM and DTM equally. The grid steps are set to 0.03 m and cell height to “average height” which have to be projected on the Z direction.

For the second procedure the two-point clouds are compared to each other directly, The DTM cloud is used as “Ground/Before” source and DSM is used as “Ceil/After”. There are several factors which must be considered. For the “Ground/Before” source, the DTM cloud has multiple holes which are the gaps of the extracted crowns. Thus, the gaps should be interpolated where there is a need for “Empty cell values”. Also, the value of each cell of the grid has to be considered equal to the average cell height. The size of the grid plays a major role in the result accuracy, which should be chosen to fit the requirements with regards to the clouds resolution.

The gridding step tested for three different values, as 5 cm, 25 cm and 50 cm. The calculated volume is illustrated in the relevant sub-chapter (8.5).

7.5 Classification of Side Scan Sonar Dataset

Among the sonar dataset of the OFOBS dives there are two side scan sonar (SSS) datasets as high frequency (HF) and low frequency (LF). The raw SSS data have a navigation problem, due to USBL disconnection during the dives and have been corrected afterwards by adjustment to camera position (Figure 7-6 A). This data has been exported to raster format with false color based on Backscattering Strength in three visible bands (RGB).

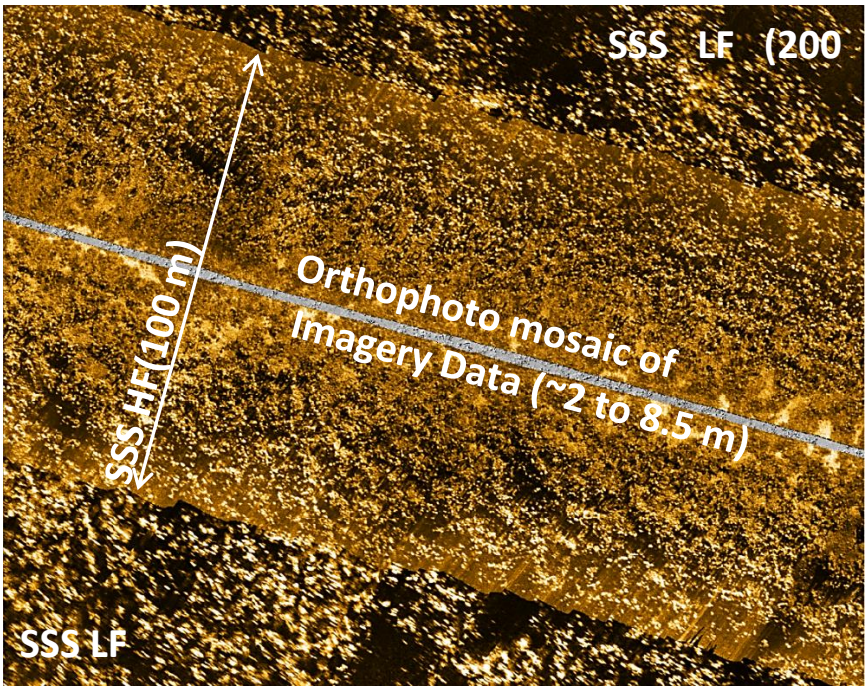

Figure 7-22: Side scan sonar of LF and HF overlaid by orthophoto mosaic of imagery data.

In order to extract the information classes from this data, a set of supervised and unsupervised raster classifications were carried out in *ArcMap* (Esri (Ed.), 2017).

For the supervised classification a multi-variation signature was assigned with more than 400 samples and is based on the three classes of the Acoustic Backscattering Strength (ABS) (Samsudin & Hasan, 2017)

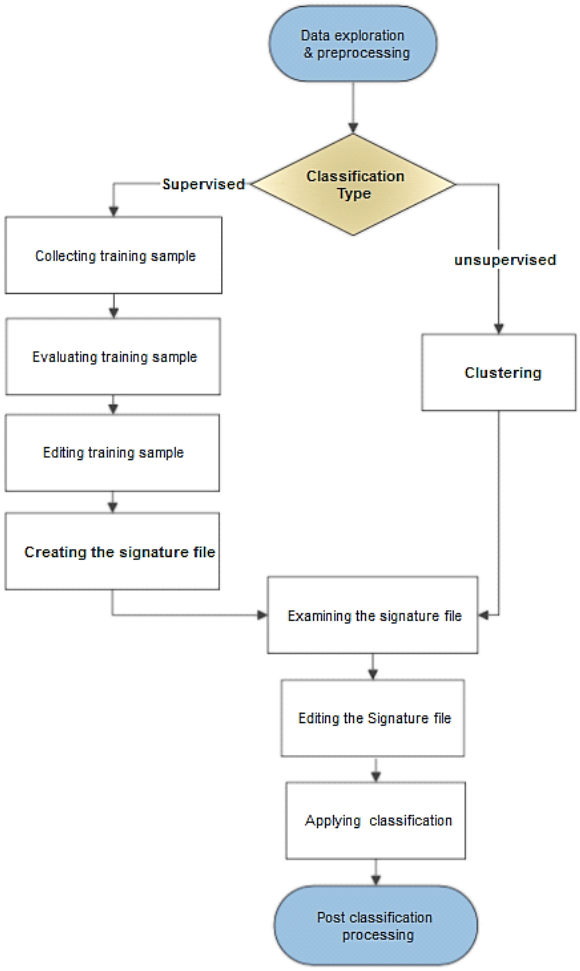

Figure 7-23: Image classification workflow (self-representation based on Esri workflow)

For the classification analysis it is assumed that the data and training samples have normal distribution, and the classification is sensitive for the range of each band equally. The outputs of the classification are illustrated in sub-chapter 8.6.

8 Results

This chapter presents the results of the applied methods described in the previous chapter in the same order of the processing steps. First, the result and outputs of the 3D reconstructed model, then the point cloud Segmentation will come, followed by the result of the sponge Detection by *Spongdia*. The result of the biomass calculation is illustrated in brief and this chapter ends with the result of the side scan sonar classification.

8.1 Primary and Fundamentals

The sample area has many diverse environmental factors at play and may be considered as a challenging sample area. The flat length of the sample area is about 705 meters and with a height difference of 122 meters with a ground slope of 0 to ~50°. Therefore, the distributions of the sponges could be studied over the different ground slopes and different depths.

Also, during the dives, the depth of the OFOBS was manually controlled by the vessel cranes, in order to adjust the flight height of OFOBS to maintain a suitable imaging distance above the seafloor surface. Due to the manually control of the OFOBS during the operation the FH changed very frequently, especially over the slope area (Figure 8-1) which caused a lot of jumps and bounces during the acoustic and imaging survey. The variation of the FH in the sample area is minimum 1.2 m and maximum 8.7m.

The FH of the OFOBS has direct impact on the coverage of sounding and camera footage straightly and exponentially. On the contrary FH has inverse impact on the sounding and imagery quality of the seabed, and Ground Sampling Distance (GSD), as well as negative influence on the 3D reconstructed model. Thus, the point cloud classification accuracy and feature detection quality are indirectly depended on FH.

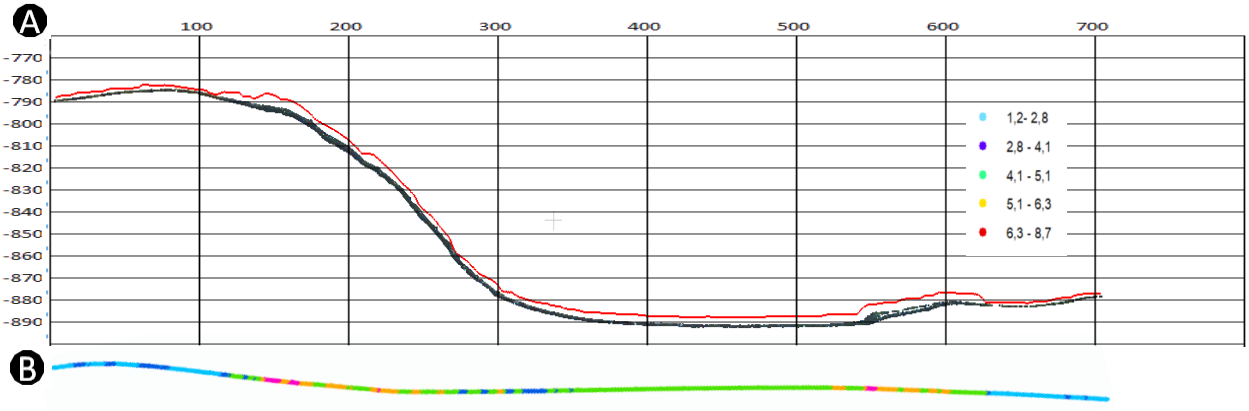

Figure 8-1: (A) a Side view of OFOBS track line (Red line) over seabed terrain along the sample area. (B) The top view of OFOBS FH segmented in 5 categories.

8.2 Outputs of the 3D Reconstructed Model

The *Agisoft* project of the sample area contained 1895 pictures which is just 5 % of the high resolution quality pictures and poor quality extracted video frames, blurred and smudged by the movement and shaking of the OFOBS, and one of the factor which impacts the quality in the point cloud. The following table is representing the property of the constructed 3D model.

Still Images	95
Extracted video frames	1800
Aligned pictures	1895
Tie points	756,365
dense cloud points	103,256,691

Table 8-1: property of the constructed 3D model.

The raw dense cloud is an uncleaned, unclassified multi-resolution point cloud. The density and the resolution of the dense cloud is a derivative of the GSD which is depended to FH. The dense cloud resolution within the sample area varies from 3 to 9 mm. The other raster outputs, such as orthophoto mosaic and DEM inherit the property from the 3D model and are exported with the maximum possible accuracy of 3mm.

The outputs of the SfM are big raster and vector datasets, representing a linear shape (~705 m x 9 m), and cannot be fitted in the A4 paper size dimension. Therefore, a partial demonstration of the same area of each of the outputs is represented in this sub-chapter.

The following figures are representing the main product and side products of the SfM.

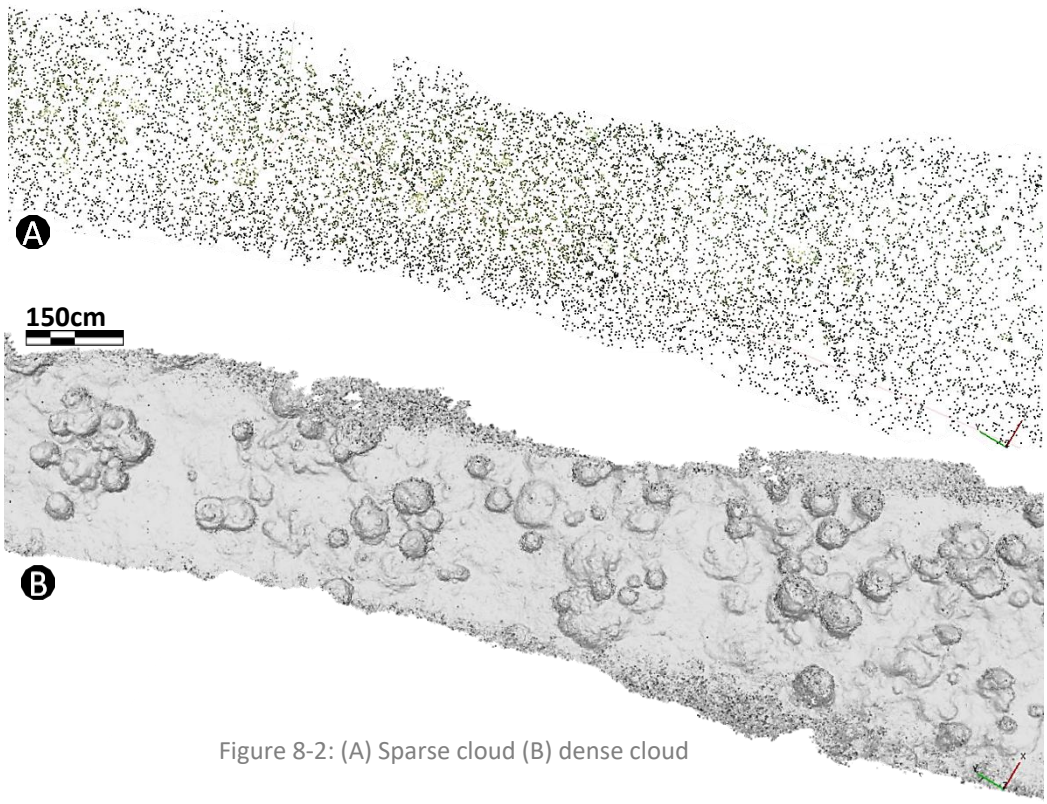

Figure 8-2: (A) Sparse cloud (B) dense cloud

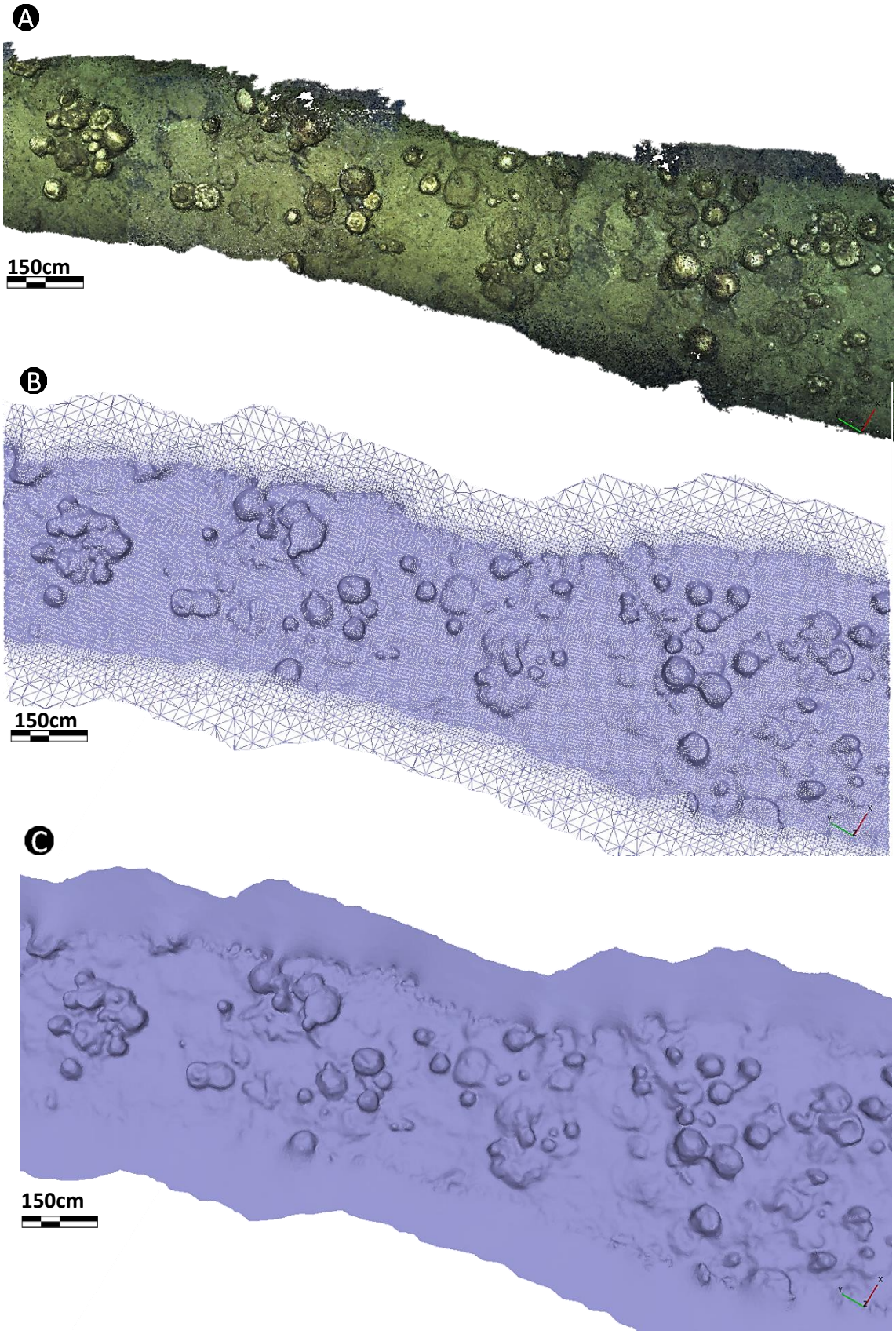

Figure 8-3: (A) Colored dense cloud (B) wireframe model 3D model (C) Solid model 3D model

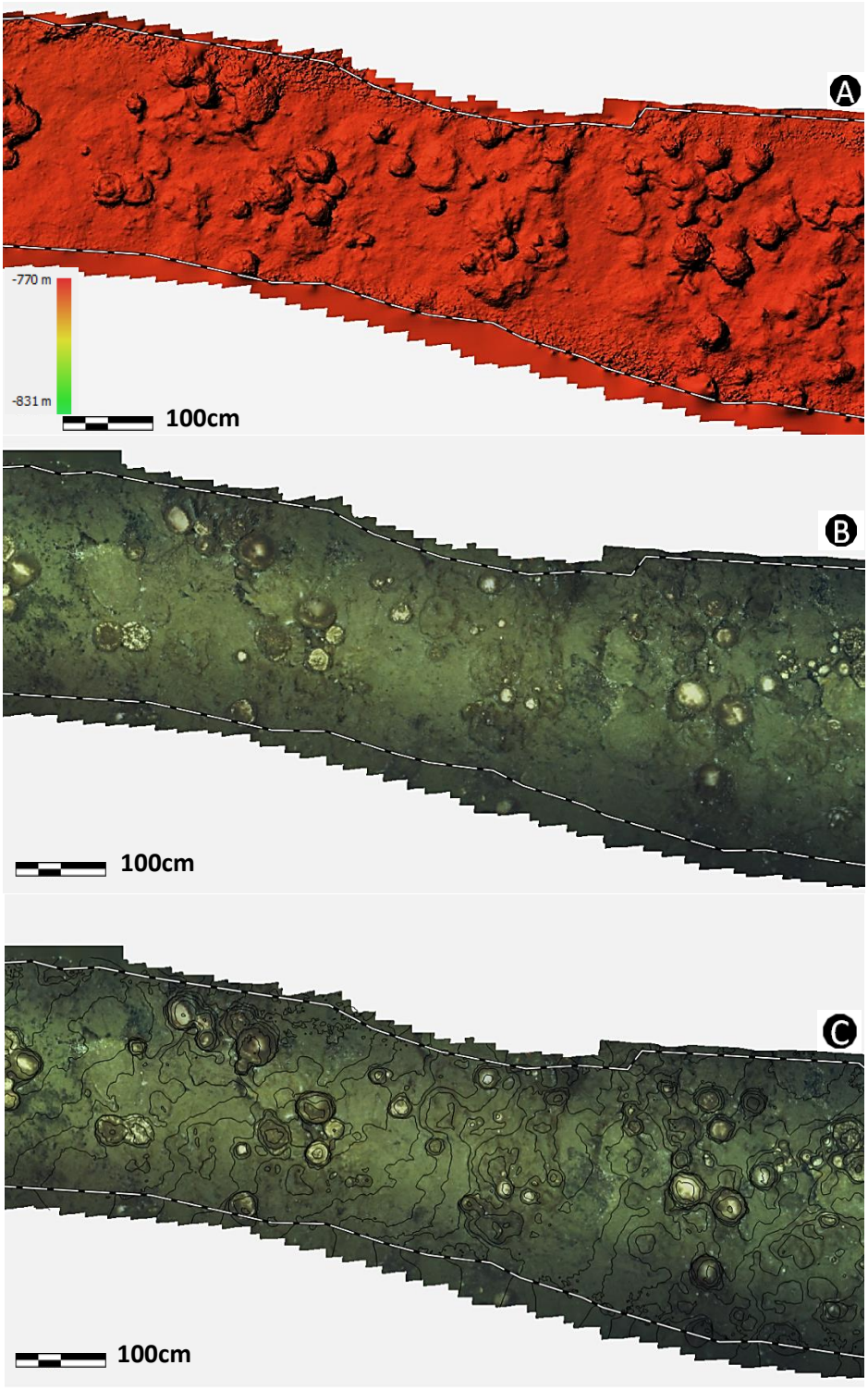

Figure 8-4: (A) DEM from point cloud (B) orthophoto mosaic (C) Contour lines over mousaic

8.3 Point Cloud Classification Results

In this sub-chapter the results of the point cloud classifications are illustrated in three sections. As a matter of the size and dimension of the datasets, a partial chunk of the sample area is demonstrated.

8.3.1 Result of Cloth Simulation Filter

For the Cloth Simulation Filter (CSF) algorithm of *Agisoft*, 19 different combination parameter sets (Max angle / Max distance / cell size) are applied, in order to classify the ground points. The following table and figures are the given combinations and results. (Part of the sample area).

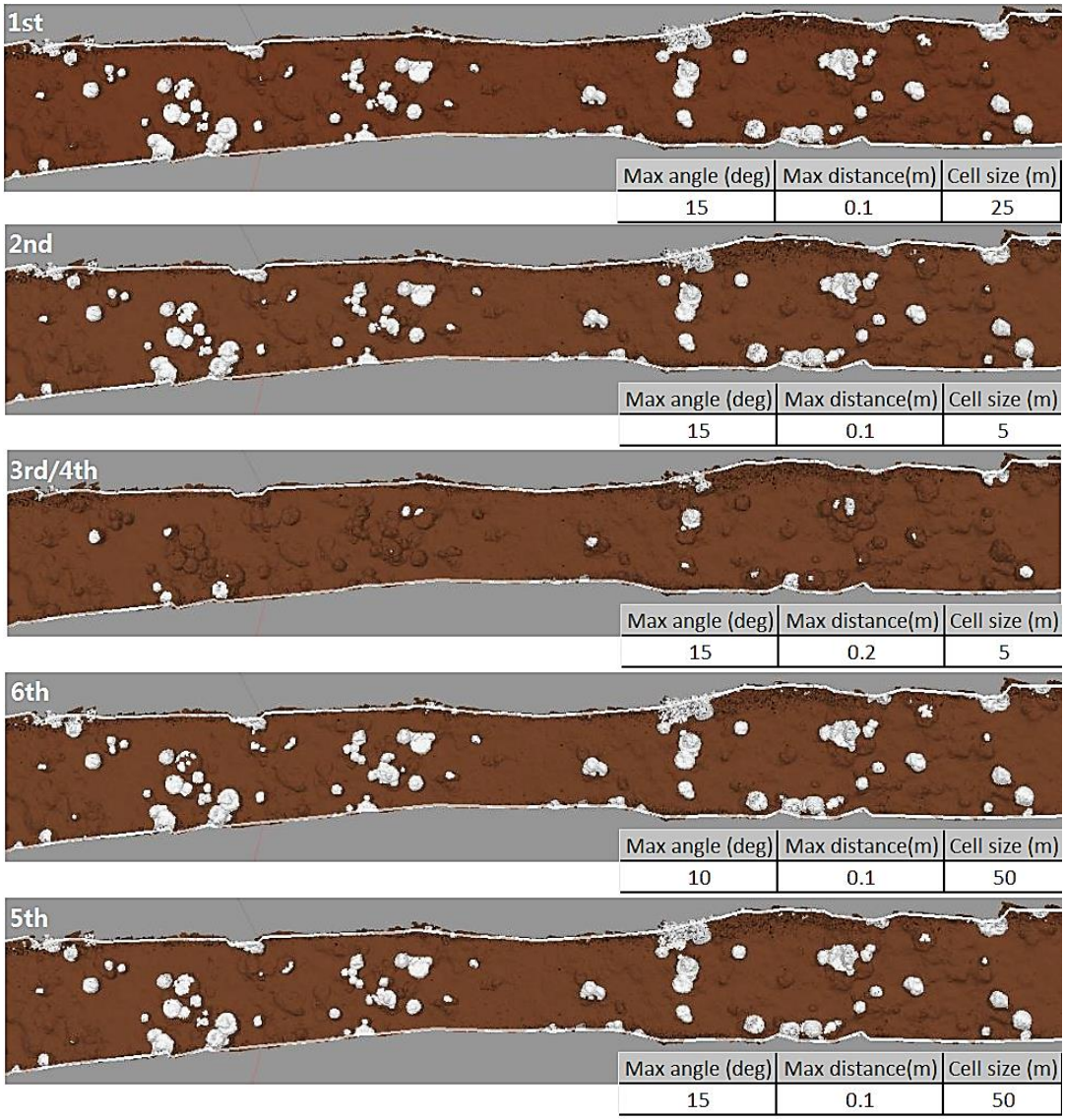

Figure 8-5: Outputs point cloud Classification in *Agisoft PhotoScan* (Parameter sets 1st-6th)

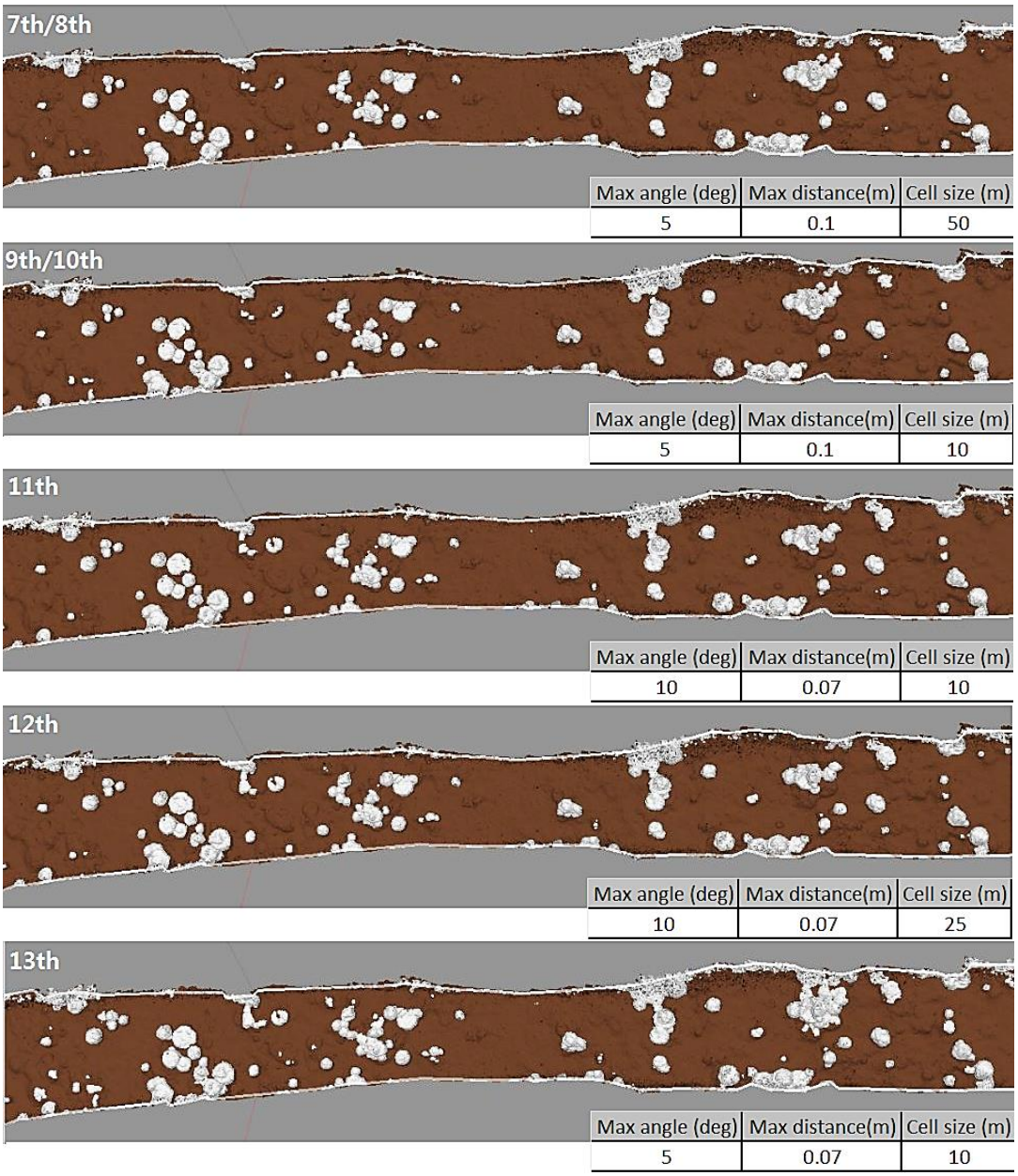

Figure 8-6: Outputs point cloud Classification in *Agisoft* PhotoScan (Parameter sets 8th-13th)

The CSF algorithm cannot deliver good results in the ultra-noisy area. Therefore, several parameter sets were applied specifically in this area in order to get the best possible classification. However, while a parameter set improves classification in this area, it deteriorates the classification in the normal area.

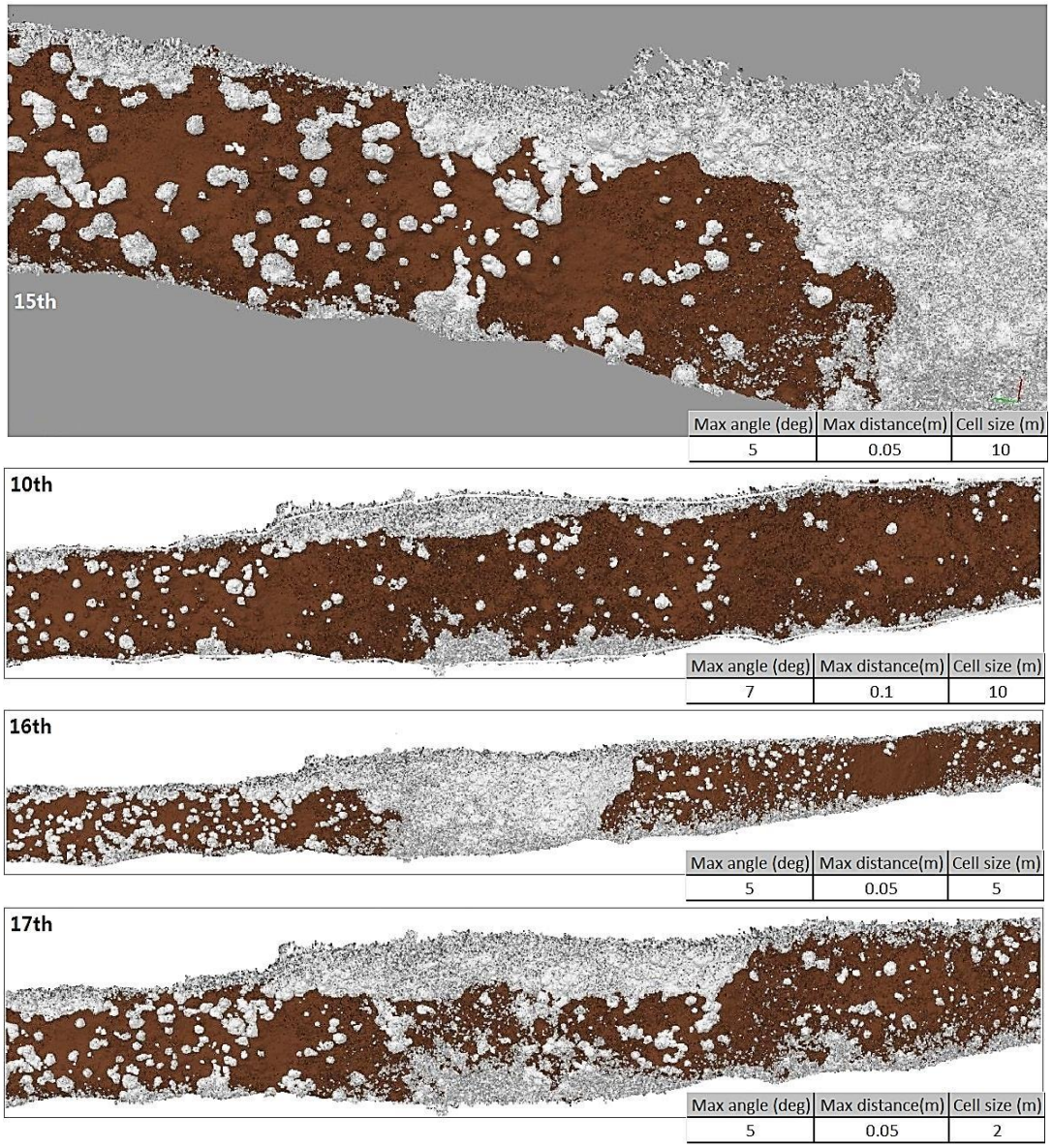

Figure 8-7: Outputs point cloud Classification via *Agisoft* PhotoScan (result in the Ultra-Noisy area)

8.3.2 Result of Roughness Estimation

The remaining unclassified areas have terrain slopes of about 35° in addition to the cross-section slope of 25°, the OFOBS flight height during the survey jumped to 7.8 meter as a matter of crane height changes required by shipborne operations, and all these factors caused low quality imagery with poor light condition on the seafloor and the production of an ultra-noisy point cloud as well. For the ultra-noisy area of the slope three different variables were applied and the flowing figures are illustrating the results.

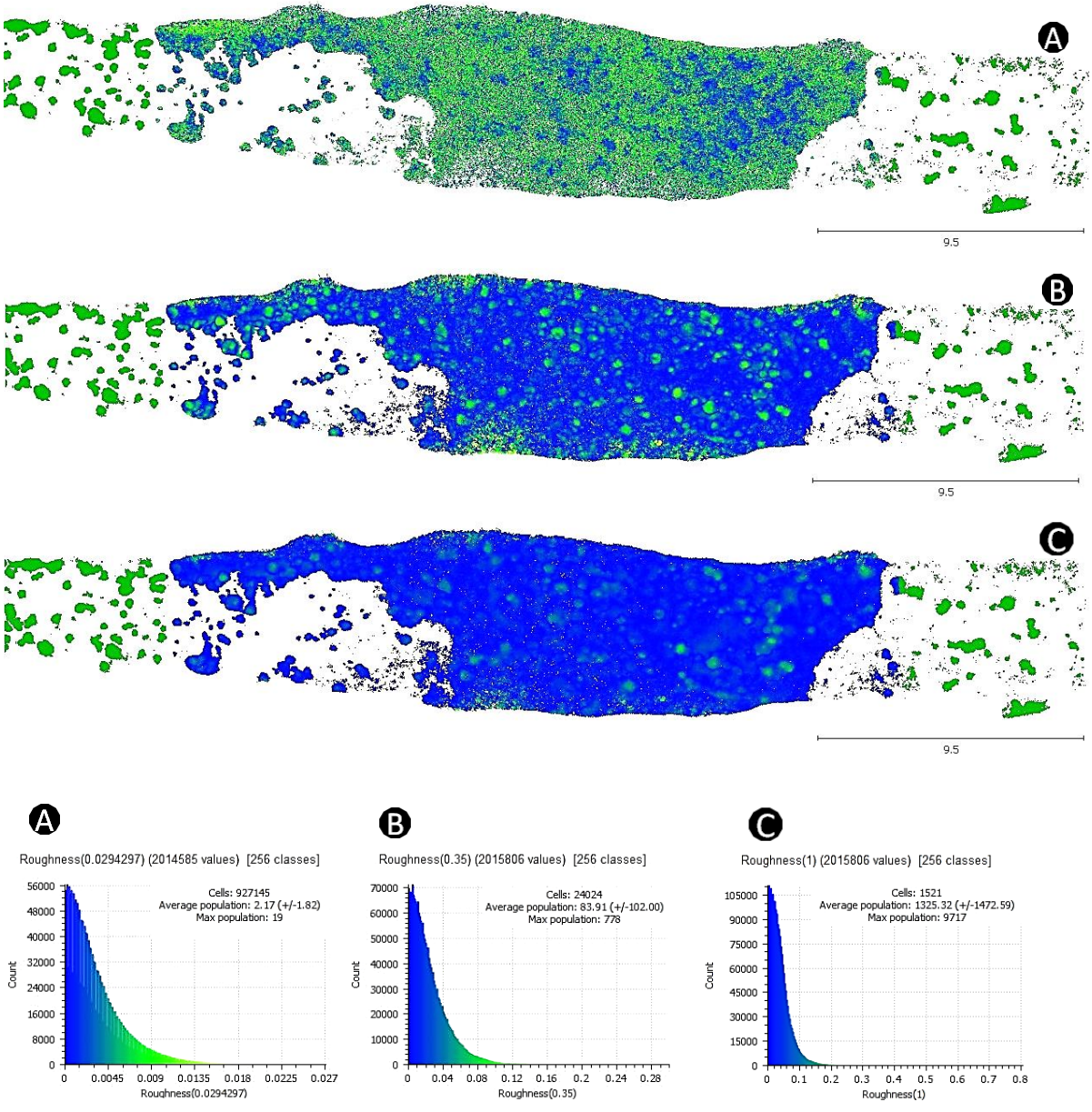

Figure 8-8: Outputs of Roughness estimation over Ultra-noisy area.
The kernel sizes are (A) 3 cm (B) 35 cm (C) 100 cm.

8.3.3 Result of the Roughness Estimation on Bathymetry Grid

Here are the outputs of the Roughness estimation on the bathymetry grid data set, the kernel size 24 cm applied for sponge detection. In the outer boundary the density of the points is not enough for object detection.

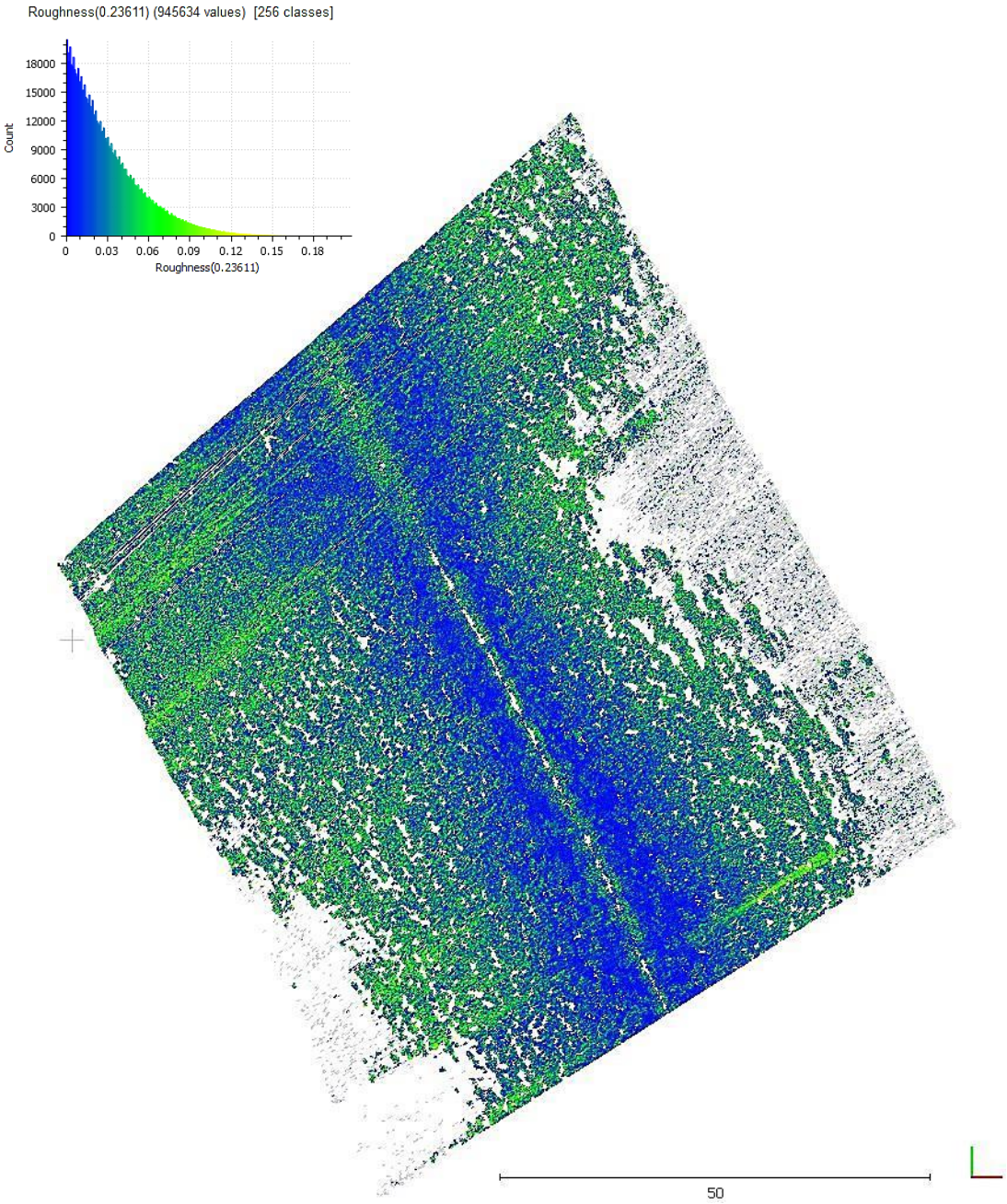

Figure 8-9: Outputs of Roughness estimation for bathymetry point clouds. The kernel size is 24 cm

8.4 Outputs of the *Spongdia*

The sample area for sponge detection is divided into six Sub-Sample-Area (SSA) based on three factors of terrain slope, depth and OFOBS height, since each of these factors have a major impact on the data quality or sponge distribution. Therefore, each of the SSA has its own characteristics regards the three mentioned factors for further comparison and discussion in the subsequent chapter. The following figure and table (figure 8-10) are representing the characteristics of each SSA.

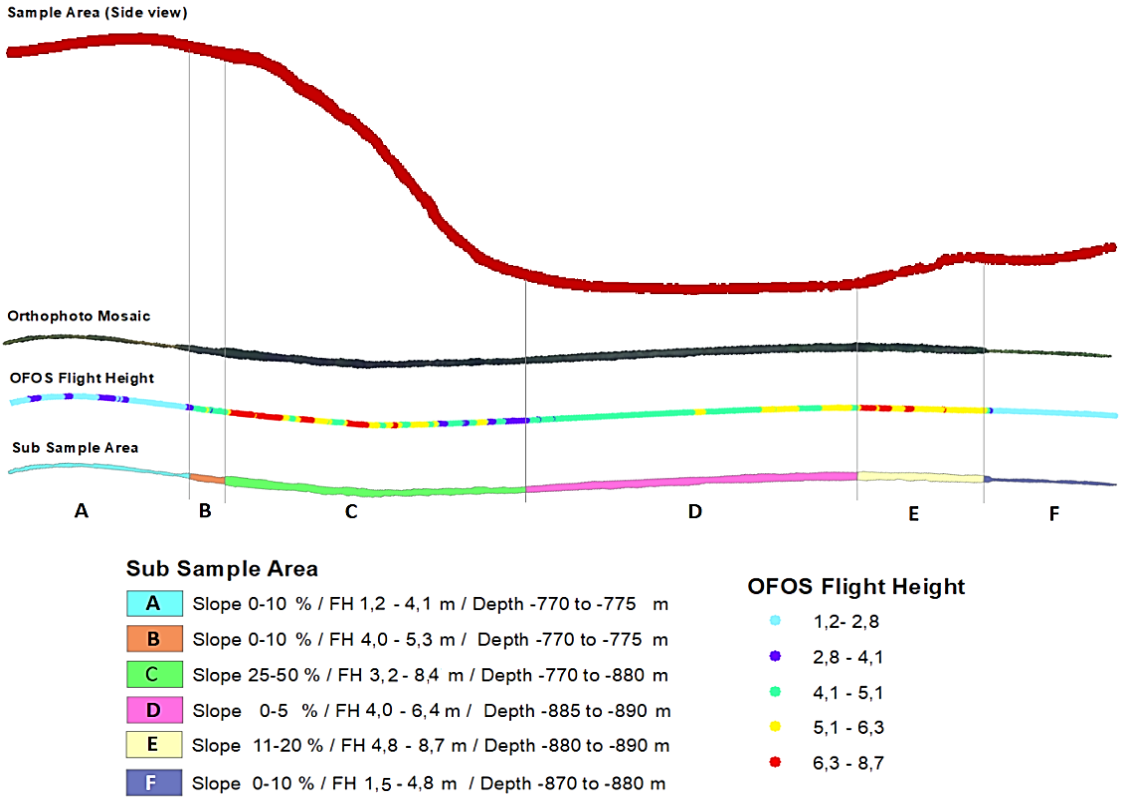

Figure 8-10: The SSA and the characteristic of each area

8.4.1 Detected Peaks

The detected peaks in the sample area for each SSA detected by *Spongdia* are provided in the following table.

During peaks detection with *Spongdia*, 4 different values of the Nearest Neighbor (NN) were attempted for Sub-Sample-Area "A" (SSA-A), in order to compare and find the best value for NN.

SSA	NN	Peaks #
A	9	1636
	13	1204
	25	680
	49	399
B	25	259
C	25	551
D	25	368
E	25	39
F	25	39

Table 8-2: Outputs of peak detection of *Spongdia* for all SSA.

A visual evaluation is attempted in order to find the best fitted values of the NN. The visual detecting and compression of the sponges shows that value NN 13 and 25 are providing a reasonable number for automatic peak detection, thus the NN 25 was applied to the rest of the areas. The Peaks numbers (Peak #) for NN 9 is extra sensitive to the surface change and the NN 49 is missing the small sponges in the dataset.

8.4.2 Ground truth Reference

Within each SSA two procedures were applied, the automatic peak detection as the main method and visual was sponge detection as evaluation evidence. For visual detection part the orthophoto mosaic employed, therefore the visual detection should be judged by the quality of the orthophoto.

The first iteration comparing the two methods reveled that neither of the outputs is perfect to be considered as a reference for the other one. Therefore, an improvement step was applied for the Visually-Detected sponges, in order to enrich the visual detection certainty, by adding the missing sponges with the aid of automatically detected peaks, DEM. The task of visual detection was a little challenging due to the low color contrast of sponges and the background seabed, therefore in some areas it was hard to make the decision if the object is sponge or not. To overcome this uncertainty, a fuzzy logic approach was implemented. The visual detection task was divided in three classes, 1) Easily detectable sponges with about 80% to 100% certainty, 2) Visually Detected with the aid of NN peaks with about 50% to 80% certainty, 3) sponge Spicules accumulation detection with the aid of NN peaks, about 30% to 50% certainty. The following picture is provided an example of the visual detection in the sample area.

Figure 8-4: The example of the sponges which are not easily detectable on visual detection due to low color contrast.

8.4.3 Sub- Sample area “A”

In order to provide a better image on the outputs, the results of SSA-A will be explained in details and the rest of the areas will be compared in the discussion chapter. The SSA-A has about 117-meter length at the depth of 770 to 775 meters. The area is relevantly flat with

some variation with a maximum ground slope of 10%. The OFOBS flight height is at its lowest range to the seabed within the dive between 1.35 to 4 meter. This caused the change in the width of the survey dive from 1.2 to 4.1 meter.

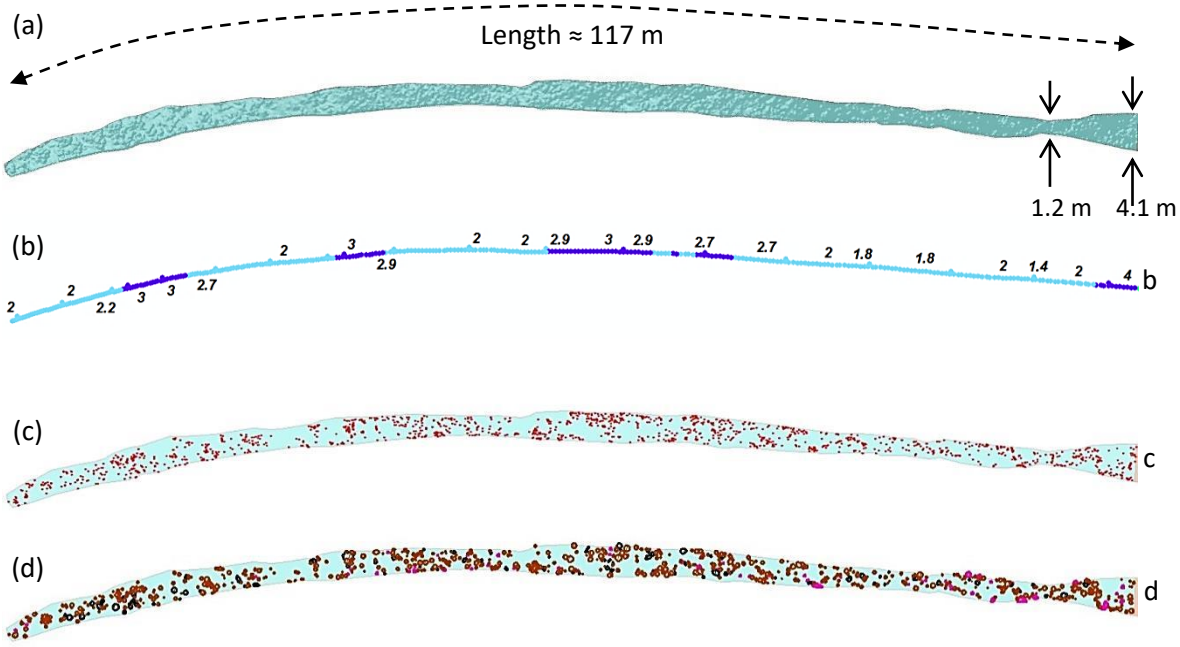

Figure 8-5: (a) SSA-A dimensions, (b) FH values over the track line, (c) Automatically detected peak by *Spongdia*, (d) visually detected sponges.

For the visually detected sponges in the first iteration, 714 sponges are counted with a certainty of 80 to 100% within SSA-A, the second iteration of visual detection attempted with the aid of the detected peaks, which added 62 more sponges and circa-sponges to the previous count, by the certainty of 50% to 80%.

In the third iteration 98% of the area of sponge Spicules accumulation is visually added with aid of NN peaks by the certainty of 30% to 50%. The total numbers of the visually detected objects (with or without aid) are 874 sponges or circa-sponges. The number of the automatically detected peaks varies from 399 to 1636, which depend on the NN values. In general, the larger of the neighborhood values is chosen, it is more likely that the detected peak is a sponge, but it is possible that some of smaller sponges may not be detected.

In the case of a small neighborhood value applies, even smaller sponges will be detected; however, it is possible that even low bumps in the surface are detected as sponges.

For the detection of large sponges, a high value is recommended. This ensures that small bumps are not detected as a sponge. This value can be changed depending on the density and size of the sponges.

The big value (NN 49) is useful for big sponge detection, and the small value (NN9) is useful for geom-morphotypes detection. Then it is mostly evaluated that the NN 45 are big sponges with

high probability and NN 9 are more likely to include the multi peak of the sponges and some caps including sponges and artifacts, a visual evaluation shows that the NN 9 is including any big and small changes in the slope area.

Sponges		1) Easy Detected (80% -100%)		
Visually-Detection		714		
Peaks		Detected Peaks	Peak in sponges Circle	Percentage of Detected
Detected Automatically	NN 9	1636	514	72
	NN 13	1204	480	67
	NN 25	680	411	58
	NN 49	399	325	46
Sponges		2) Visually Detected with aid of NN peaks (50% - 80%)		
Detected Manually		62		
Peaks		Improvement	Percentage of improvement %	
Detected Automatically	NN 9	56	8	
	NN 13	61	9	
	NN 25	62	9	
	NN 49	9	1	
Sponges		(3) Sponge spicules accumulation with aid of NN peaks 30% - 50%		
Detected Manually		98		
Peaks		Within sponges Circle	Percentage of Detected %	
Detected Automatically	NN 9	94	96	
	NN 13	88	90	
	NN 25	61	62	
	NN 49	22	22	
Sponges		Total		
Detected Manually		874		
Peaks		Within sponges Circle	Percentage of Detected %	
Detected Automatically	NN 9	664	76	
	NN 13	629	72	
	NN 25	534	61	
	NN 49	356	41	

Table 8-3: Result of automatically and visually detection of the SSA-A.

In order to provide a better explanation for the table 8-3 the following set of pictures is explained by the differences-

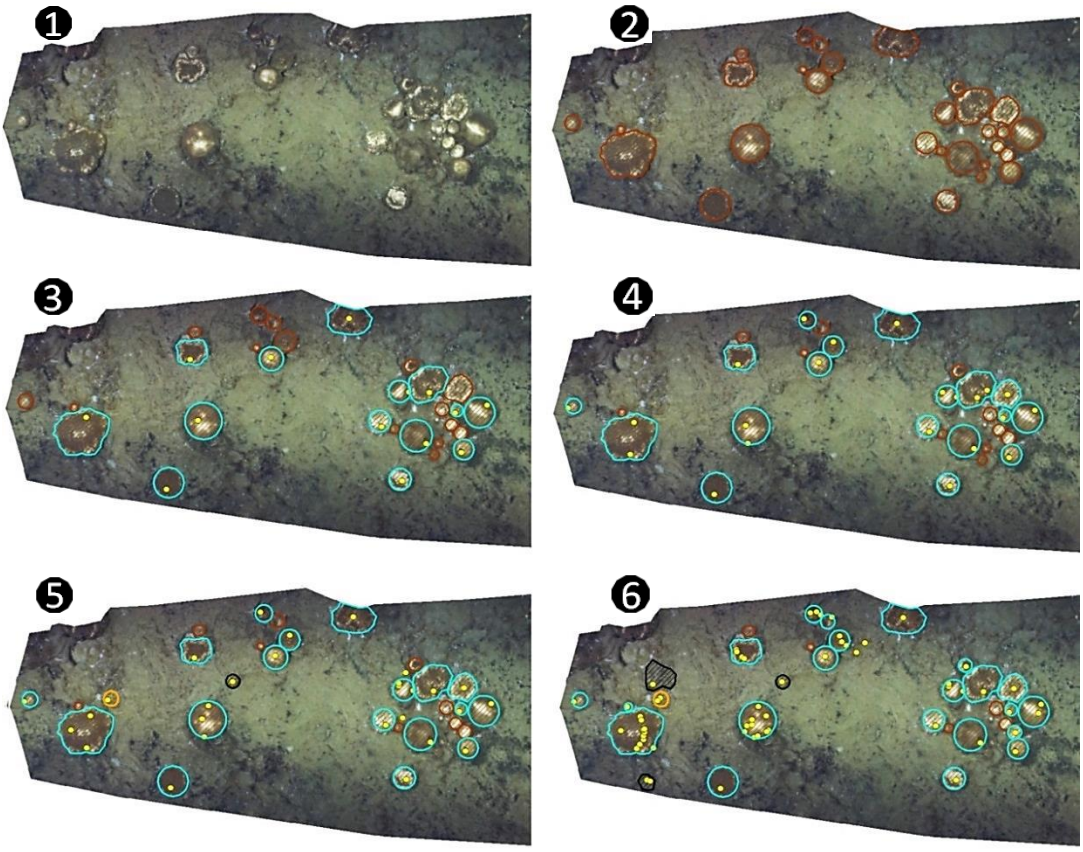

Figure 8-6: Comparison of the automatic and visual detection on detailed view of SSA-A

The upper table image (2) shows the sponges that were visually detected at first sight named as “Easy Detected”, which are marked in brown color.

The middle left picture (3) shows the detected peaks with an NN value of 49, which are marked with yellow dots. Due to the high NN value, the large sponges are easily detected, but small sponges are rarely detected.

The right image (4) shows the detected peaks within a neighborhood of 25. In addition to the large sponges, which were recognized with a neighborhood of 49, medium-sized sponges are also detected here. Some big sponges are determined with two peaks.

The results with an NN value of 13 can be seen in the lower left image (5). Here are some peaks that were detected that are no or not visually recognized as sponges. These are either small elevations in the area, visually unrecognized sponges (orange circle) or Sponge spicules (black circle).

The last image (6) shows the results of a neighborhood with a value of 9. With this value even the smallest sponges are found in some areas and larger sponges are recognized with several peaks. The advantage of NN 9 value is to be able to detect any small elevation and bump in the dataset, but in the same time it will be affected by the low quality of the point cloud very easily.

8.5 Result of the Volume Estimation

In this sub-chapter the result of the two methods for volume calculation (chapter 7.4) is provided.

8.5.1 Result of the Volume Estimation from Mesh

The result of the DSM and DTM volume calculation from the mesh are as follow:

Layer	Grid Steps (m)	Size	Calculated volume(m^3)
DSM based Mesh	0.03	3599x1552	202,294.707
DTM based Mesh	0.03	3597x1552	164,880.177
Total fresh Biomass	-	-	37,414.53

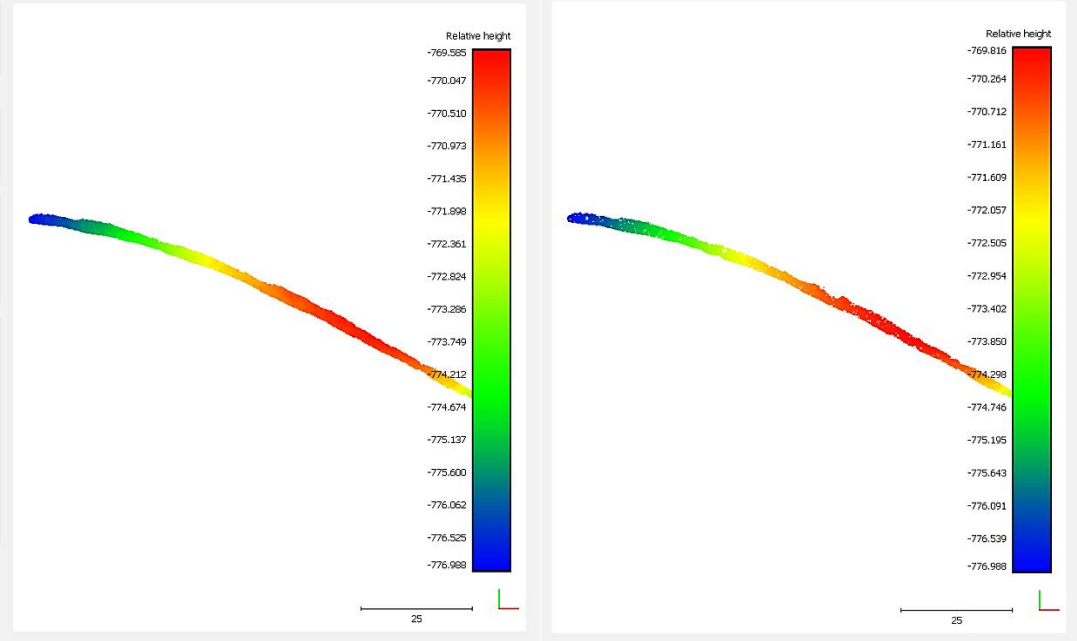

Figure 8-7: Volume calculation on DSM-based Mesh (Left), and DTM-based Mesh (Right), the Grid steps are 0.03 m, the z value calculated for average cell height within each grid.

The resolution and the accuracy of the volume calculation is dependent on the prospective chain of process, including 3D reconstruction model, point cloud resolution and classification in addition to the mesh generation step and volume calculation for Individual Meshes.

8.5.2 Result of the Volume Estimation from Point Cloud

The results of the volume calculation for SSA-A with three tested grids steps (5cm, 25cm, 50cm) are provided in this sub-chapter.

Ground source: DTM Cloud Empty cell value: Interpolate Ceil Source: DSM Cloud Grid step: 0.05 Grid Size: 2160 x 931 Projected dir. : Z Cell height: Average	Volume: 23.982 / Surface: 769.940 Added volume: (+)24.394 Removed volume: (-)0.412 Matching cells: 99.6% Non-matching cells: ground = 0.0% ceil = 0.4% Average neighbors per cell: 8.0 / 8.0

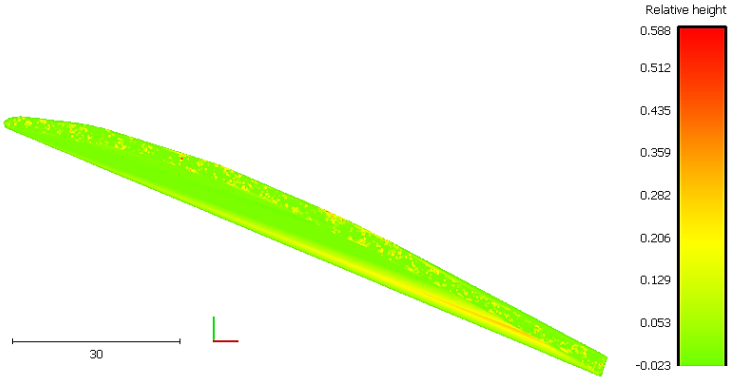

Figure 8-8: Volume estimation for point cloud with 05 cm grid step

Ground source: DTM Cloud Empty cell value: Interpolate Ceil Source: DSM Cloud Grid step: 0.25 Grid Size: 433 x 187 Projected dir. : Z Cell height: Average	Volume: 14.560 / Surface: 778.938 Added volume: (+)14.562 Removed volume: (-)0.003 Matching cells: 99.6% Non-matching cells: ground = 0.0% ceil = 0.4% Average neighbors per cell: 7.8 / 8.0

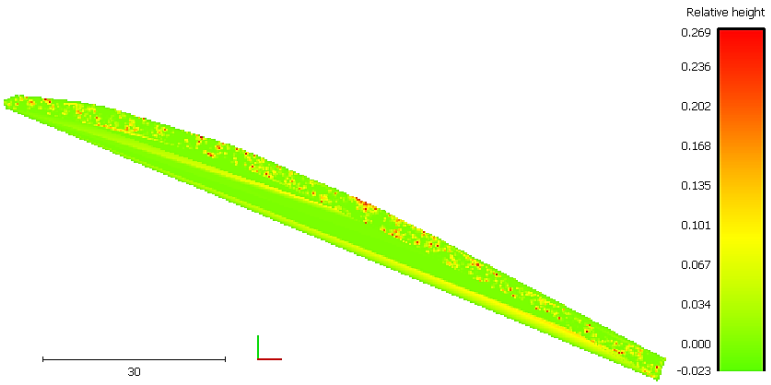

Figure 8-9: Volume estimation for point cloud with 25 cm grid step

Ground source: DTM Cloud Empty cell value: Interpolate Ceil Source: DSM Cloud Grid step: 0.5 Grid Size: 217 x 94 Projected dir. : Z Cell height: Average	Volume: 18.748 / Surface: 801.750 Added volume: (+)18.759 Removed volume: (-)0.011 Matching cells: 98.7% Non-matching cells: ground = 0.0% ceil = 1.3% Average neighbors per cell: 7.5 / 8.0

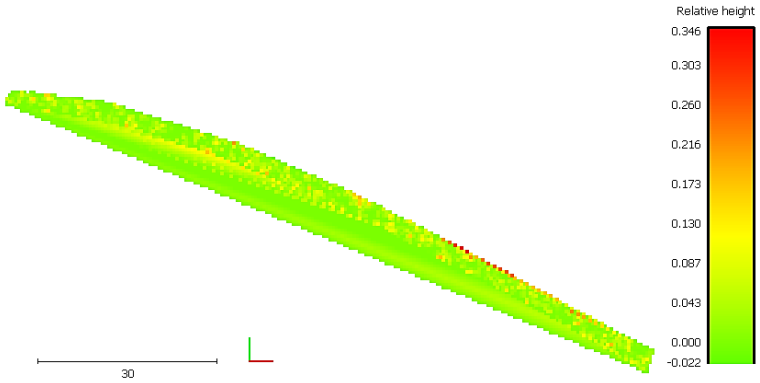

Figure 8-10: Volume estimation for point cloud with 50 cm grid step

8.6 Result of the Side Scan Sonar Classification

The supervised classification assigned with covariance matrix of the signatures values to cluster the SSS raster file, the signatures based on three classes of ABS level. In total 401 sample assigned as signatures

Class ID	Number of Cells	Class Name
1	215 (54%)	1- High Intensity (75-100)
2	161 (40%)	2- Low intensity (25 to50)
3	25 (6%)	3- In between (50-75)
0	0	4-No or very low intensity (0- 25)

Table 8-4: Signature assigned to the intensity classes

The forth class is automatically generated for the remaining unclassified cluster which is the area with no intensity or less than 25% .The following figures are illustrating the signature of sample areas for resampling Nearest Neighbor(NN) of 25 and 10.

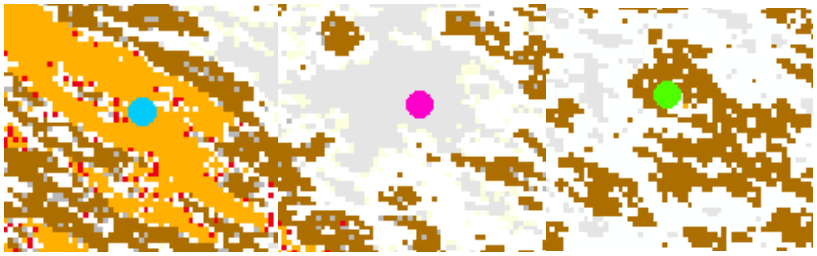

Figure 8-11: Signatures of three classes over the classified area by the 25 Nearest Neighbors

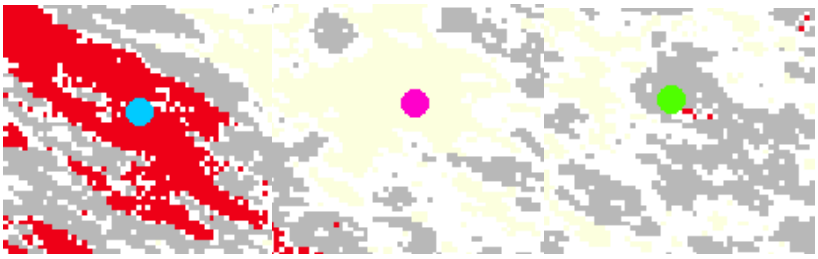

Figure 8-19 Signatures of three classes over the classified area by the 10 Nearest Neighbors

Figure 8-20: No intensity or less than 25 % is classified as blanked

Figure 8-21: Classified SSS LF with 25 NN

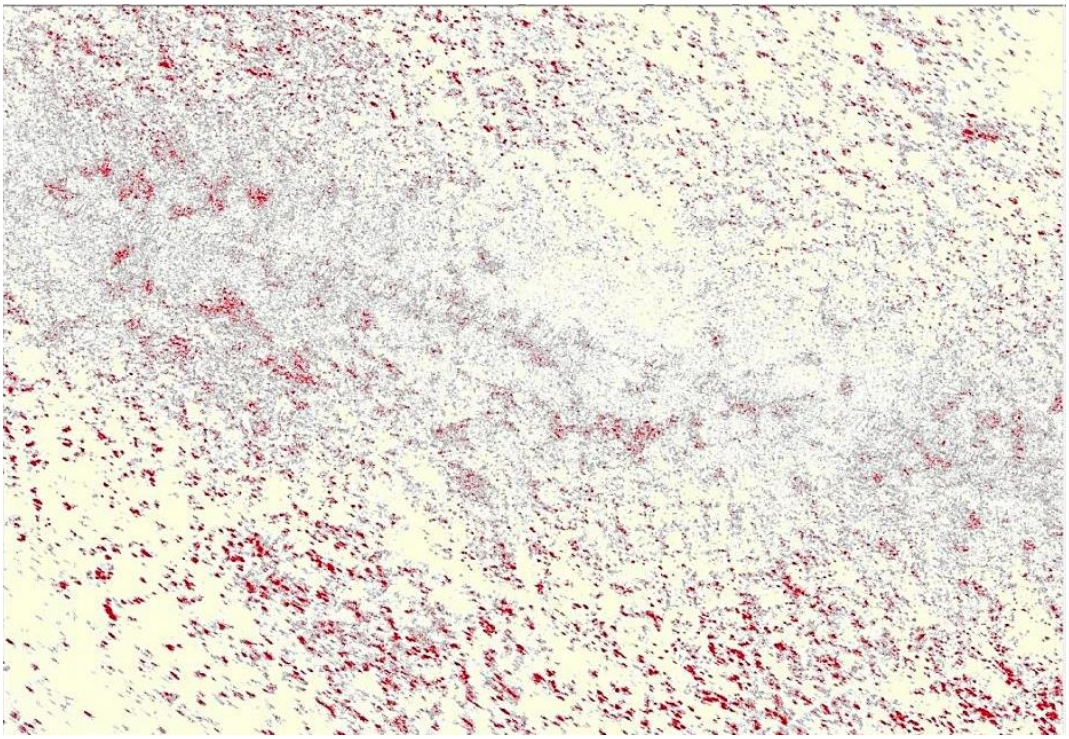

Figure 8-12: Classified SSS LF with 10 NN

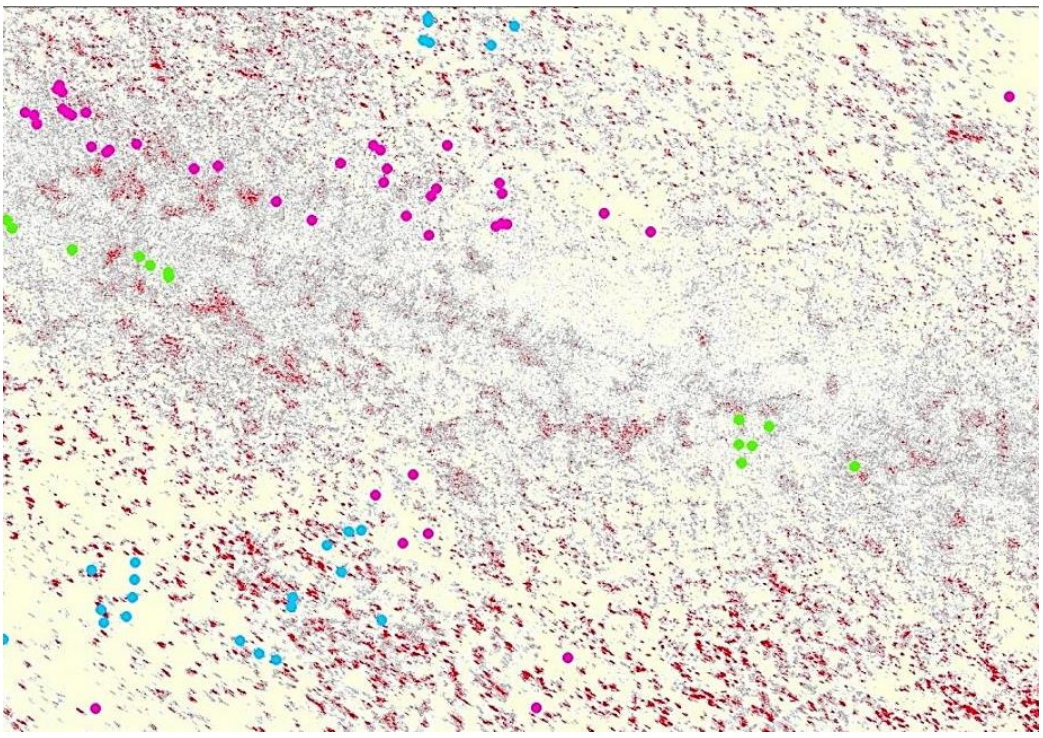

Figure 8-13: Distribution of the three classes of the signatures over the classified SSS LF with 10NN

9 Discussion

The analyses of the results are provided in the following sub-chapters, starting with a brief explanation about the uncertainty estimation. The capability and reliability of the 3D reconstructed model and the mapping products are explained in the second place. The third subchapter delves into the sponge and Peak detection by *Spongdia* in comparison with visual sponge detection. Then the two methods of the Volume calculation will be compared, followed by the interpretation of the side scans sonar classification. This chapter ends with further possible datamining and recommendations to improve the OFOBS installation and survey planning.

9.1 Uncertainties Estimation

To compute with the uncertainty of a multi-sensor, multi-platform dataset is a complex task which could be considers especially difficult where the data acquisition is accomplished in the harsh environment of the Arctic Ocean. The dataset which this thesis benefits from is also has such complexity, with several dependency and undefinable uncertainties. This section attempts to provide a brief discussion about this matter in two parts: 1) bathymetry uncertainty 2) under water photogrammetry uncertainty.

9.1.1 Uncertainty Budget of Bathymetry

The International Hydrographic Organization (IHO) defined the minimum requirement for error budget in the certain bathymetry orders in the 5th edition of (S-44_5E) as the standards for hydrographic surveys (International Hydrographic Organization (IHO) (Ed.), 2008). Theoretically the closest category in S-44_5E which fit to the shipborne dataset is the “Order 2”, described as “Areas generally deeper than 100 meters where a general description of the seafloor is considered adequate”. Beside the OFOBS data is far better than the “Special order”, considering the resolution and local position but not the global position.

The maximum allowable total propagated uncertainty (TPU) is a depth dependent value resulting from the overall combination of all uncertainty sources which contributes in measurements, also known as error budget. It should be computed for each depth point when all the relevant uncertainty sources are known and taken in to account. The s_44_5E notice that the result of the bathymetry is acceptable when 95% of the accuracy values are within 95% confidence level values.

The TPU of the bathymetry and underwater positioning are consisting of the TPU of the position of transducers, in addition to all the factors which are contributed for depth sounding. In

order to comply with the criteria specification of S-44, there are several factors which needed to take into accounts (International Hydrographic Organization (IHO) (Ed.), 2008).

The following table 9-1 is listing the require factors, for TPU calculation and the status of them in Arctic high latitude.

The result of the TPU is due to the combination of all contribution factors of uncertainty, therefore the lack of values affecting the overall result. As the brief information provided in the table 9-1 (Jensen & Sicard, 2010) indicates, it is almost impossible to quantify the error budget of PS101 in high latitude 87° N, while there is more missing and unreliable value for TPU computation.

Contributing factors of TPU	Status of PS101
Geoid model / Projection	WGS 84 / UPS North (N,E)
GNSS position	No coverage of the GNSS correction systems and less GPS coverage
gyro heading	Become ineffectual at high latitudes as the earth's spin rate is less at higher latitude
pitch	Effected by Ice braking
roll and heave	
mounting	√
beam range	Effected by Ice flow beneath the transducer
beam angle	
beam width	
beam steering	
sound velocity at transducer head	Dives is in touch with the melting ice and ice
sound velocity profile	Not in the specific interval
Tide value	Not available and the tide models are not covering the ice
Node offsets / lever Arms	√
Bathy depth	√
Timing offsets / latency	√
draft	Changing due to the Ice braking condition

Table 9-1: Elements of TPU computation and their status in high latitude. Own representation adapted from *Jensen & Sicard (2010)*.

To provide a better image for uncertainty factors, the following picture (figure 9-1) is illustrating a simplified TPU of MBES with unrealistic assumptions that, regardless to the vessel attitude, the IMU has no uncertainty and vessel sounding is in stationary position.

The RV Polarstern has its own coordinate frame defined and calculated within vessel survey (Appendix A), where all the sensors on bored are referred to. The MBES indi-

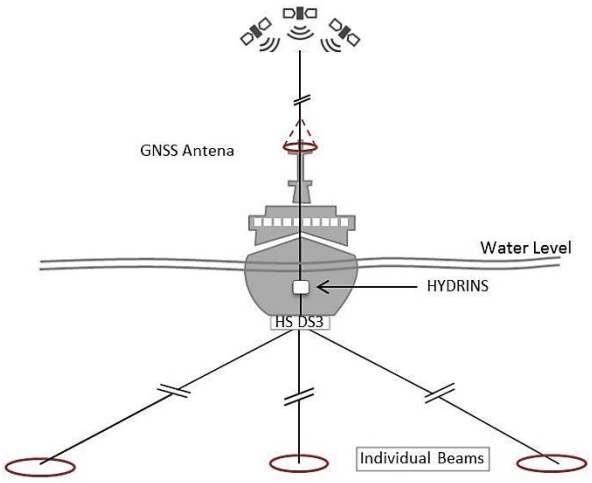

Figure 9-1: Schematic illustration of TPU for MBES

vidual beams and USBL positioning system measurements also refer each individual ping to a transducer with regards to the vessel frame. The only connection from the vessel frame to the global frame is via Trimble SPS855 GNSS solution (3.1.2). As it is mentioned in chapter 3 the system provides sub-centimeter accuracy in Real-Time Kinematic (RTK) mode and less than 5 m 3DRMS with Satellite Based Augmentation Systems (SBAS) for positioning, while the RTK and SBAS solutions are dependent on reference stations. Since the land station signals could not reach the vessel in the open ocean the RTK modes are useless, and SBAS covers only distinct areas on the northern hemisphere and are not able to cover the high latitude Arctic Ocean, therefore the uncorrected standalone GPS accuracy is estimated about 10 to 15 m (C.J. de Jong, 2010).

The next sensor is the iXBlue HYDRINS INS, where the position is combining with the vessel attitude. The manufacture provides two different values for aided and unaided with GNSS which has some time latency for real time positioning. The non-aided values for the attitude accuracy are 0.2 (RMS) and 0.1 (RMS) for heading while the aided outputs are two times better than no aided (iXBlue-SAS, 2016). However, the accuracies are much worst in high latitude conditions especially during Ice-breaking.

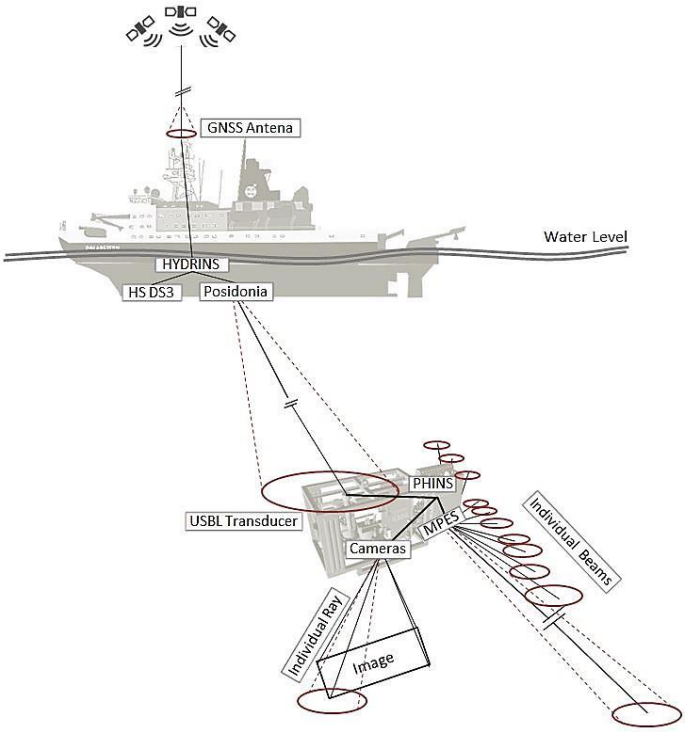

Figure 9-2: Schematic illustration of TPU for OFOBS camera and sonar system. Own representation adapted from (WATI et al., 2016)

For the USBL uncertainty, the manufacturer claims the 0.2% of the slant range, which in the sea-ice coverage of the Langseth Ridge, is impossible to achieve since the acoustic underwater positioning system is highly effected by the environmental characteristics.

Thus, the TPU of the OFOBS is also affected with the same factors presented in table 9-1 in addition to the USBL uncertainty and some transformation of the OFOBS sensors uncertainty, such as PHINS and pressure sensor.

Furthermore, there were frequently disconnections between the vessel USBL antenna and OFOBS transponder, which produces a series of random jumps in the OFOBS position data (Purser et al., 2018). Moreover, the structure of the positioning measurement chain causes the uncertainty accumulation at the end of the multi-sensor measurements system of OFOBS, partly due to the data flow passing from GNSS antenna to the cameras and transducers. Therefore, the computation of the position for OFOBS is also unquantifiable.

9.1.2 Uncertainty Budget of Imagery Data

For photogrammetry there are several well-known geospatial standards which cover different areas of the photogrammetry and remote sensing, such as the series of technical ISO standards by the International Society for Photogrammetry and Remote Sensing (ISPRS), but none of them cover the specification requirement for underwater photogrammetry.

The principals of the Industrial, terrestrial and aerial photogrammetry are similar, since all of them needs a sequence of images with sufficient overlap in order to construct a virtual 3D model for the measurements, while they are different in platforms, planning, target model and accuracy (Mikhail et al., 2001). Underwater photogrammetry also has some areas in common with the other type of photogrammetry, while the distinctive aspect is the media which the images are captured within. The refraction and absorption of the light is bigger in the water and also the depth of water has big influence in light ray behavior due to the stratification caused by temperature, pursuer and salinity (Steele et al., 2009).

In the conventional photogrammetry it is essential to establish a network of ground control points (GCPs) in order to transfer the relative location and dimension of the 3D model to the global frame with an acceptable scale and level by absolute orientation step. With the development of the technology, a new method is developed for geo-referencing without using GCPs. In this method the Camera Exposure Positions (CEPs) of the center of the photo is recorded by GNSS on board the platform. The more accurate positioning causes more accurate CEPs thus more accurate 3D models and mapping products such as DEM and orthophoto mosaic. It is possible to increase the accuracy of the 3D model by integrating the camera orientation at the time of the exposure by implementing an accurate IMU in the imagery system or platform (Carbonneau & Dietrich, 2017).

Since it is almost impossible or at least not cost-efficient to establish GCPs networks beneath of the Arctic Ocean, the CEPs are the best alternative for the SfM method. Fortunately, the provided dataset of OFOBS had enough information to build up virtual CEPs for the sample area.

It is essential to mention that the provided SfM technique (chapter 7-1) developed by Dreutter (2017), solved the navigation problem for OFOBS tracking in the local frame which has a shift and rotation with global frame as big as TPU.

As the TPU of the cameras positions are affected by the USBL position, the TPU of the 3D model is in the same range and incomputable. However, the dimensions of the features on the seafloor could be evaluated by the position of the projected laser dots.

For feature detection, the dimensions of the objects are in concern rather than position, therefore, the uncertainty of the position and the dimensions should be considered separately.

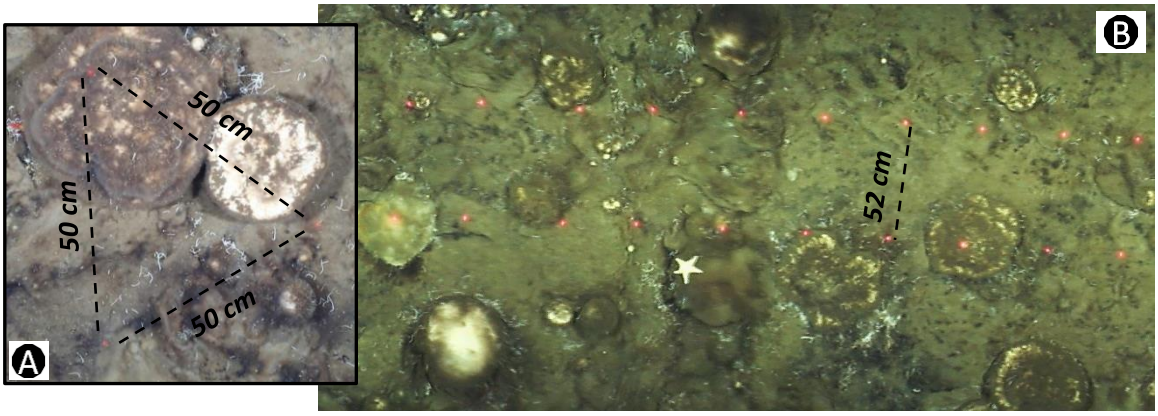

Figure 9-3: (A) The triple laser dots on the stills images. (B) The laser spots at the orthophoto mosaic

The dimensions of the triple laser dots on the nadir of the OFOBS are 50cm where the pitch and roll values are zero. Thus, the distance of these laser spots are measured on the unmasked orthophoto mosaic in order to evaluate the 3D model outputs. The mean value of several measurements over the sample area is 52 cm; therefore, it can be concluded that the 2D accuracy of the 3D model is about 0.04 in the nadir area which gets bigger in the outer boundary.

9.2 Capability and Reliability of 3D Model Products

The orthophoto mosaic, DEM and point cloud are the main products of the SfM which are employed for classification and feature detection. They all inherit the properties of the 3D model such as accuracy and resolution in all respects. However, it is possible to improve the virtual resolution of this data, but it does not improve the accuracy and reliability rather the density of the information that is enhanced by the interpolation.

It should be considered that for reconstructed 3D models, two sources of imagery data are employed: 1) extracted frame of video 2) still images. These distinct sources of the data are varying in properties as they come from different cameras with unlike focal length and resolutions and they have a slightly different distance to the seafloor regarding the two individual waterproof housing and installations. Thus, the property of these sources will be discussed as the main source of the 3D model. The capability of imagery information depends on several factors such as: cameras properties, camera installation and object distance (Fekete, 2008). The camera properties are defined by the manufacturer which partly could be modified via the camera settings. The following table (9-2) is comparing the main properties and settings of the video and stills camera in brief.

properties	Video Camera (Sony FCB-H11)	Stills Camera (Canon EOS 5D Mark III + 24 mm fixed lens)
Resolution name	2K (Full HD)	6K 3:2
Aspect ratio	1.75 : 1	1.50 : 1
Resolution number	2.1 megapixels	22.3 megapixels
Dimensions in pixels	1920 x 1080 pixels	5760 x 3840 pixels
Total number of pixels	2’073’600	22’118’400
Imaging rate	25 fps (extracted frame 1to 4 fps depends on speed and FH)	1 each 20 sec+ some random manual shooting
Overlap	Minimum 60%	Big gaps

Table 9-2: A brief compression of video and stills camera properties

Regarding the pixels number of each cameras image, the quality of the stills images are about 11 times richer than the extracted video frames.

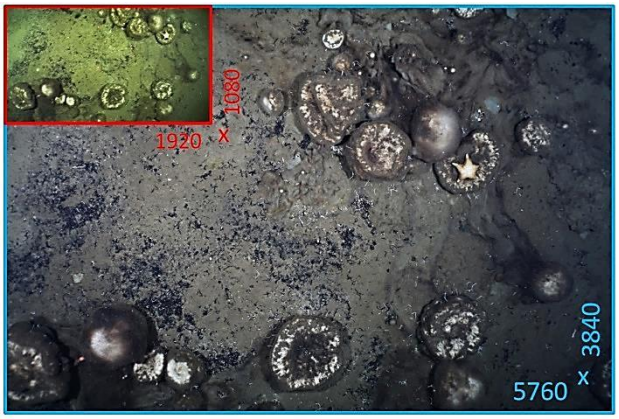

Figure 9-4: Compression of full HD resolution video frames (Red) with 6K resolution still images (Blue)

The datasets provided by both of the cameras vary in many aspects. For example: the extracted video frames are covering the entire OFOBS dive with more than 60% overlap, but the frames are partly blurred and smudged, they consist low resolution and hue in comparison to the still images which provide a 6k high resolution image with notable color balance but there is no overlap in between.

In addition, the illumination during the stills camera shooting was much better due to the extra strobe lighting. Furthermore, the exposure time of the still camera was suitable for dynamic recording, as the shutter time was fast enough to escape the motion effect during the dive. On the contrary the low saturation of the video frames is obvious in the extracted frames and the slow exposure time (25fps) of video captured the moving effect of the

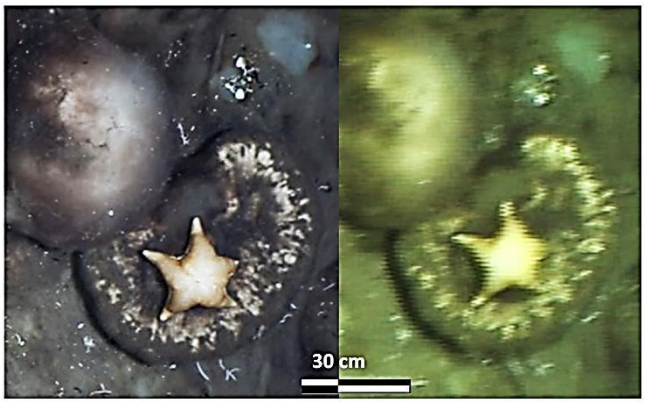

Figure 9-5: Compression of the quality of the still image (Left) and extracted video frame (Right).

OFOBS which caused parallax and smudges in the frames.

The resolution and sharpness of the still images are ideal for visual interpretation and reconstructing a detailed 3D model, but it should be considered that these good images are just ~5% of the images used for SfM and the rest are extracted video frames. Thus, the quality of the 3D model and the mapping products are highly affected by the poor quality of the full HD video camera. There for the ground sampling distance (GSD) is also reduced by the low-quality video frames except in areas that were covered by the still images.

The distance to objects has a big impact on imagery information in different ways. For example, the FH of OFOBS affects the video frames brightness and hue more than the still images synced with extra strobe lights, which is a matter of light absorption in the water. In addition, the ground sampling distance (GSD) is increasing by the higher FH, thus the higher GSD the lower spatial resolution and lower point cloud resolution (Leachtenauer & Driggers, 2001).

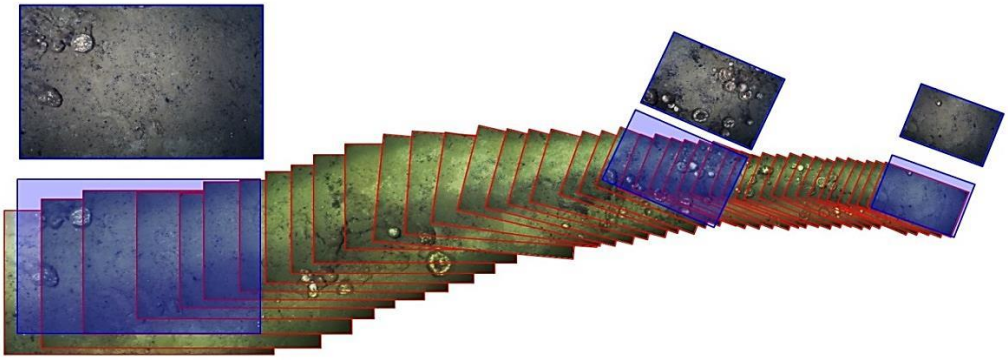

Figure 9-6: A sequence of Individual orthophotos including 42 video frames (Red) and3 stills images (Blue) are illustrating. The overlaps and gaps influenced by the FH. As a matter of inappropriate time interval for automatic shooting, there is no overlap in the track of the still images

The video camera and stills imagery camera are mounted adjacent to each other in the centre of OFOBS. The video camera is tilted to the starboard side of OFOBS in order to cover relatively the same area as the still imagery camera. This orientation is ideal at the FH of 1.5 to 3 meter.

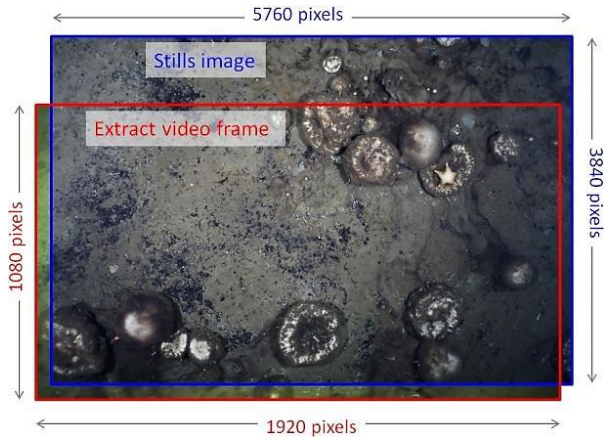

Figure 9-7: Comparison of the coverage and resolution of the still image (blue) and the video frame (red)

The low color contrast of the sponges and background see-floor is a challenge for pattern recognition algorithms which get worst due to the low saturation of video frames

The distribution of the noise is not steady through the dataset. Specifically, the noisy area is mostly in the outer edges of the OFOBS track line

Non-Normal noise distribution constantly appears on the starboard side of the OFOBS track line as a matter of video camera installation which is installed on the port side and tilted to starboard side (Appendix B). The tilted video camera installation makes light ray length longer on the starboard side in comparison to the port side.

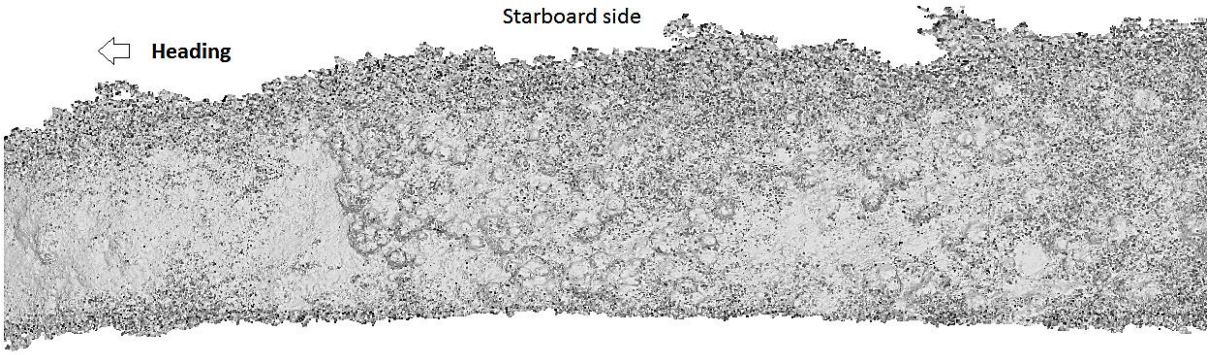

Figure 9-8: Uneven noise at the starboard side compare to the port side due to camera installation.

The noise is increasing exponentially by the slope ratio, likewise within OFOBS flight height where the distance plays a major role in the image quality due to the light propagation within water columns.

The masking of the triple laser points also reduces the quality of the mapping products. The following picture is illustrating the image boundaries and masking boundaries.

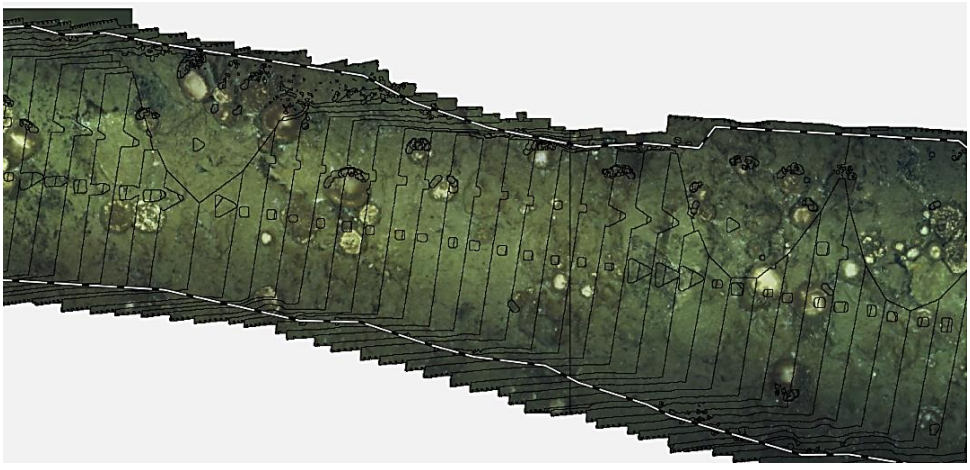

Figure 9-9: Manual and automatically l masked of the triple laser points.

The discussion of the reconstructed 3D model is a little controversy. In one hand the OFOBS dataset is not meant for underwater photogrammetry, thus whatever comes out should be

consider as a gift, while in the other hand the stills image camera is riche enough to provide better dataset by 10 times richer over a proper configuration and setting. Therefor there are two judgments for the imagery datasets: compare to the capability of the still imagery system, the provided dataset is not demanding but as unmanaged side products it is highly valuable.

9.3 Point Cloud Classification

The two tested software and algorithms for point cloud classification have advantages and disadvantages. The first result of the CSF algorithm in Agisoft needs more preparation and should start from the photo alignments until reaching segmentation via same environment. It is also not possible to apply different values in the same chunk and the environment of the software does not provide any tools or flexibility for user and the process of segmentation is extremely time consuming, but it is also possible to apply several iterations over the batch processing. On the contrary, the roughness estimation algorithm provided by CloudCompare, processes information faster and the software provides some flexible side tools to apply multiple variations in different area of the point cloud. This is considered a remarkable advantage as the resolution of the point cloud is subject to change by the FH and it is a needed multi-variation on the same dive.

Also, the result of the roughness estimation algorithm over the bathometry is not satisfactory as the bathymetry point cloud have some cuts and gaps in the outer side (figure 8-9) and the center line of the data shows some gap and noise in the nadir.

9.4 Sponge Detection

This sub-chapter tries to interpret the result and outputs of the *Spongdia* and find applicable reasons for their formation.

It is already a challenging task for the human eyes to interpret and define different classes for such diverse and complex information (appendix F and G) into several decent categories.

Therefore, the sponge detection methods of this study are mainly focuses on the several main aspects such as peaks, crown, and height of the sponges and a little experiment on geom-morphotypes segmentation derived from point cloud.

And at the end a little interpretation and analysis for the distribution and accumulation of the sponges will represent in regard to geomorphology aspect over the slope and depth.

Spongdia

The result of the visual-detection approach has a lot of ambiguity for the area covered with spicules accumulation in 2D orthophoto, therefore a supplementary step applied to enrich the

visually detected sponges by getting help from the detected peaks and DEM file. Then visually detected sponges and automatically detected peaks compared to gather in order to evaluate the peck detection.

NN = Nearest Neighbor A = Automatically M = Manually			Visually detected 80% - 100 %		Vissually Detected with aid nn peaks 50% - 80%		Sponge Spicules accumulation with aid nn peaks 30% - 50%		Total		SSA
	NN	Peaks #	Sponges #	Sponges %	Sponges #	Sponges %	Sponges #	Sponges %	Sponges #	Sponges %	
M			714		62		98		874		A
A	9	1636	514	72	56	8	94	96	664	76	
	13	1204	480	67	61	9	88	90	629	72	
	25	680	411	58	62	9	61	62	534	61	
	49	399	325	46	9	1	22	22	356	41	
M			236		15		9		260		B
A	25	259	151	64	15	6	8	89	174	67	
M			418		101		131		650		C
A	25	551	191	46	101	100	131	100	423	65	
M			319		26		73		418		D
A	25	368	253	79	26	100	73	100	352	84	
M			7		3		2		12		E
A		39	5	71	3	100	2	100	10	83	
M			30		5		4		39		F
A	25	39	18	60	5	100	4	100	27	69	

Table 9-3: Outputs of peak detection of *Spongdia* for all SSA in compare with visually detected with different certainty

Due to the high-resolution point cloud with minimum nose in SSA-A, different neighborhood values are applied within this area. The number of peck detected with NN value of 9 are higher compare to the other NN values and that's because the NN value 9 is detecting any small change on the surface as a sponges. This sensitivity is an advantage in the case of detecting small sponges in the flat areas or searching for geom-morphotypes, but also could be consider a disadvantage for complex situation or complex geom-morphotypes.

The detected peaks with neighborhood of 25, represents the most reasonable result in comparison with visually detected values. Therefore, for all other SSA the NN value of 25 is applied as the main value for peak detection.

The comparison of the most sponges which visually detected in SSA-A and Spongdia shows 76% overlap for NN9 and 72% for NN13.

In SSA-D and SSA-E few sponges are detected, therefore a precise evaluation is not easy to perform. In these areas the seabed is fairly flat and individual sponges are to calculate with the program. This also shows the height detection rate of 83 and 84%.

In general, finding a sponge in flat areas is easier for the algorithm hence the gridding is considered for overall slope of the area which the program is able to classify over the grids that are larger than the sponges. For a better detection single homogeneous areas can be selected and used for the calculation in the program Spongdia. Depending on the size of the sponges, individual NN values can be used for this purpose.

9.5 Analyses of Sponge distribution and discovered knowledge

The detected sponge crowns and peaks indicate that the distribution of the sponges in the sample area are not even and follows a pattern based on geomorphology of the seabed. It is obvious that the depth and slope play a major role in the distribution of the sponges.

The six distinct sub-sample areas are categorized by depth and slope. Two of these areas are relatively flat (Figure 9-12 A and D), but in different depths. One of them is at the top side of the central mount and the other one is 120m deeper at the saddle of the Central mount and Karasik peak. The given values in here are including sponge crowns and accumulation of the sponge spicules, but for simplicity is named “cap”.

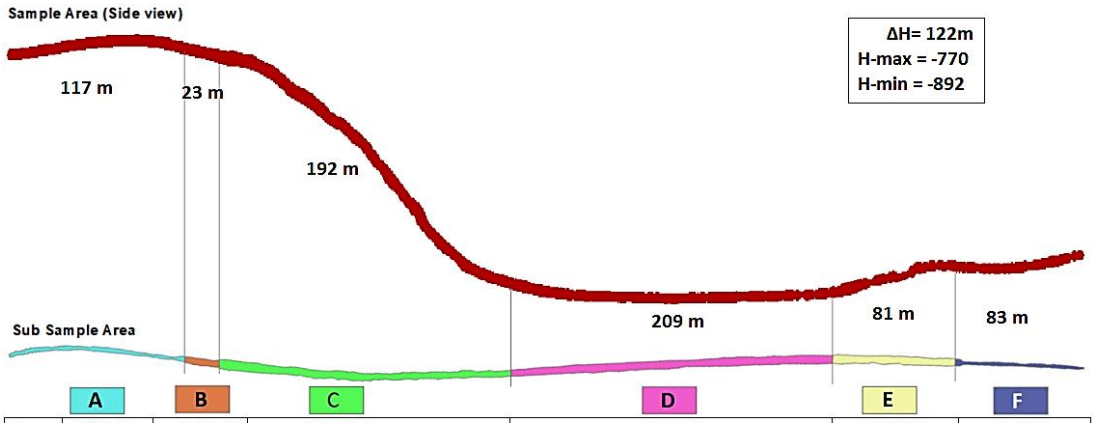

	A	B	C	D	E	F
Slope	0-10 %	0-10 %	25-50 %	0-5 %	11-20 %	0-10 %
Depth	-770 m -775 m	-770 m -775 m	-775 m -880 m	-880 m -890 m	-880 m -890 m	-870 m -880 m

Figure 9-10: The Six sub-sample are and the characteristic of them

The number of the detected caps in A is 874 which is more than two times the detected caps in D (418), while the length of the D (209m) is about two time bigger than the A (117m). Also, the area D is about 120m deeper than the area A, but both of the areas have relatively similar slope. The following picture is illustrating the distribution of the sponges in SSA-A and SSA-D.

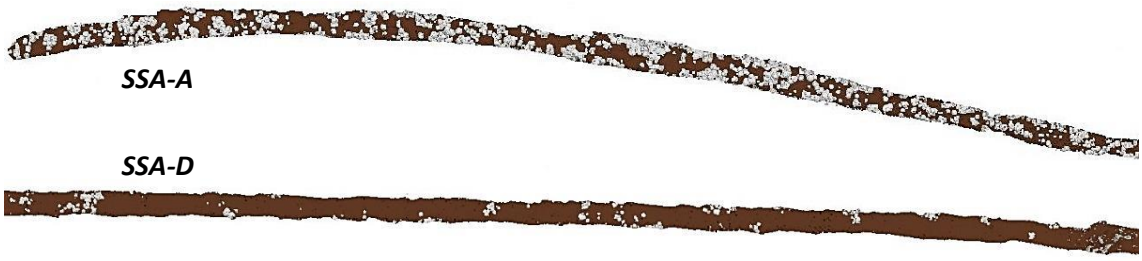

Figure 9-11: Comparison of the detected sponges crown in SSA-A and SSA-D

The comparison of the sponge distribution over SSA-A and SSA-D reveal this fact that the Geodia sponge population is about 4 times denser at the top of the central peak of the Karasik seamount compare to the 120 meters deeper area of the saddle, thus the depth could be mentioned as one of the plying rules of the sponges' distribution. However, for this conclusion the sedimentology and ocean current information are missing and are not put to account.

The SSA-B is the ultra-noisy area therefore *Spongdia* detected 260 peaks in this small 23 m area which definitely is not correct and should be consider as noise. The correct number of the sponges in this area is detectable in roughness method about 85 caps. It is worth mentioning the ultra-noise of this area is due to 3 major factors interfered here: 1) maximum FH of OFOBS during the dive within sample area reached here about 8.7 m 2) the along track slope of 25° and 3) side slope of 20°. The FH is the main reason of such a noise in the survey area. The following figures are showing the failed algorithm of SCF and the outputs of roughness estimation algorithm.

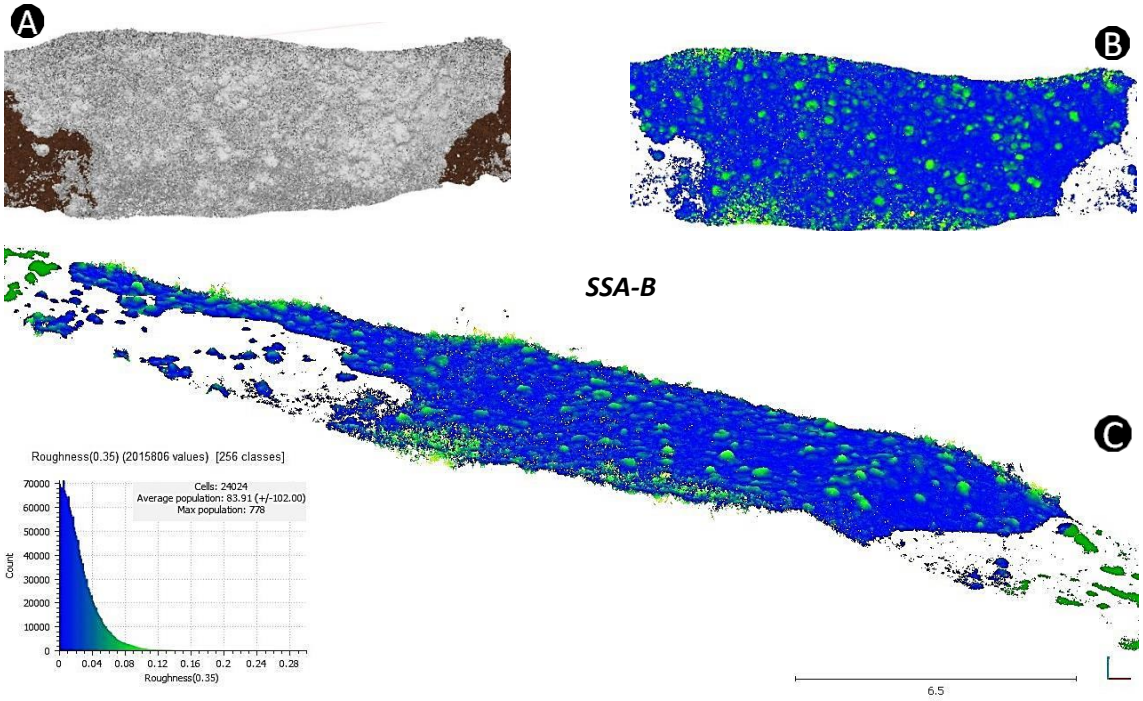

Figure 9-12: SSA_B the ultra-noisy area (A)Top view showing the failed attempt of classification by SCF algorithm over (B) top view of the same area, where 85 cap detected by roughness algorithm by kernel size of 35 cm (C) isometric view of the same area illustrating the along track slope and side slope

Another piece of knowledge which was achieved during this data mining is about the relationship of sponge distribution and seabed slopes. As the following graph shows the Geodia sponges are mostly settled at the seabed where the ground slope is smaller than 45° but hardly could be detected in the slope bigger than 45°. This pattern accrues in the slope area between the central peck and the saddle in SSA-C several times. The following picture is showing the side and top view of the same area where the sponges are settled at the slope smaller than 45°.

Figure 9-13: The influence of the slope over the Sponges distribution

One of the most noticeable phenomenon detected during the OFOBS dives, is the sponges tracks which could be observe once in q while in videos and still images. The initial hypothesis to describe this linear feature is the effect of slope and gravity to the sponges. But the analyses of the regional slope over the reconstructed 3D model reveal that in some areas the track of the sponge's path is perpendicular to the seabed slope. The following graph is showing the mention analysis.

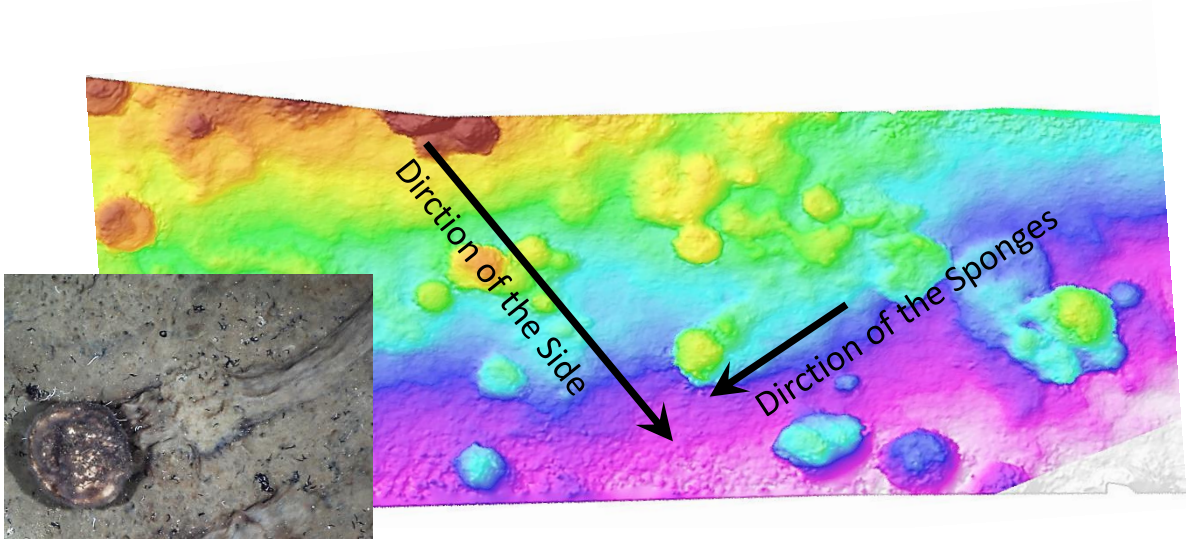

Figure 9-14: Sponge track in related to terrain slope.

9.6 Volume Estimation:

For the volume estimation, it must be considered that the size of the grid plays a major rule in the volume estimation accuracy therefore should be chosen as it fits the requirements in regard to the clouds resolution. The grid step sets for this calculation

The geometry area measured for this boundary A is as big as 287.626705 m^2 and this value calculated for the manually detected sponges has two following value

9.7 Analyst of the SSS Classification

The assumption of the intensity classification is that the sponges and rocks backscatter in higher intensity as the matter of higher exposure to the sonars waves compare to the flat seabed. Therefore 54% of the sample signatures are pointed to the high intensity areas to improve the detected sponges. The main problem of SSS data is in the outer boundary, as the image is not scaled, and the resolution gets worst in the outer side exponentially by the decreasing the incident angel of sonar ray.

The detected features in the corners are bigger than in the middle and in the nadir, there is no reliable information. The result of the segmentation with 20 and 25 nearest neighbors are quite similar.

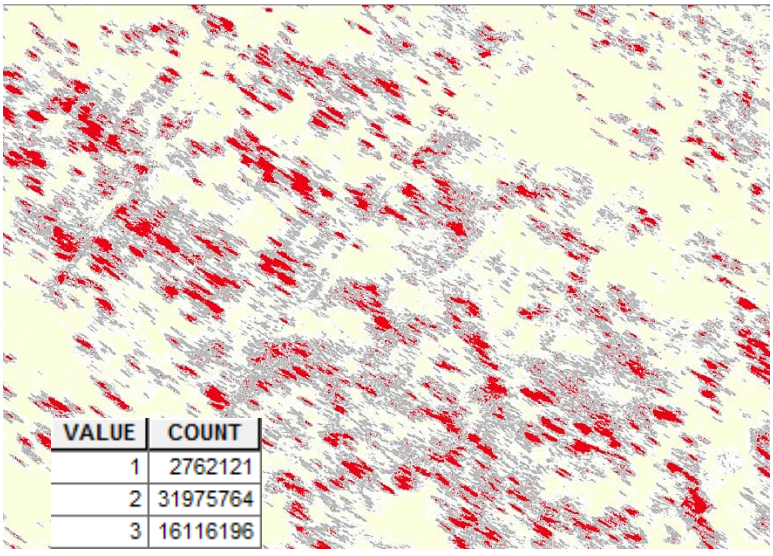

Figure 9-15: Result of the supervised classification by the 10 nearest neighbors.

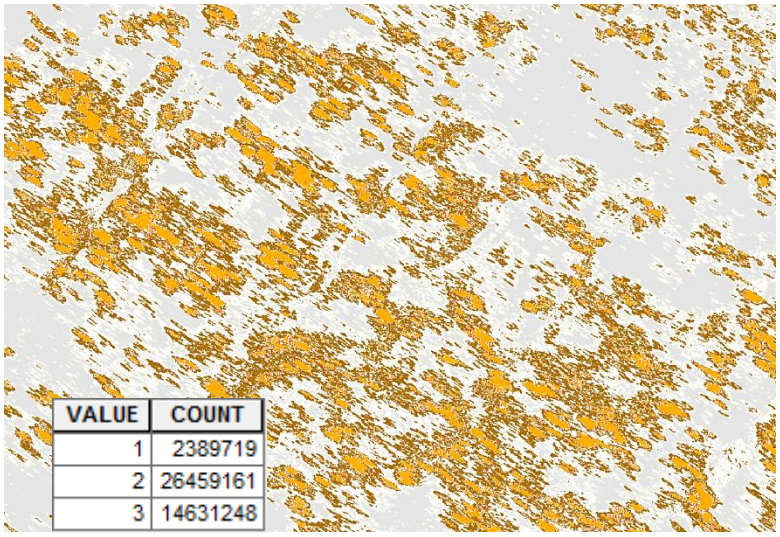

Figure 9-16: Result of the supervised classification by the 25 nearest neighbors.

9.8 Challenges and Choices

In some cases, a layer of spicules material covers the sponges completely or partly, which regardless to the material and consistency all these variations temporary named as sponge's crown, including yellowish bacteria accumulation or dead or dying sponges. This is one of the unsolved challenges for feature detection in point cloud as the designated method is designed for non-colored point cloud, which needs more complex workflow and programing.

The other challenge of current dataset is low color contrast of the sponges with the seabed background color. As the pattern recognition algorithms benefit from high color contrast within SfM and feature detection. In addition, the image quality of the frames is blurred in the corners and slightly smudged by the OFOBS motion, which could be solved by provided improvement recommendations in sub-chapter 9.7.2.

9.9 Further Possible Data Mining

The OFOBS footage shows a great variety of shapes of the same morphotypes with different geometries (Appendix E) and also some of the complexity regarding sponges' collision with other sponges of the same type or other members of the habitat community (Appendix F). Therefore, a local catalog is provided from the video and stills camera in order to prepare an unofficial catalog of the sponges' geom-morphotypes in the region which are the essential key for data interpretation, feature detection and algorithm training. Due to the computer feature detection processing, there should be a combination of raster and geometry classification approach for sponges' classification with some positive and negative samples.

Therefore, during the data processing a little experiment conducted in order to classify the geom-morphotypes of the sponges. The object-based image analysis (OBIA) and object-based point cloud analysis (OBPA) employed. OBIA and OBPA are advanced segmentation methods based on neural network. For this classification three individual datasets employed: orthophoto mosaic, DEM. and cleaned dense cloud. For these process the trial version of *eCognition Developer* employed (eCognition (Ed.), 2017).

Although the work flow was not very straightforward initially and some obstacles appeared regarding the data capability limitation for free version and memory overflow, but the multi-segmentation algorithms succeed to detect sponges crown in low color contrast situation.

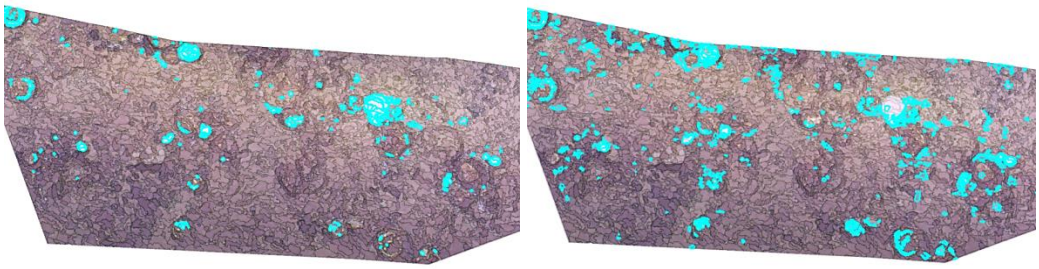

Figure 9-17: Output of multi-segmentation for sponge detection by different setting.

Although the resolution of the SfM products are not good enough for more detailed data mining but the experiment shows that with a better point cloud and orthomosaic the haar-like cascade algorithm could distinguish the geom-morphotypes. The following pictures are illustrating the low resolution orthophoto of a concave crown sponges (Appendix F) recognized and classified by two different variation setting

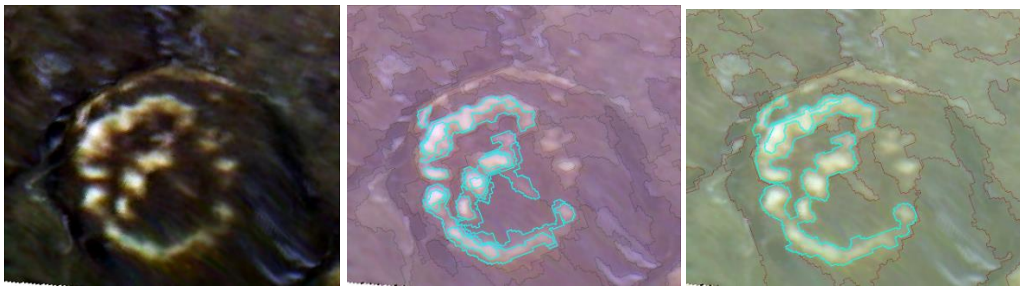

Figure 9-18: Outputs of geom-morphotypes segmentation by eCognition. (Left) a concave crown sponge on orthophoto, (middle and right) result of the segmentation by different variable sets.

The other possible improvement for geom-morphotypes segmentation could be applied over the *Spongdia*, by clustering the neighborhood peaks which have similar height as concave crown or more geometry analysis.

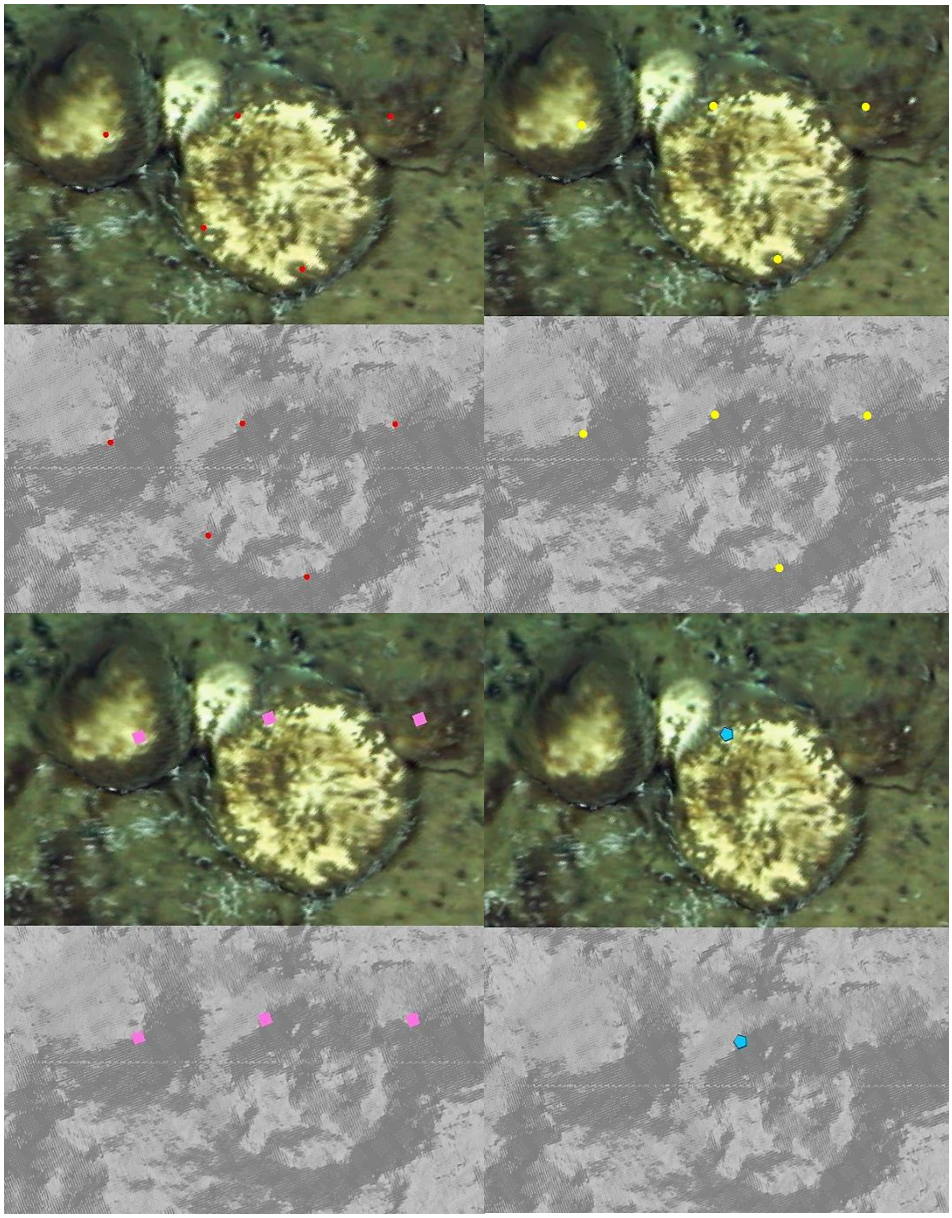

Figure 9-19: Results of Spongdia peak NN: (Upper left) NN9, (upper right) NN13, (lower left) NN25, (lower right) NN45.

9.10 Possible Improvements

The exploited OFOBS was not originally designed for underwater Photogrammetry purposes but mainly as observation and the bathymetry. The idea of using OFOBS dataset developed during post processing phase of PS101 with the master theses of Dreutter (2017). Therefore, in this section some recommendation will present with intention to improvement the data capability and quality of optical datasets of the OFOBS. These adaptations and modifications will convert the OFOBS to an underwater photogrammetry platform with bathymetry extension.

Some of these modifications have extra cost and a little impact while some improve the outcome exponentially with no cost.

9.10.1 Data Acquisition Improvement

It is possible to improve the capability and quality of the 3D model by ~10 times better via the camera configuration time setting. The automatically shooting interval of still camera has to be shortening to a tailored value which provides appropriate overlaps on a sequence of the 6k images. These images are ~11 times richer in pixel number and are premier in hue and color balance, which are not only improve the GSD but also provide more reliability and accuracy for pattern recognition result. It also will escape the errors and uncertainty of the video frame timestamping interpolation, as these images already have the time and position information embedded in their metadata. Therefor by improving the initial and fundamental dataset the noise and ambiguity will reduce exponentially.

9.10.2 Further Hardware Improvements

There are many possibilities to improve the optical dataset of OFOBS by utilizing extra hardware and extension, which some of them will improve the bathometry dataset as well. Also, there are some hardware modifications for the cameras mounting which needs detailed analysis.

In addition to the camera resolution which play the major role in the image and derivatives quality there are still many technical and strategically details which could boost the outcomes noteworthy directly and indirectly.

In order to extract sharper still images and video there are several compensation methods and techniques available from which already employed in film industry and smartphones, in which they meant to reduce blurring effected by the motion of an imaging device within exposure. The concept of Image stabilization has Hardware or Software or mixed approach. A usual compensating hardware which mostly employed in drones and UAVs is Gimbal.

The gimbals could be utilized either as camera stabilization systems or for whole OFOBS mounting system.

The current camera installation of OFOBS could be categorized as a passive photogrammetry, while in the case of installing the second parallel stills camera, the system will turn to a stereo photogrammetry system or active photogrammetry system (Bianco et al., 2011). The benefit of the active system is vary: 1) the active system provides a wider range of the data sets specially if there is more than 2 camera installed in the parallel arms, also the stereo shooting could extend the OFOBS for the simultaneous localization and mapping (SLAM) system.

With a wider imagery system, the result of SfM will expand to the area where the SfM dataset and bathymetry point will have overlap. Thus, the feature matching and resampling methods will provide a seamless high resolution wide range dataset.

10 Conclusion

This work has address the novel developed workflow of spatial data mining for habitat mapping on several datasets collected in the harsh condition of the Arctic Ocean by the Ocean Floor Observation and Bathymetry System (OFOBS). The rationale of this work was based on multi-sensor dataset with different type, quality, capability and uncertainty which were employed for feature detection. The previous chapters have present the capability of various computer vison and pattern recognition algorithms excavating to the different geospatial datasets, searching defined target object (Geodia sponges) in order to categorizing them in several classes.

Although the main focus of spatial data mining was on the optical sensor dataset, some feature detection algorithms were applied over sonar datasets in order to show the capability of the data in comparison to the optical datasets.

The structure from the motion (SfM) algorithm recruited for reconstructing the 3D model, and then the mapping product of the 3D model were exported for further data mining. The 3D model inherits its quality mostly from the low-resolution video frames, as 95% of the images involved in the reconstructed model come from the low-quality video camera.

In this study area two type of measurements are considered: 3D dimensions of the detected objects and 3D position of the survey area. Regarding the environment property and frequent disconnection of the USBL, the underwater positioning in the global coordinate frame still remains a mystery in the range of several meters in the mean of incomputable total propagation uncertainty (TPU). However, the local frame and the measurement of the 3D dimension of the object is evaluated locally bay triple projected laser dots in the local frame were achieved by 4% (2 centimeter in 50-centimeter reference distance) centimeters (chapter 9.1).

The enormous capability of the OFOBS dataset for habitat mapping was demonstrated in chapter 7 and 8 by implementing several feature detection algorithms for imagery datasets and sonar datasets. The imagery datasets provide higher resolution feature detection but in a limited narrow corridor of the field of view (FOV) of the camera, while the bathymetry is covering a wider area but there are lots of ambiguity in the type and size of the detected objects, especially in the outer range of the side scan sonar data and bathometry. Also, it is not possible to detect any object in nadir point of sonar by several meters due to the property and installation of the sonar system, thus it is impossible to extend and resample the results of the imagery dataset to the sonar dataset with acceptable assumptions. The solution for this issue is provided in the recommendations chapter.

There are several challenges within the datasets which were discussed in chapter 9.7. Mainly there are the two physical factors recognized which affect the OFOBs data quality: one of them is a sudden change in the slope which caused imbalanced light absorption in a single picture and the other one is the flight height (FH) of the OFOBS as is described in ultra the Ultra-noisy area. As it discussed in the previous chapter the FH has more influents on the resolution and quality of the point cloud than the slope. Also, there low color contrast of the seabed captured in video camera is an unsolvable problem. In addition, the complexity and geom-morphotypes diversity of the sponges (Appendix F and G) are the two serious challenges for the peak detection algorithms which partly remained unsolved.

The interpretation of the distribution of the sponges attempted in chapter 9.4 by comparing the two relatively flat areas shows the capability and advantage of the provided methods in 3D datasets. This kind of interpretation could not be achieved in 2D feature detection over orthophoto images.

11 References

Agisoft (Ed.) (2016): *Agisoft PhotoScan User Manual: Professional Edition. Version 1.2*. Online: http://www.agisoft.com/pdf/photoscan-pro_1_2_en.pdf (Accessed: 2016-11-02).

Altman, N. S. (1992): *An Introduction to Kernel and Nearest-Neighbor Nonparametric Regression*. The American Statistician, 46(3), 175-185. doi:10.1080/00031305.1992.10475879

Ana Fred, M. D. M., Gabriella Sanniti di Baja (2016): *Pattern Recognition Applications and Methods*, Springer.

AWI (2017): *Polarstern*. Online: https://www.awi.de/en/expedition/ships/polarstern.html.

AWI, P. Gerchow & FIELAX (2018, Feb 07, 2018 21:03): *FS-Polarstern Sientific Devices* v.60. Online: https://spaces.awi.de/confluence/pages/viewpage.action?pageId=173932621.

Bianco, G., A. Gallo, F. Bruno & M. Muzzupappa (2011): *A comparison between active and passive techniques for underwater 3D applications*. Int. Arch. Photogramm. Remote Sens. Spat. Inf. Sci, 34, 357-363.

Boetius, A. & A. Purser (2017): *The Expedition PS101 of the Research Vessel POLARSTERN to the Arctic Ocean in 2016*. *Berichte zur Polar- und Meeresforschung = Reports on Polar and Marine Research*. Bremerhaven, Alfred Wegener Institute for Polar and Marine Research, 706, 230 p. doi:10.2312/BzPM_0706_2017

C.J. de Jong, G. L., S. Skone, I.A. Elema (2010): *Hydrography*. Netherlands, VSSD & Delft University Press.

Carbonneau, P. E. & J. T. Dietrich (2017): *Cost-effective non-metric photogrammetry from consumer-grade sUAS: implications for direct georeferencing of structure from motion photogrammetry*. Earth Surface Processes and Landforms, 42(3), 473-486. doi:doi:10.1002/esp.4012

Caris (Ed.) (2016): *CARIS HIPS and SIPS Documentaion (Reference Guide)*. USA, Teledyne CARIS, Inc., 10.2.2.

Clinton, B. (2000): *Improving the Civilian Global Positioning System (GPS)* O. o. t. P. Secretary. USA, Press Release of The White House.

Cochran, J. R., G. J. Kurras, M. H. Edwards & B. J. Coakley (2003): *The Gakkel Ridge: Bathymetry, gravity anomalies, and crustal accretion at extremely slow spreading rates*. Journal of Geophysical Research: Solid Earth, 108(B2). doi:10.1029/2002JB001830

Dorschel, B. & L. Jensen (2017): *Swath sonar bathymetry during POLARSTERN cruise PS101 (ARK-XXX/3) with links to multibeam raw data files*. PANGAEA. doi:10.1594/PANGAEA.871047

Dreutter, S. (2017): *Multisensor Microbathymetric Habitat Mapping with a Deep-Towed Ocean Floor Observation and Bathymetry System (OFOBS)*. HafenCity University Hamburg, 125. doi:10013/epic.51433

Duda, R. O., P. E. Hart & D. G. Stork (2001): *Pattern Classification*. New York, John Wiley & Sons.

eCognition (Ed.) (2017): *eCognition Developer*

e. C. Developer.v8.7.1905, Trimble

Ecological Society of America (1931): *Ecological monographs : a quarterly journal for all phases of ecology*. Ecological monographs : a quarterly journal for all phases of ecology.

El Naggar, S. E. D. (2006): *Handbuch FS POLARSTERN*. E. Fahrbach, AWI, 84. doi:10013/epic.26892

Esri (Ed.) (2017): *ArcGIS Spatial Analyst extension*. USA, Esri Inc., 10.4.1.

Fang, J.-Y. & Z. M. Wang (2001): *Forest biomass estimation at regional and global levels, with special reference to China's forest biomass*. Ecological Research, 16(3), 587-592. doi:10.1046/j.1440-1703.2001.00419.x

Fekete, K. S., P. (2008): *Qualification of close range photogrammetry cameras by average image coordinates rms error vs. object distance function*.

Freeman, H. & R. Shapira (1975): *Determining the minimum-area encasing rectangle for an arbitrary closed curve*. Commun. ACM, 18(7), 409-413. doi:10.1145/360881.360919

Fridtjof Nansen Institute (1999): *Bathymetrical Chart of Northern Polar Seas by Dr Fridtjof Nansen*. Online: https://www.fni.no/getfile.php/132474/Bilder/Polh%C3%B8gda/Nansen_bathymetrical_map_arctic.jpg (Accessed: 2017-10-30).

GPL-software (Ed.) (2017): *CloudCompare*.

GSHHG (2017): *Global Self-consistent, Hierarchical, High-resolution Geography Database* W. V. S. (WVS)., C. W. D. B. I. (WDBII). and A. o. t. C. (AC). University of Hawai'i, Honolulu.

Harris, P. T. & E. K. Baker (2011): *Seafloor Geomorphology as Benthic Habitat: GeoHAB Atlas of Seafloor Geomorphic Features and Benthic Habitats*, Elsevier Science.

Heipke, C. (2003): *Photogrammetrie & Fernerkundung-vom Elektronenmikroskop bis zur Planetenbeobachtung*. Photogrammetrie Fernerkundung Geoinformation, 165-180.

Hosseinie Abrischimie, R. (2017): *Durchführung der Waldinventarisierung mit Hilfe von UAV-basierter Sensorik*. Hamburg, HafenCity University Hamburg, 110.

HYPACK (Ed.) (2016): *a Xylem brand and part of YSI, software for the hydrographic and dredging industry since 1984*. *HYPACK® SURVEY*. v. 13. USA.

International Hydrographic Organization (IHO) (Ed.) (2008): *IHO Standards for Hydrographic Surveys*. *Special Publication N° 44*. Monaco, International Hydrographic Bureau, 5th edition, February 2008.

IOC-IHO GEBCO SCUFN-XV1/3 (2003): *Sixteenth meeting of the GEBCO Sub-committee on Undersea Feature Name (SCUFN)*. *SCUFN-XV1/3*. 16th. Monaco, International Hydrographic Bureau, INTERGOVERNMENTAL OCEANOGRAPHIC COMMISSION (of UNESCO), 16th, 54.

IOC-IHO GEBCO SCUFN-XV/3 (2002): *Fifteenth meeting of the GEBCO Sub-committee on Undersea Feature Name (SCUFN)*. *SCUFN-XV/3*. 15th. Monaco, International Hydrographic Bureau, INTERGOVERNMENTAL OCEANOGRAPHIC COMMISSION (of UNESCO), 15th, 81.

iXBlue-SAS (2016): *HYDRINS Product Specification*. *MU–HYDRINS–AN–012 Ed. A – February 2016*. i.-S. Company.

iXBlue (Ed.) (2011): *USBL-BOX – Positioning System – User Guide*. Online: http://www.igp.de/manuals/MU_USBLBOX_AN_001_B.pdf (Accessed: 2016-11-15).

iXBlue (Ed.) (2014): *Phins 6000 – FOG-based high-performance subsea Inertial Navigation System for deep water*. Technical Specifications. Online: https://www.ixblue.com/sites/default/files/downloads/ixblue-ps-phins_6000-02-2014-web.pdf (Accessed: 2016-09-02).

IXSEA (Ed.) (2010): *PHINS 6000 – User Guide*. (Supplied with hardware).

Jakobsson, M., L. Mayer, B. Coakley, J. A. Dowdeswell, S. Forbes, B. Fridman, H. Hodnesdal, R. Noormets, R. Pedersen, M. Rebesco, H. W. Schenke, Y. Zarayskaya, D. Accettella, A. Armstrong, R. M. Anderson, P. Bienhoff, A. Camerlenghi, I. Church, M. Edwards, J. V. Gardner, J. K. Hall, B. Hell, O. Hestvik, Y. Kristoffersen, C. Marcussen, R. Mohammad, D. Mosher, S. V. Nghiem, M. T. Pedrosa, P. G. Travaglini & P. Weatherall (2012): *The International Bathymetric Chart of the Arctic Ocean (IBCAO) Version 3.0*. Geophysical Research Letters, 39(12). doi:10.1029/2012GL052219

Jensen, A. B. & J.-P. Sicard (2010): *Challenges for Positoning and Navigation in the Arctic*. Coordinates: A resource on positioning, navigation, and beyond.

Kale, K. V., S. C. Mehrotra & R. R. Manza (2010): *Computer Vision and Information Technology: Advances and Applications*, I.K. International Publishing House Pvt. Limited.

Keegan, B. F., P. J. S. Boaden & P. O. Ceidigh (1977): *Biology of Benthic Organism*.

Leachtenauer, J. C. & R. G. Driggers (2001): *Surveillance and Reconnaissance Imaging Systems: Modeling and Performance Prediction*, Artech House.

Lowe, D. G. (2004): *Distinctive Image Features from Scale-Invariant Keypoints*. International Journal of Computer Vision, 60(2), 91-110. doi:10.1023/b:Visi.0000029664.99615.94

Luhmann, T., S. Robson, S. Kyle & J. Boehm (2013): *Close-Range Photogrammetry and 3D Imaging*, De Gruyter.

Luhmann, T., S. Robson, S. Kyle & I. Harley (2007): *Close Range Photogrammetry: Principles, Techniques and Applications*, Wiley.

Lurton, X. (2002): *An Introduction to Underwater Acoustics: Principles and Applications*, Springer.

Mikhail, E. M., J. S. Bethel & J. C. McGlone (2001): *Introduction to modern photogrammetry*. New York.

NOAA (2017): *Benthic habitat map*. Online: https://oceanservice.noaa.gov/facts/benthic.html.

Overath&Sand-Surveyors (2016): *Alignment Survey Report - RV Polarstern - Survey Period: June 2016. Revision 3*. J. 2016. Reederei F. Laeisz GmbH / Bremerhaven, Revision 3, 105.

PANGAEA-PS101-Datasets (2016): *PS101 Dataset on PANGAEA warehouse*.

Purser, A., Y. Marcon, S. Dreutter, U. Hoge, B. Sablotny, L. Hehemann, J. Lemburg, B. Dorschel, H. Biebow & A. Boetius (2018): *Ocean Floor Observation and Bathymetry System (OFOBS): A new Towed Camera/Sonar System for Deep-Sea Habitat Surveys*. IEEE Journal of Oceanic Engineering, PP(99), 1-13. doi:10.1109/JOE.2018.2794095

Ravindranath, N. H. & D. O. Hall (1995): *Biomass, energy and environment: a developing country perspective from India*, Oxford University Press.

Reid, T. W., Todd/ Blanch, Juan /Enge, Per (2015): *GNSS Integrity in the Arctic. The 28th International Technical Meeting of the Satellite Division of The Institute of Navigation (ION GNSS+ 2015)*. Tampa, Florida.

Ripley, B. D. (2007): *Pattern recognition and neural networks*, Cambridge university press.

Sablatnig, R. (2009): *Einführung in Visual Computing (EVC) Image Processing & Computer Vision. PhD*. Wien, TU Wien.

Samsudin, S. A. & R. C. Hasan (2017): *Assessment of Multibeam Backscatter Texture Analysis for Seafloor Sediment Classification*. ISPRS-International Archives of the Photogrammetry, Remote Sensing and Spatial Information Sciences, 177-183.

Sassi, R. J. (2012): *An hybrid architecture for clusters analysis: rough setstheory and self-organizing map artificial neural network*. Pesquisa Operacional, 32, 139-164.

Seaice.Universität.Bremen (2017, 2018): *Sea Ice Remote sensing*. Online: https://seaice.uni-bremen.de/ (Accessed: 2016).

Sebe, N. (2005): *Machine Learning in Computer Vision*, Springer Netherlands.

Slabon, P. (2011): *Kalibrierung und Genauigkeitsuntersuchungen zur neuen Hydrosweep DS-3 Anlage auf FS Polarstern*. HafenCity Universität Hamburg, 126.

Slabon, P. (2014): *Analysis of the sedimentary and topographical structure of the Falkland Plateau using new Hydrosweep DS3 and Parasound data from RV Polarstern Expedition ANT-XXIX/5*.

Sohn, R. A., C. Willis, S. Humphris, T. M. Shank, H. Singh, H. N. Edmonds, C. Kunz, U. Hedman, E. Helmke, M. Jakuba, B. Liljebladh, J. Linder, C. Murphy, K.-i. Nakamura, T. Sato, V. Schlindwein, C. Stranne, M. Tausenfreund, L. Upchurch, P. Winsor, M. Jakobsson & A. Soule (2008): *Explosive volcanism on the ultraslow-spreading Gakkel ridge, Arctic Ocean*. Nature, 453, 1236. doi:10.1038/nature07075

Steele, J. H., S. A. Thorpe & K. K. Turekian (2009): *Elements of Physical Oceanography: A derivative of the Encyclopedia of Ocean Sciences*, Elsevier Science.

TeledyneRESON (2010): *HydroSweep DS Deep-Sea Multibeam Echosounder*. DS3. doi:PLD16537-1

Thiede, J. (2002): *POLARSTERN ARKTIS XVII/2 : Cruise Report: AMORE 2001 (Arctic Mid-Ocean Ridge Expedition)*. Bremerhaven, Alfred Wegener Institute for Polar and Marine Research, 421. doi:10013/epic.10426

Venzke, J.-F. (1990): *The 1869/70 German North Polar Expeditio (Arctic profiles)*. ARCTIC, 43, 83-85.

WATI, G. N., J. B. GELDOF & N. SEUBE (2016): *Error budget analysis for hydrographic survey systems; implementation on an inspection campaign of pipelines by an AUV*. INTERNATIONAL HYDROGRAPHIC REVIEW, No.15(Publication P-1).

Weber, J. (1983): *Maps of the Arctic Basin sea floor: a history of bathymetry and its interpretation*. ARCTIC, 121-142.

Wolff, K., C. Kim, H. Zimmer, C. Schroers, M. Botsch, O. Sorkine-Hornung & A. Sorkine-Hornung (2016): *Point Cloud Noise and Outlier Removal for Image-Based 3D Reconstruction*. 2016 Fourth International Conference on 3D Vision (3DV), 118-127. doi:10.1109/3DV.2016.20

Zhang, W., J. Qi, P. Wan, H. Wang, D. Xie, X. Wang & G. Yan (2016): *An Easy-to-Use Airborne LiDAR Data Filtering Method Based on Cloth Simulation*.

The data used in this thesis is available through the bathymetry group and the PANGAEA archive of the Alfred-Wegener-Institute, Helmholtz Centre for Polar and Marine Research (AWI). To access the data please contact the following email: infobathy@awi.de.

Appendix A (RV Polarstern)

RV Polarstern Sketch with vessel survey reference points and fixed sensors position

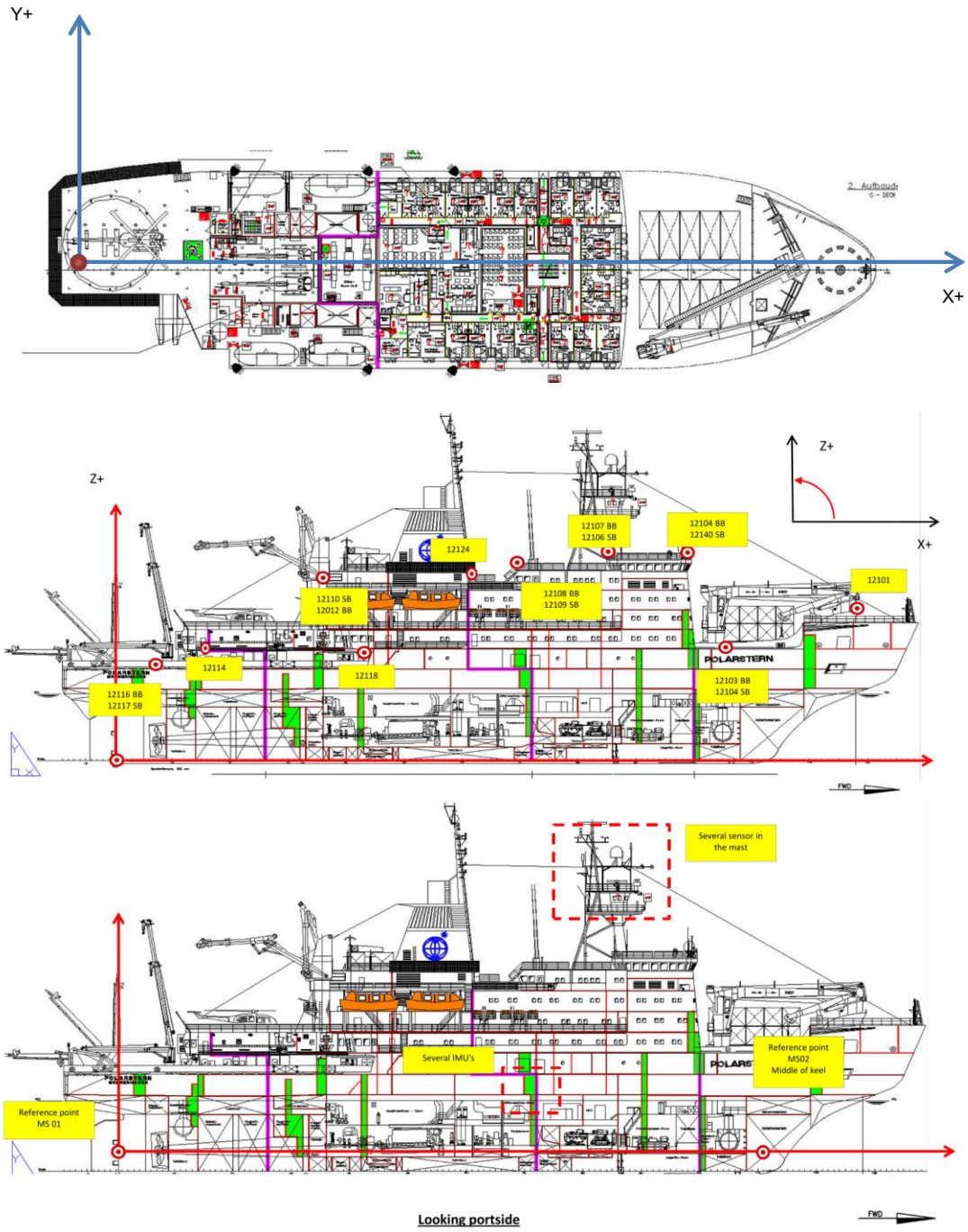

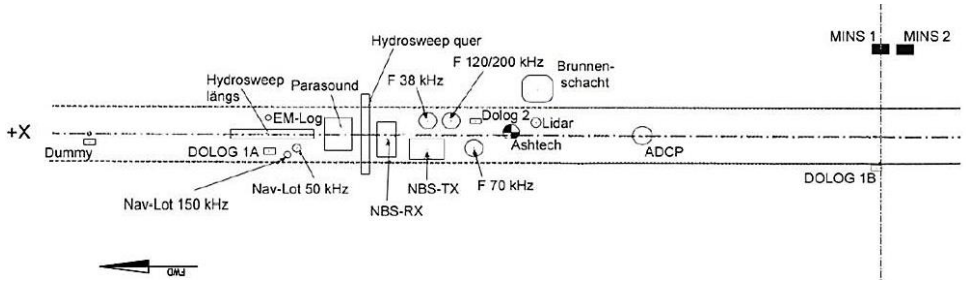
Hydrosweep quer
MINS 1
MINS 2
F 120/200 kHz
Brunnen-
schacht
Hydrosweep
längs
Parasound
F 38 kHz
EM-Log
Dolog 2
Lidar
+X
Dummy
DOLOG 1A
Ashtech
ADCP
Nav-Lot 50 kHz
NBS-TX
F 70 kHz
DOLOG 1B
Nav-Lot 150 kHz
NBS-RX

Appendix B (OFOBS Instruments Sketch)

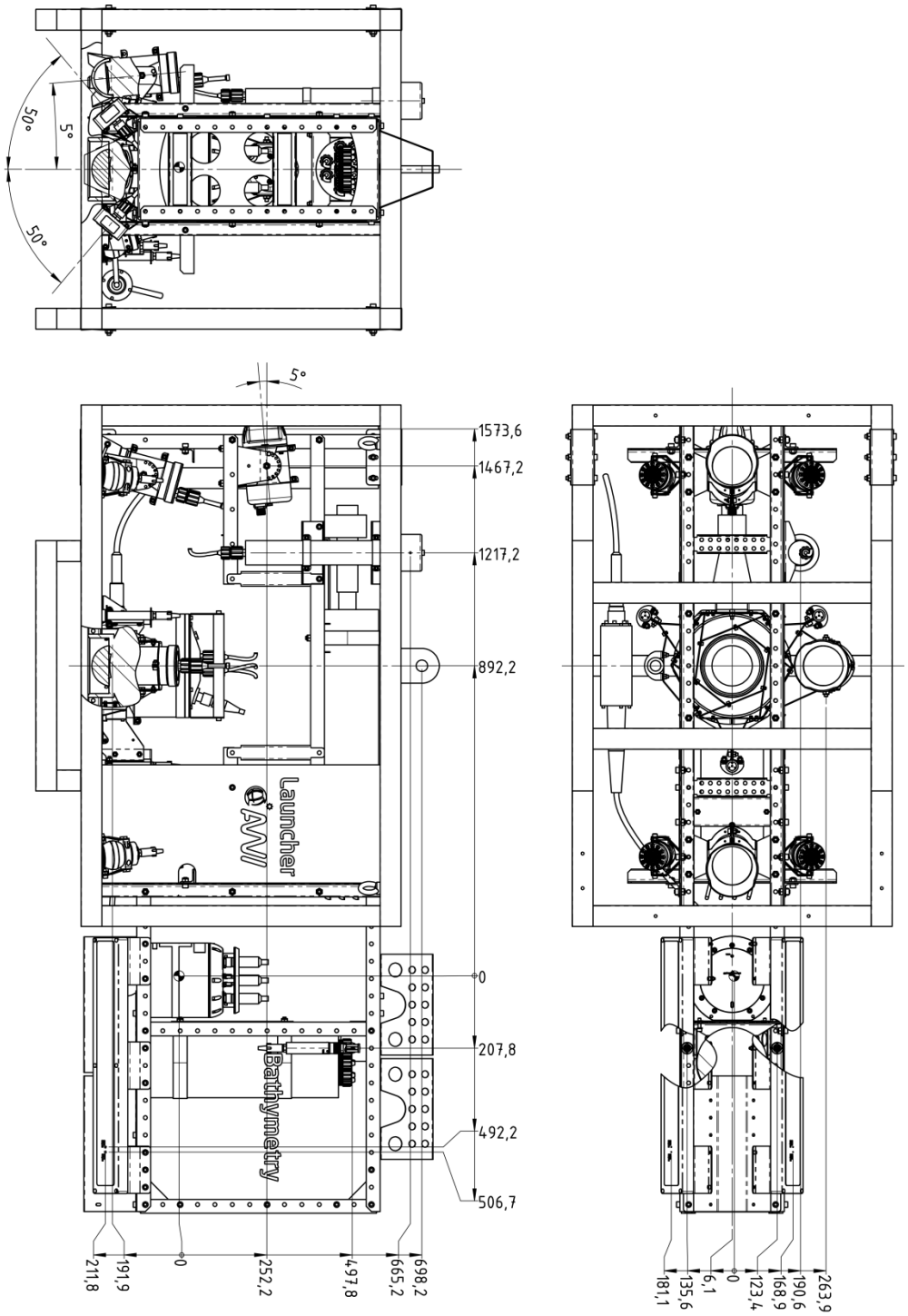

Appendix C (Maps)

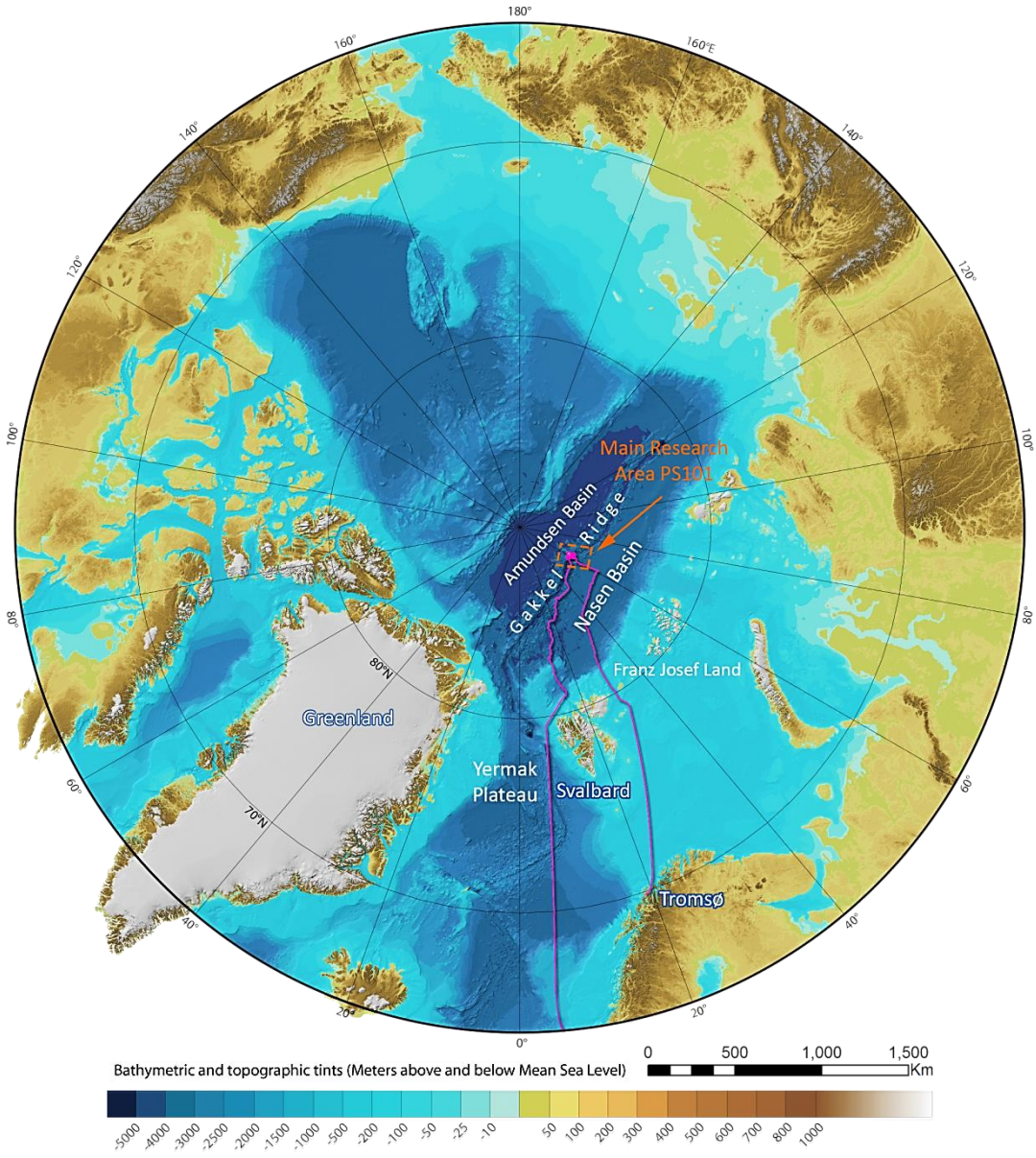

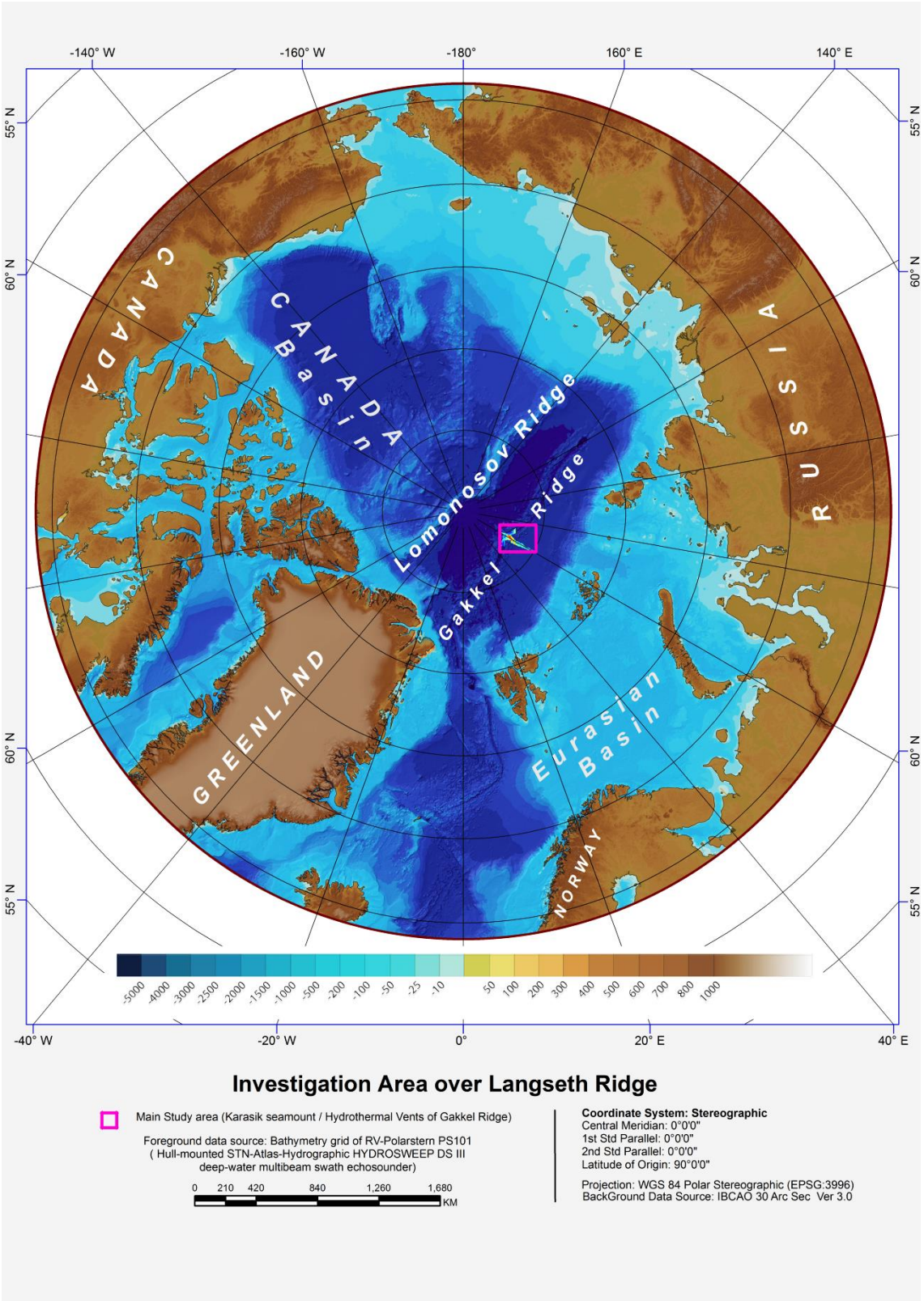
-140° W
-160° W
-180°
160° E
140° E
55° N
60° N
CANADA
CANADA Basin
Lomonosov Ridge
Gakkel Ridge
RUSSIA
GREENLAND
Eurasian Basin
NORWAY
-5000
-4000
-3000
-2500
-2000
-1500
-1000
-500
-200
-100
-50
-25
-10
50
100
200
300
400
500
600
700
800
1000
-40° W
-20° W
0°
20° E
40° E
Investigation Area over Langseth Ridge
Main Study area (Karasik seamount / Hydrothermal Vents of Gakkel Ridge)
Foreground data source: Bathymetry grid of RV-Polarstern PS101
(Hull-mounted STN-Atlas-Hydrographic HYDROSWEEP DS III
deep-water multibeam swath echosounder)
0 210 420 840 1,260 1,680
KM
Coordinate System: Stereographic
Central Meridian: 0°0'0"
1st Std Parallel: 0°0'0"
2nd Std Parallel: 0°0'0"
Latitude of Origin: 90°0'0"
Projection: WGS 84 Polar Stereographic (EPSG:3996)
BackGround Data Source: IBCAO 30 Arc Sec Ver 3.0

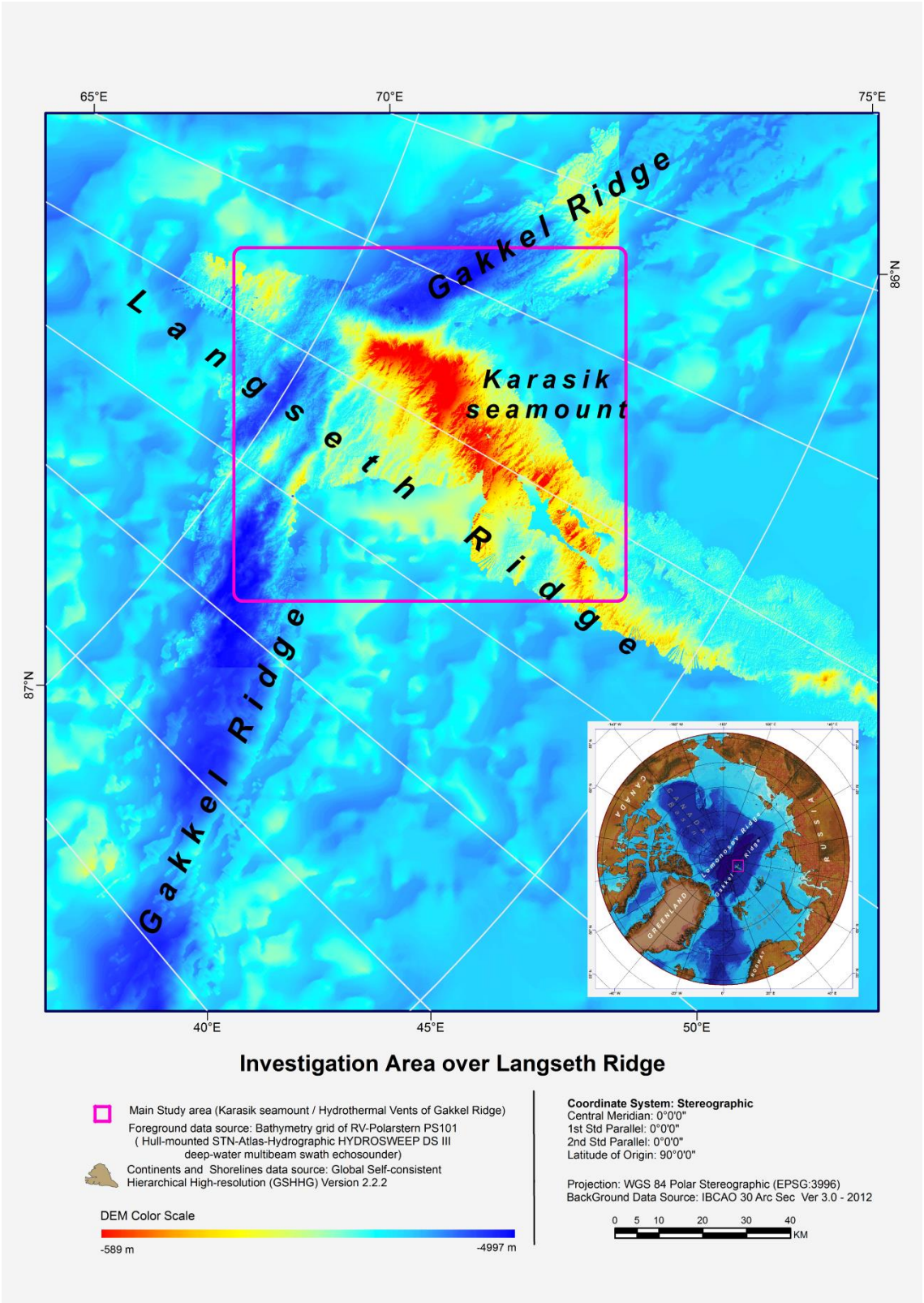
65°E
70°E
75°E
86°N
87°N
40°E
45°E
50°E
Gakkel Ridge
Langseth Ridge
Karasik seamount
Gakkel Ridge
Investigation Area over Langseth Ridge
Main Study area (Karasik seamount / Hydrothermal Vents of Gakkel Ridge)
Foreground data source: Bathymetry grid of RV-Polarstern PS101
(Hull-mounted STN-Atlas-Hydrographic HYDROSWEEP DS III
deep-water multibeam swath echosounder)
Continents and Shorelines data source: Global Self-consistent
Hierarchical High-resolution (GSHHG) Version 2.2.2
DEM Color Scale
-589 m
-4997 m
Coordinate System: Stereographic
Central Meridian: 0°0'0"
1st Std Parallel: 0°0'0"
2nd Std Parallel: 0°0'0"
Latitude of Origin: 90°0'0"
Projection: WGS 84 Polar Stereographic (EPSG:3996)
BackGround Data Source: IBCAO 30 Arc Sec Ver 3.0 - 2012
0 5 10 20 30 40
KM

Appendix D (Volume estimation tables)

Ground source: DTM Cloud Empty cell value: Interpolate Ceil Source: DSM Cloud Grid step: 0.05 Grid Size: 2160 x 931 Projected dir. : Z Cell height: Average	Ground source: DTM Cloud Empty cell value: Interpolate Ceil Source: DSM Cloud Grid step: 0.1 Grid Size: 1080 x 466 Projected dir. : Z Cell height: Average
Volume: 23.982 Surface: 769.940 ---------- Added volume: (+)24.394 Removed volume: (-)0.412 ---------- Matching cells: 99.6% Non-matching cells: ground = 0.0% ceil = 0.4% Average neighbors per cell: 8.0 / 8.0	Volume: 35.087 Surface: 769.560 ---------- Added volume: (+)35.096 Removed volume: (-)0.008 ---------- Matching cells: 99.6% Non-matching cells: ground = 0.0% ceil = 0.4% Average neighbors per cell: 7.9 / 8.0
Ground source: DTM Cloud Empty cell value: Interpolate Ceil Source: DSM Cloud Grid step: 0.25 Grid Size: 433 x 187 Projected dir. : Z Cell height: Average	Ground source: DTM Cloud Empty cell value: Interpolate Ceil Source: DSM Cloud Grid step: 0.5 Grid Size: 217 x 94 Projected dir. : Z Cell height: Average
Volume: 14.560 Surface: 778.938 ---------- Added volume: (+)14.562 Removed volume: (-)0.003 ---------- Matching cells: 99.6% Non-matching cells: ground = 0.0% ceil = 0.4% Average neighbors per cell: 7.8 / 8.0	Volume: 18.748 Surface: 801.750 ---------- Added volume: (+)18.759 Removed volume: (-)0.011 ---------- Matching cells: 98.7% Non-matching cells: ground = 0.0% ceil = 1.3% Average neighbors per cell: 7.5 / 8.0

Appendix E (Supervised Clustered by Signatures)

```
# Signatures Produced by Class Sig from
#    Class-Grid __1000002
#    and Stack __1000001
#    Number of selected grids          4
#    Layer-Number    Band-name
/*          1      PS101_169_A_SSL_3cm_RENAV_RGB.tif\Band_1
/*          2      PS101_169_A_SSL_3cm_RENAV_RGB.tif\Band_2
/*          3      PS101_169_A_SSL_3cm_RENAV_RGB.tif\Band_3
/*          4      PS101_169_A_SSL_3cm_RENAV_RGB.tif\Band_4
#  Type   Number of Classes   Number of Layers    Number of Parametric Layers
   1           3              4                    4
# ================================================================
#  Class ID     Number of Cells    Class Name
      1            215        1
# Layers           1           2           3           4
# Means              2.543070e+002 2.474465e+002 2.348233e+002 2.550000e+002
# Covariance
   1      3.994271e+001 8.325949e+001 1.634984e+002 0.000000e+000
   2      8.325949e+001 3.908464e+002 9.588830e+002 0.000000e+000
   3      1.634984e+002 9.588830e+002 2.427455e+003 0.000000e+000
   4      0.000000e+000 0.000000e+000 0.000000e+000 0.000000e+000
# ----------------------------------------------------------------
#  Class ID     Number of Cells    Class Name
      2            161        2
# Layers           1           2           3           4
# Means              2.218634e+001 1.396894e+001 0.000000e+000 2.550000e+002
# Covariance
   1      2.122901e+002 1.386058e+002 0.000000e+000 0.000000e+000
   2      1.386058e+002 9.056778e+001 0.000000e+000 0.000000e+000
   3      0.000000e+000 0.000000e+000 0.000000e+000 0.000000e+000
   4      0.000000e+000 0.000000e+000 0.000000e+000 0.000000e+000
# ----------------------------------------------------------------
#  Class ID     Number of Cells    Class Name
      3            25         3
# Layers           1           2           3           4
# Means              2.173600e+002 1.466800e+002 1.512000e+001 2.550000e+002
# Covariance
   1      1.838490e+003 1.397203e+003 5.928300e+002 0.000000e+000
   2      1.397203e+003 1.127310e+003 6.418733e+002 0.000000e+000
   3      5.928300e+002 6.418733e+002 7.510267e+002 0.000000e+000
   4      0.000000e+000 0.000000e+000 0.000000e+000 0.000000e+000
```

Appendix F (Sponges morphotypes catalog)

This catalog is based on the observation of videos and images of OFOBS dive PS101-169-1 of the sample area. The naming is temporary as there is no such catalog available. The catalog is biased on the geometry of the morphotypes which is shortened to geom-morphotypes

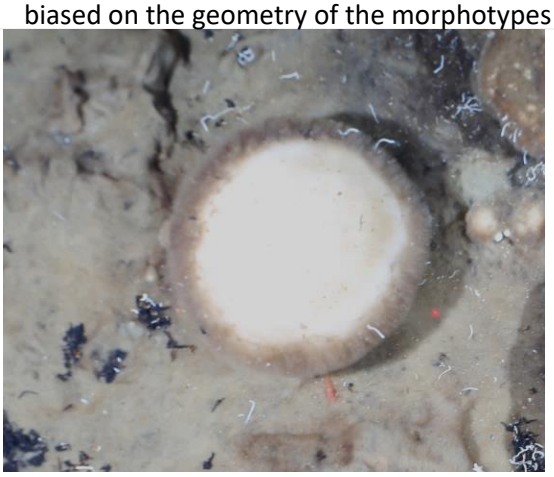

Convex crown

Concave crown

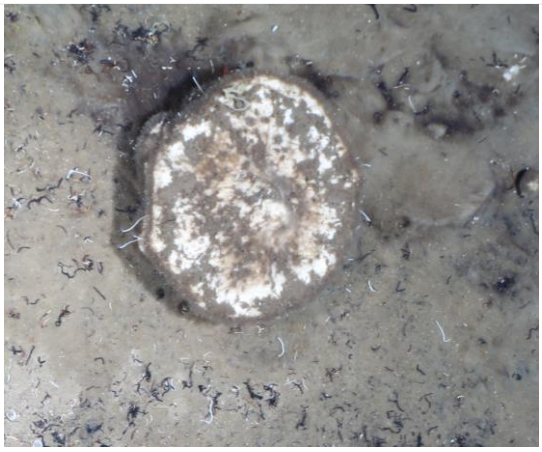

Flat crown

Half Flat/Convex crown

Concave crown with multi hole

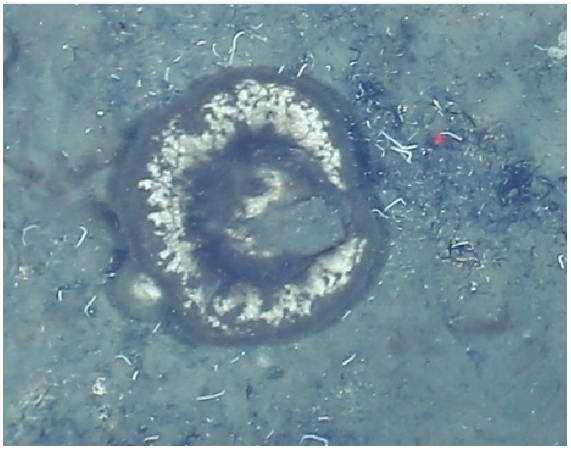

Ring shape

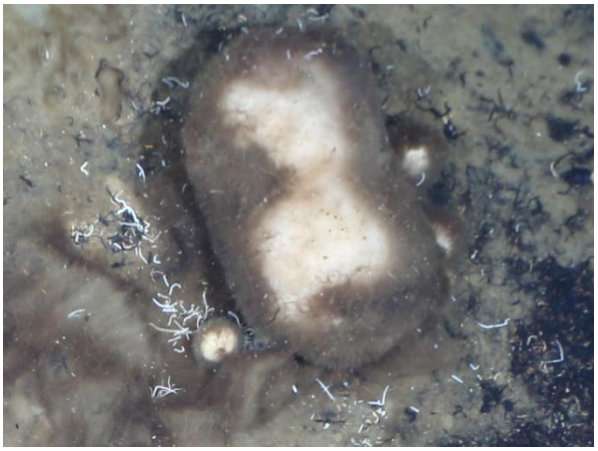

Tween Convex Crown

Tween Concave Crown

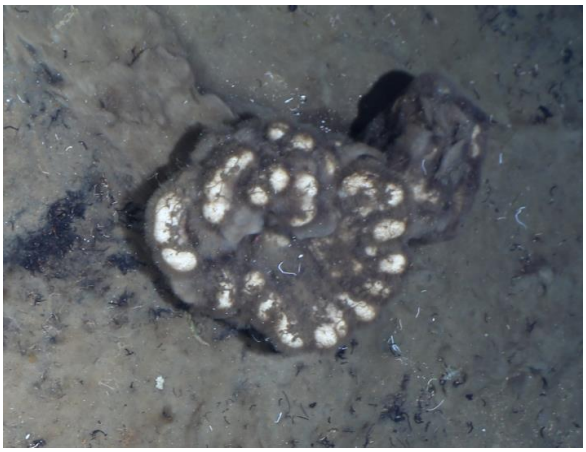

Convex nested crown

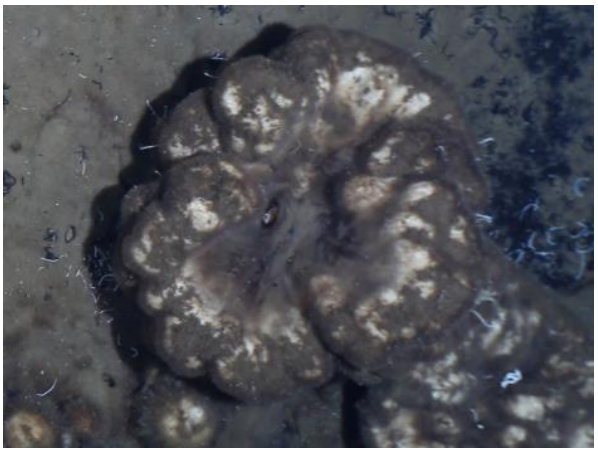

Concave nested crown

Multi deck crown

Appendix G (Complex situation for sponge detention)

Concave Crown (with a shrimp in the middle)

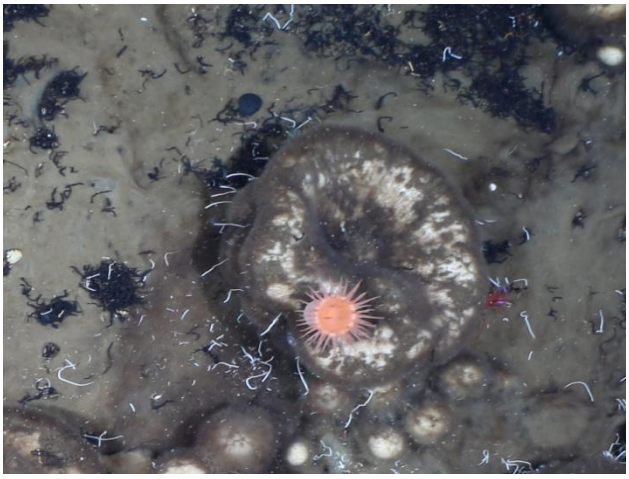

Single hole Concave Crown with anomaly in the top

Complex situation(sponges and Starfishes)

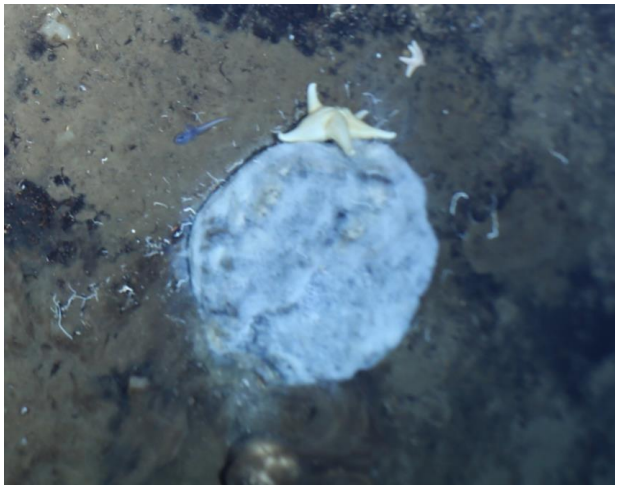

Complex Object (Bacterial mat covering dead/dying sponge and star fish)

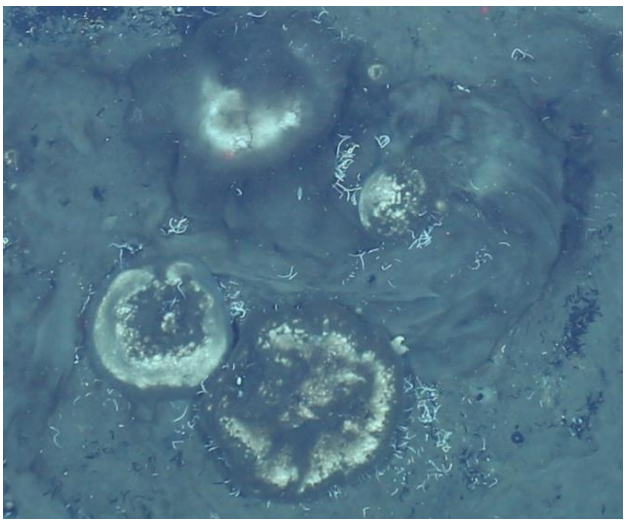

Sinked in and partly covered by sponge spicules

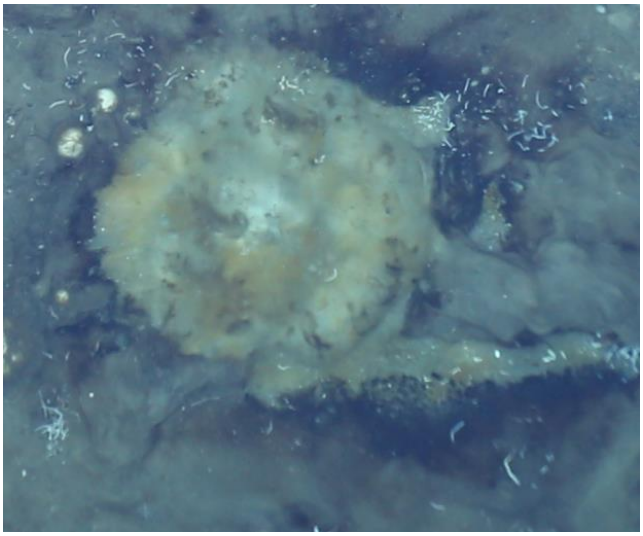

yellowish decaying dead/dying sponges mixed with bacterial mate

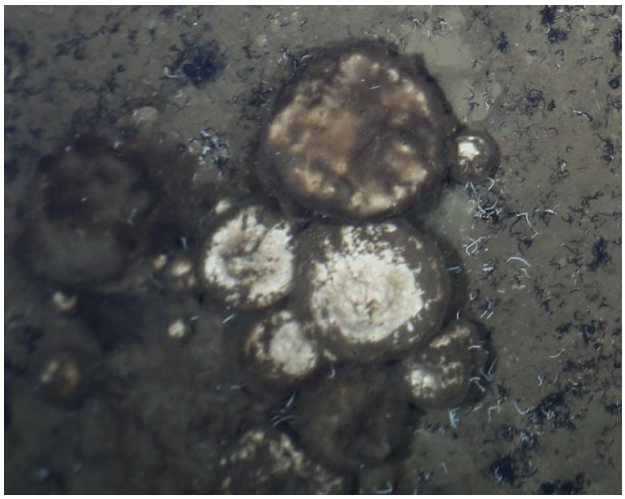

Mixed Group (collision scenario)

Complicated situation of sponges and sponge spicules